Title
Synergistic experimental and theoretical approach to atomic-level surface and interface science

Permalink
https://escholarship.org/uc/item/9n50j59z

Author
Grassman, Tyler J.

Publication Date
2007

Peer reviewed|Thesis/dissertation

UNIVERSITY OF CALIFORNIA, SAN DIEGO

SYNERGISTIC EXPERIMENTAL AND THEORETICAL APPROACH TO ATOMIC-LEVEL SURFACE AND INTERFACE SCIENCE

A dissertation submitted in partial satisfaction of the

requirements for the degree Doctor of Philosophy

in

Materials Science and Engineering

by

Tyler J. Grassman

Committee in charge:

      Professor Andrew Kummel, Chair
      Professor Edward Yu, Co-Chair
      Professor John Crowell
      Professor Charles Tu
      Professor John Weare

2007

The dissertation of Tyler J. Grassman is approved, and it is acceptable in quality and form for publication on microfilm:

_____

_____

_____

_____
Co-Chair

_____
Chair

University of California, San Diego

2007

TABLE OF CONTENTS

LIST OF SYMBOLS AND ABBREVIATIONS

Aluminum	Al
Angstrom	Å
Arsenic	As
Auger Electron Spectroscopy	AES
Capacitance Voltage	CV
Celsius	C
Complementary Metal Oxide Semiconductor	CMOS
Chlorine	Cl
Current	I
Degree	º
Density Functional Theory	DFT
Density of States	DOS
Electron	e^-
Electron Volt	eV
Enthalpy of Adsorption	ΔH
Et Alia	*et al.*
Gallium	Ga
Germanium	Ge
Hydrogen	H
Low Energy Electron Diffraction	LEED
Metal Oxide Field Effect Transistor	MOSFET
Monolayer	ML
Nanoampere	nA
Nitrogen	N
Oxygen	O
Perdew-Burke-Ernzerhof	PBE
Perdew-Wang 1991	PW91
Projected Density of States	PDOS
Projector Augmented Wave	PAW
Sample Voltage	V_s
Silicon	Si
Scanning Tunneling Microscopy	STM
Scanning Tunneling Spectroscopy	STS
Tunneling Current	I_t
Ultra High Vacuum	UHV
Vienna *ab initio* Simulation Package	VASP
Volt	V

LIST OF FIGURES

Chapter Five

Chapter Six

x

LIST OF TABLES

ACKNOWLEDGEMENTS

I would like to acknowledge, and thank, my advisor, Professor Andrew Kummel, for allowing me to join his lab, even though I am from Oregon (it appears we may have even started a trend with this). From good to bad, I've learned a lot, seen a lot, and I think accomplished a lot, in my time here. The experience and knowledge, of all flavors (especially the grant-writing arena), will be invaluable in my upcoming career. Thank you.

I would also like to thank my lab-mates, both past and present, many of whom have become close, valuable friends. These years would have been impossible (not to mention boring) without you. I consider myself very lucky for getting to work with you, and even more so for getting to actually know you. Our scintillating, and completely scientific, conversations over coffee and lunch have made all the difference. Keep it up, and I wish you all the best of luck.

I would like to specifically thank Darby for her support, extreme patience, and countless hours of mulling over ideas, problems, and anything else that may have arisen over the years during our learning and application of density functional theory in the course of our work.

I would like to thank my other friends and family. Though you may not necessarily have contributed directly to my grad school adventure, you were no less important to the experience.

Finally, I would like to thank Nancy, for everything. A simple "thank you" is truly not enough, but it is a start.

Chapter 3, in part or in full, is in preparation for submission for publication in the Journal of Chemical Physics. The dissertation author is the primary investigator and author of this paper:

T. J. Grassman, S. R. Bishop, A. C. Kummel, "An atomic view of Fermi level pinning of Ge(100) by O_2." *In preparation for submission to the Journal of Chemical Physics* (2007).

Chapter 4, in part or in full, is in preparation for submission for publication in the Journal of Chemical Physics. The dissertation author is the primary investigator and author of this paper:

T. J. Grassman, A. C. Kummel, "Passivation of the Ge(100) surface using molecular SiO." *In preparation for submission to the Journal of Chemical Physics* (2007).

Chapter 5, in full, is in preparation for submission for publication in various conference proceedings. The dissertation author is the primary investigator and author of this paper:

T. J. Grassman, S. R. Bishop, A. C. Kummel, "Density functional theory study of first-layer adsorption of ZrO_2 and HfO_2 on Ge(100)." *In preparation* (2007).

Chapter 6, in full, is a reprint of the material as it appears in the following publication, for which the dissertation author was the primary investigator and author:

T. J. Grassman, G. C. Poon, A. C. Kummel, "Low coverage spontaneous etching and hyperthermal desorption of aluminum chlorides from Cl_2/Al(111)," Journal of Chemical Physics **121**, 9018 (2004).

VITA

2000   Bachelor of Arts, Chemistry – University of Oregon

2000-2001   Teaching Assistant – University of California, San Diego

2001   Master of Science, Materials Science and Engineering – University of California, San Diego

2001-2007   Research Assistant, Kummel Lab – University of California, San Diego

2007   Doctor of Philosophy, Materials Science and Engineering – University of California, San Diego

PUBLICATIONS

T. J. Grassman, S. R. Bishop, A. C. Kummel, "Density functional theory study of first-layer adsorption of ZrO_2 and HfO_2 on Ge(100)." *In preparation* (2007).

T. J. Grassman, A. C. Kummel, "Passivation of the Ge(100) surface using molecular SiO." *In preparation for submission to the Journal of Chemical Physics* (2007).

T. J. Grassman, S. R. Bishop, A. C. Kummel, "An atomic view of Fermi level pinning of Ge(100) by O_2." *In preparation for submission to the Journal of Chemical Physics* (2007).

D.L. Winn, M.J. Hale, T.J. Grassman, J.Z. Sexton, A.C. Kummel, R. Droopad, and M. Passlack "Electronic properties of adsorbates on GaAs(001)-$c(2\times8)/(2\times4)$" *Submitted to J. Chem. Phys* (2007).

D. L. Winn, M. J. Hale, T. J. Grassman, A. C. Kummel, R. Droopad, M. Passlack, "Direct and indirect causes of Fermi level pinning at the SiO/GaAs interface," Journal of Chemical Physics **126**, 84703 (2007).

M. J. Hale, D. L. Winn, T. J. Grassman, A. C. Kummel, "Chemically resolved scanning tunneling microscopy imaging of Al on *p*-type $Al_{0.1}Ga_{0.9}As(001)$-$c(2\times8)/(2\times4)$," Journal of Chemical Physics **122**, 124702 (2005).

T. J. Grassman, G. C. Poon, A. C. Kummel, "Ultra-low coverage spontaneous etching and hyperthermal desorption of aluminum chlorides from Cl_2 on Al(111)," Journal of Chemical Physics **121**, 9018 (2004).

G. C. Poon, T. J. Grassman, J. C. Gumy, A. C. Kummel, "Direct and precursor-mediated hyperthermal abstractive chemisorption of Cl_2/Al(111)," Journal of Chemical Physics **119**, 18 (2003).

M. K. Knowles, T. J. Grassman, A. H. Marcus, "Measurement of the dynamic structure function of fluorescently labeled complex fluids by Fourier imaging correlation spectroscopy," Physical Review Letters 85, 2837 (2000).

T. J. Grassman, M. K. Knowles, A. H. Marcus, "Structure and dynamics of fluorescently labeled complex fluids by Fourier imaging correlation spectroscopy," Physical Review E **62**, 8245 (2000).

FIELDS OF STUDY

Major Field: Chemistry (Physical)

    Studies in Complex Fluids
    Professor Andrew H. Marcus

Major Field: Materials Science and Engineering (Surface Science)

    Studies in Gas-Surface Dynamics
    Professor Andrew C. Kummel

    Studies in Semiconductor Surface and Interface Science
    Professor Andrew C. Kummel

ABSTRACT OF THE DISSERTATION

SYNERGISTIC EXPERIMENTAL AND THEORETICAL

APPROACH TO ATOMIC-LEVEL SURFACE AND

INTERFACE SCIENCE

by

Tyler J. Grassman

Doctor of Philosophy in Materials Science and Engineering

University of California, San Diego, 2007

Professor Andrew Kummel, Chair

Professor Edward Yu, Co-Chair

Two different areas of surface science topics have been studied using a synergistic combination of experiment and theory, which provides for both explanation and clarification of experimental results, as well as prediction for future experiments. Low

coverage oxidation Ge(100) was studied using scanning tunneling microscopy (STM), scanning tunneling spectroscopy (STS), and DFT modeling of bonding and electronic structures. 100 L O_2 exposure was found to pin the Fermi level near the valence band due to a strong coverage effect, with theoretical findings consistent with experimental observations. The passivation of Ge(100) surface using molecular silicon monoxide (SiO) was studied using STM, STS, and DFT modeling of bonding and electronic structures. The adsorbed SiO was found to form trimer, $(SiO)_3$, trough-bridging pyramids that did not pin the Fermi level. Ordered molecular metal oxide (ZrO_2 and HfO_2) adsorbate interfaces on Ge(100) were studied using DFT modeling of bonding and electronic structures. Metal-down and oxygen-down structures were found to be energetically degenerate, with metal-down structures forming metallic interface and oxygen-down structures forming passive interfaces. Calculated density of states minima shifts were attributed to possible band bending extending beyond the depth of the computational Ge slabs. The gas-surface dynamics and etching by low-coverage Cl_2 on Al(111) was studied using time-of-flight mass spectrometry, King-and-Wells sticking measurements, and density functional theory (DFT) modeling. Hyperthermal desorption of $AlCl_3$ was documented and attributed to fast-time-scale surface diffusion and agglomeration of adsorbed Cl to form aluminum chlorides with activated chemisorption states having potential energies above the vacuum level.

CHAPTER ONE

Background and Introduction

1.1 PASSIVATION AND PINNING OF GE(100)

For nearly five decades, silicon and its native oxide, silicon dioxide, have spearheaded the digital electronics revolution as the materials of choice for use in the ubiquitous metal-oxide-semiconductor field effect transistor (MOSFET), invented by Kahng and Atalla at Bell Labs in 1960. A conceptual schematic of an example MOSFET device (enhancement-mode n-channel MOSFET) is given in Figure 1.1. This choice of semiconductor and insulator materials was a matter of pure practicality, owing to the serendipity of the extremely low defect density interface between the Si and the thermally grown SiO_2, in addition to other such characteristics as low cost of production, ease of integration, and high availability of silicon. Much of the growth of the digital electronics industry is a result of the high scalability of these Si-based MOSFETs (e.g. exponential increase in processing core speeds), wherein the shrinking of the device dimensions provides for a host of benefits, including higher drive currents and increased gate capacitance (i.e. faster switching times and lower energy usage), and higher device packing density.

By the 1990's it had become clear that the industry was approaching the fundamental limits of classical Si MOSFET device scaling. One of the pre-eminent

problems was electrical leakage through the ever-thinning gate dielectric. This problem was only recently alleviated by the introduction of high-κ gate dielectrics and metal gates, allowing for the use of increased oxide thicknesses, and thus electrical insulation, while maintaining a scalable gate capacitance (i.e. equivalent oxide thickness, EOT). This solution, however, provides only a temporary fix to the scaling issues faced by Si-based MOSFET devices. In order to further improve device, and therefore end product (e.g. CPUs), performance, a new semiconductor channel material is needed, with intrinsic characteristics beyond that of silicon.

One such alternative material is germanium, whose greater low-field intrinsic carrier mobilities may provide for a significant increase in drive current and reduction of gate bias over state-of-the-art silicon MOSFET devices (Table 1.1 compares these bulk materials properties for Ge and Si). However, in contrast to Si, Ge does not have a suitably stable electrically-passivating native oxide. The Ge native oxide, GeO_2, is both water-soluble and thermally unstable at elevated temperatures; GeO_2 decomposes and desorbs as GeO above 400ºC.[1-3] Therefore, an alternative dielectric and/or electrical passivation method is also needed.

With the introduction of new semiconductor and dielectric materials comes the introduction of new challenges to the field of semiconductor surface and interface science. With respect to the semiconductor/dielectric interface, successful MOSFET operation requires a very low defect density, low physical roughness, and an electronic passivity. An electronically passive interface is one that lacks a significant density of electronic states in the semiconductor band gap, a condition that can induce Fermi level pinning. Interface state-induced Fermi level pinning occurs when a significant density of

electronic states in the band gap or on the band edges forms, causing the valence and conduction bands (VB and CB, respectively) to bend in such a manner as to satisfy charge neutrality at the interface (not to be confused with gate metal-induced Fermi level pinning on high-κ gate stacks). Figure 1.2 presents a simple schematic of this phenomenon for both *p*- and *n*-type semiconductors. Given the fact that Si is basically the only major semiconductor material that produces low defect and state density interfaces with its native oxide, Fermi level pinning is likely to be a major issue for devices produced with both new channel and dielectric materials, and as such is one of the major focuses of the work presented in this dissertation.

Numerous experiments have attempted the fabrication of Ge-based MOSFET and MOSCAP (metal-oxide-semiconductor capacitor) devices using a great diversity of insulators, including GeO_2,[4-6] Ge_3N_4,[7] GeO_xN_y,[5,8,9] SiO_2 (with and without a Si interlayer/cap),[10-13] and high-k metal-oxides ($BaStTiO_3$, ZrO_2, HfO_2).[12,14,15] The success of these different dielectric materials has indeed been found to depend greatly on the nature of the semiconductor-oxide interface. Devices fabricated with poor passivation at the oxide/Ge(100) interface were consistently found to yield poor C-V (capacitance-voltage) characteristics; large frequency dispersion in accumulation, capacitance peaks within the band gap, gate leakage, and/or flatband shifts, all of which are associated with interfacial or oxide traps and fixed charge. Those devices that were fabricated with proper interfacial passivation (or, at the very least, sufficient initial cleaning of the Ge surface to remove all native oxide) were found to exhibit superior C-V characteristics. However, despite the wealth of results indicating the importance of interfacial effects, the exact mechanisms behind semiconductor passivation and pinning are still relatively

unclear. It is, therefore, the goal of the work presented in this dissertation to correlate interfacial bonding structures with the resulting interfacial electronic structures in order to better understand the atomic-level mechanisms of both electronic passivation and Fermi level pinning.

A. The Effects of Interfacial Ge Native Oxide

From the previously discussed C-V studies, one can conclude that the Ge-based MOSFET devices with the best properties are those that have been carefully produced such that the native oxide has either been modified or eliminated altogether. Even experiments attempting to grow high-quality GeO_2 yielded thin oxide films with large suboxide concentrations.[4] Other experiments, however, have shown that the native oxide can be modified via nitridation to produce devices with improved electrical properties compared to those with unmodified native oxide interfacial layers.[8,16] It follows that primary goal of interfacial passivation in Ge-based MOS structures is the modification or elimination of this native oxide. Nonetheless, it is still unclear as to *why* the native oxide causes such problems. It is unknown if the observed unfavorable device characteristics is due merely to the formation of Ge-O bonds or due to the properties of bulk GeO_2. Therefore, it is critical to determine if Ge-O bonding alone can pin the Fermi level to determine if other oxides can be directly deposited on Ge while retaining a passive interface.

While Ge-O bonding might pin the Fermi level, we note that the pinning may not be intrinsic to all Ge-O bonds on the Ge(100) surface. For example, while the GeO_2/Ge interface is pinned, a ZrO_2/Ge interface may be unpinned, even though both interfaces

contain Ge-O bonds. Furthermore, even for a given interface, the deposition method can change the electronic structure because the bonding geometries of adsorbates on surfaces play a definitive role in the determination of the electronic properties of the resultant interfaces. This is an especially important issue in the consideration of electrical passivation of semiconductor surfaces, where bond angles and coordination numbers can have a large effect on the electronic structure. Therefore, a thorough characterization and understanding of the effect of Ge-O bonding at the Ge(100) surface is paramount for understanding the interfaces made with potential gate dielectric oxides for Ge-based MOSFET devices.

Much work has been performed over the past decade using STM-based experiments to characterize the initial oxidation of the Ge(100)-2×1 surface, including the effect of post-oxidation annealing and elevated-temperature oxidation.[17-23] A few studies utilizing density functional theory modeling have also been produced,[24,25] but these have mostly concentrated on the initial metastable oxygen adsorption sites. While these various works have provided much insight into the physical nature of the Ge(100) oxidation reaction, a thorough and unambiguous identification of the various adsorbate and reaction product geometries and their electronic structure has remained elusive.

Chapter Three of this dissertation presents an atomic-level study of the structural and electronic properties of the O_2 oxidation reaction on the Ge(100) surface utilizing scanning tunneling microscopy (STM), scanning tunneling spectroscopy (STS), and density functional theory (DFT) modeling, in order to get at a fundamental understanding of the atomic geometries of the surface binding sites (STM, DFT) and the resultant electronic structure of those sites (STS, DFT). Long, low-temperature (325ºC) post-

oxidation anneals allowed for the elimination of various metastable and/or transitional reaction sites, as well as the coalescence of the oxygen adsorbate species, so that the effect of specific reaction products on the electronic structure could be elucidated, while anneals above 425ºC returned the Ge(100) surface to its "clean" state via the desorption of Ge oxides and a reordering of the surface Ge atoms. For definitive determination of the effect of O_2 dosing and annealing on the electronic structure, STS spectra were taken on the clean and O_2 dosed surfaces of both *n*-type and *p*-type substrates, and the observed reaction sites were modeled with DFT to help better characterize the physical and electronic structures. The major result from this work was that low-coverage oxidation of Ge(100) induces Fermi level pinning, which was attributed to two main causes: the addition of half-filled dangling bonds to the surface in the form of displaced Ge ad-atoms and ad-dimers (a by-product of the room-temperature oxygen dimer displacement reaction), and a strong suboxide coverage effect owing to high densities of oxygen dimer displacement sites on the room-temperature oxidized surface and the formation of extended suboxide row-like structures on the low-temperature annealed surface.

B. Silicon and Silicon Oxides for Oxide/Ge Interfacial Passivation

Given the results of the Ge(100) oxidation study, it is reasonable to conclude that the best solution to oxide/Ge passivation is the avoidance of the formation of the native oxide altogether. In order to accomplish this in such a manner as to still allow the growth and/or deposition of oxide dielectrics during device fabrication, oxygen needs to be blocked from reacting with, or even reaching, the Ge surface. The elimination of the dangling bonds on the surface dimer atoms would drastically reduce the reactivity of the

Ge(100) surface, just like hydrogen passivation on Si(100). A diffusion barrier with either low or highly-controllable reactivity would help to prevent oxygen from even reaching the Ge. Therefore, a thin film of some material with both of these properties would be an ideal passivating buffer layer for oxide dielectric growth on the Ge(100) surface.

Silicon is one such material that has been considered for this role. Si-O and Si-Ge bonding are both known to be passive. Epitaxially-grown Si (with and without subsequent oxidation or SiO_2 deposition) capping layers have been utilized to produce successful high-κ/Ge-based MOS devices.[11,12,26] Such devices are quite interesting due to the potential for dramatic increase in carrier mobilities available through strain engineering of the Ge channel. However, these devices result in buried channel, rather than surface channel, operation and therefore present particular engineering challenges, including issues dealing with scalability and short-channel degradation.

SiO is a non-pinning transitional species at the Si/SiO_2 interface;[27-29] this interface possesses the lowest defect density of any known oxide/semiconductor interface. Given the chemical and electronic similarities of Si and Ge, it is a reasonable assumption that SiO may also be able to exist as a non-pinning transitional species at the SiO_2/Ge interface (or potentially at any oxide/Ge interface). SiO can be sublimated congruently from solid source; therefore, SiO is very easy to deposit cleanly on the Ge surface. Basic chemical reasoning also indicates that SiO should bond to the Ge surface Si-end down; the O atom's octet is filled by the double bond formed with the Si atom, but the Si atom still possesses two reactive half-filled dangling bonds. Therefore, SiO should bond to the Ge surface without the formation of high densities of Ge-O bonds. Indeed, high-quality

solid SiO source MBE-grown epitaxial layers have been reported on the GaAs(100) surface,[30] but no such attempts appear to have been previously made on the Ge(100) surface. (Note: A very recent publication reports the use of a SiO_x passivating interlayer on Ge, with a HfSiO gate dielectric, with good device characteristics, but no information was given on the nature of or the growth/deposition method of the SiO_x material.[31])

Chapter Four of this dissertation presents an atomic-level study of the structural and electronic properties of SiO deposited on the Ge(100) surface utilizing scanning tunneling microscopy (STM), scanning tunneling spectroscopy (STS), and density functional theory (DFT) modeling to provide a fundamental understanding of the atomic structure of the surface binding sites (STM, DFT) and the resultant electronic structures (STS, DFT). For definitive determination of the effect of SiO deposition and on the electronic structure, STS spectra were taken on the clean and SiO-deposited surfaces of both *n*-type and *p*-type substrates, and the observed reaction sites were modeled with DFT to help better characterize the physical and electronic structures. The major result from this work was that low-coverage molecular SiO bonds to the Ge(100) surface, after post-deposition anneals of 200 – 300ºC, via $(SiO)_3$ trough-bridging "pyramid" units that do not induce Fermi level pinning, indicating that thin films of MBE-deposited SiO may indeed provide for successful passivation for oxide growth in Ge-based MOSFET fabrication.

C. The Effect of Interfacial Bonding Geometries for ZrO_2 and HfO_2 on Ge(100)

The most studied, and probably most successful, gate dielectric materials for Ge(100) are the transition metal dioxides ZrO_2 and HfO_2 (denoted as MO_2 hereafter),

usually grown by atomic layer deposition (ALD). These oxides, under normal Ge processing conditions, are amorphous, and depending on initial Ge surface passivation, the oxide/Ge interface may be either abrupt or contain some germanate interlayer (though these interlayers are thinner than those found with Si). High resolution TEM imaging indicates that ZrO_2 tends to form more abrupt interfaces, while HfO_2 has been shown to be more likely to form interfacial interlayers.[32] TEM imaging also seems to indicate that the abrupt ZrO_2/Ge interface may be ordered, even though the rest of the oxide layer is amorphous.

MOSFET (and MOSCap) device quality is found to vary greatly in these MO_2/Ge(100) gate stacks, with the trend closely related to the oxide-semiconductor interface quality and composition (i.e. clean vs. oxidized surface, native oxide vs. oxynitride, abrupt vs. interlayer interface, etc.).[33] Currently available data, however, is not accurate or precise enough to sufficiently characterize the post-processed oxide/Ge interface, so detailed conclusions about the exact causes of problems related to the interface in these devices are unable to be definitively made. It is hoped that carefully performed high resolution scanning transmission electron microscopy (STEM) imaging in the near future will enable a close look at the structure of the oxide/semiconductor interface, revealing the extent of order at these interfaces and the nature of the bonding structure, metal-O-Ge vs. O-metal-Ge, or a combination of the two. Synchrotron radiation photoelectron spectra from a layer-by-layer etched ZrO_2/Ge gate stack, with an abrupt interface, revealed that a submonolayer thickness Ge suboxide layer existed between the ZrO_2 and Ge, indicating the possibility of a Zr-O-Ge interfacial bonding configuration.[34]

Chapter Five of this dissertation presents the results from a survey of potential ordered oxide/semiconductor interface structures between stoichiometric molecular ZrO_2/HfO_2 and Ge(100), considering both surface coverage and surface binding configuration (O-metal-Ge bonding vs. metal-O-Ge bonding) using density functional theory (DFT) modeling. This work is by no means intended to be an exhaustive set of structures, but merely an attempt to provide some insight into the MO_2/Ge interfacial system. Additionally, these structures will serve as precursors to later computational studies of thick amorphous MO_2 layers on Ge(100). Calculated enthalpies of adsorption indicate that there is no thermodynamic preference for O-M-Ge vs. M-O-Ge, meaning that one should expect the actual interface to possess a mixture of the two bonding configurations. Calculated electronic structures indicate that full O-M-Ge bonding results in metallic interfaces due to the metallic character of the M-Ge bonds, which would be expected to cause Fermi level pinning, while M-O-Ge bonding appears to provide a passive interface due to the covalent character of the O-Ge bonds, which would be expected to provide an unpinned Fermi level.

1.2 THE ETCHING OF AL(111) BY CL_2

The final section of this dissertation, Chapter Six, deals with a topic that is only casually related to the Ge work, but is included because it was a major work by the author with very interesting results. This chapter addresses some of the gas-surface chemistry of the halogen-based plasma etching of aluminum interconnects during integrated circuit processing, an issue that is still not fully understood. Because plasma etching

environments are typically very complex, and therefore difficult to study as a whole, the problem is usually broken down into much simpler components, for example the dry etching of Al by Cl_2. The mechanism of Cl_2 adsorption onto aluminum, and subsequent etching by thermal aluminum chloride desorption, has been studied many times in the last few decades.[1-13] Etch rate and etch product studies utilizing a variety of techniques, including (but not limited to) quadrupole[1-3] and time-of-flight mass spectrometry,[5] gas-phase titration of chlorine atoms,[6] quartz-crystal microbalance,[2,4] *in situ* Fourier transform infrared spectroscopy,[7] Auger electron spectroscopy,[4,10-12] and x-ray photoelectron spectroscopy[1,4] have been performed at pressures ranging from UHV to near-atmospheric. Kinetic modeling has also been employed to characterize the processes involved in both the thermal and ion-assisted etching of Al(111) by Cl_2.[9]

Spontaneous high-rate thermal etching of Al by Cl_2 has been reported by several investigators at high surface coverages (monolayer or greater).[1-10] These reports state that at least monolayer coverages of chlorine are necessary for the initiation of thermal desorption of aluminum chloride etch products. Presumably this high chlorine coverage allows for subsurface absorption of Cl adsorbates to occur such that the surface Al atoms are surrounded by Cl atoms at stoichiometrically correct concentrations.[11] The stoichiometric aluminum chlorides are then said to thermally desorb into the gas phase, with a barrier to desorption equal to about room temperature. This thermal etching is reported to be quenched below room temperature;[6] while ion-assisted etching has been observed at -50ºC in electron cyclotron resonance (ECR) plasmas.[9] These proposed high-coverage adsorption and etching mechanisms reproduce the experimental high-coverage data reasonably well.

We observe not only that etching of Al(111) by Cl_2 can occur at very low surface coverages (< 5% monolayer), but that these etch products actually exit the surface at hyperthermal velocities corresponding to $2 - 30$ times thermal energy. Remarkably, these effects are independent of both surface temperature (experiments were performed at both 100 K and 500 K) and incident Cl_2 translational energy (0.11 eV, 0.27 eV, and 0.65 eV Cl_2 incident energies were studied). Time-of-flight mass spectrometry of aluminum chloride desorption products, Cl_2 sticking probability measurements, and etch rate profiling experiments (etch rate vs. Cl_2 exposure time) all clearly indicate a low-coverage hyperthermal etching behavior that has not previously been reported. Computational DFT modeling of the Cl_2/Al(111) gas-surface reaction sequence has also been performed to further characterize the mechanism behind this etching phenomenon. We have thus developed a mechanistic model to account for both the occurrence of the low-coverage etching and the hyperthermicity of the desorbed etch products. We hypothesize that the ultra low-coverage etch results from reactions of Cl adsorbates with exposed, and therefore more reactive, Al surface defect-type sites such as adatoms, regrowth islands, and step edges. It is at these special sites that the subsequently formed aluminum chloride reaction products are able to exist in a slightly energized or excited state, specifically an activated chemisorption state, with a potential energy above that of the vacuum level. Thereafter, desorption produces etch products that exit the surface with translational energies greater than that of thermal energy.
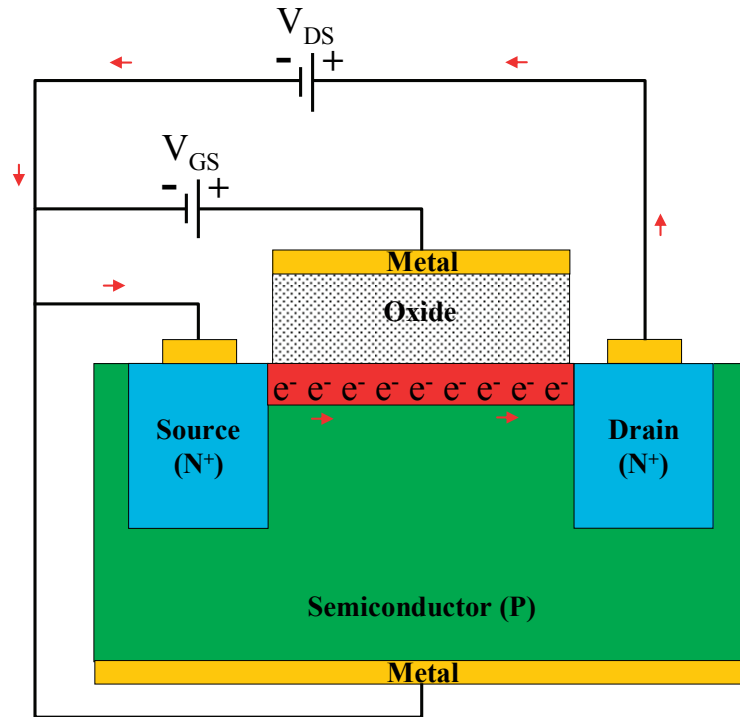
FIGURE 1.1. Conceptual diagram of an enhancement-mode n-channel MOSFET under working conditions. Application of a positive bias on the gate (with respect to the semiconductor bulk) produces a region of carrier inversion at the oxide/semiconductor interface (the channel). Bias applied between the source and drain causes carriers (in this case, electrons) to flow through the channel. Modulation of the gate bias then allows for switching on and off of the device (or adjusting the source-drain current gain).

TABLE 1.1. Bulk, room-temperature carrier mobilities and band gaps for Si and Ge.

Property	Si	Ge
$\mu_{n,\ 300\ K}$ (cm^2 V^{-1} sec^{-1})	1500	3900
$\mu_{p,\ 300\ K}$ (cm^2 V^{-1} sec^{-1})	450	1900
E_g (eV)	1.11	0.67
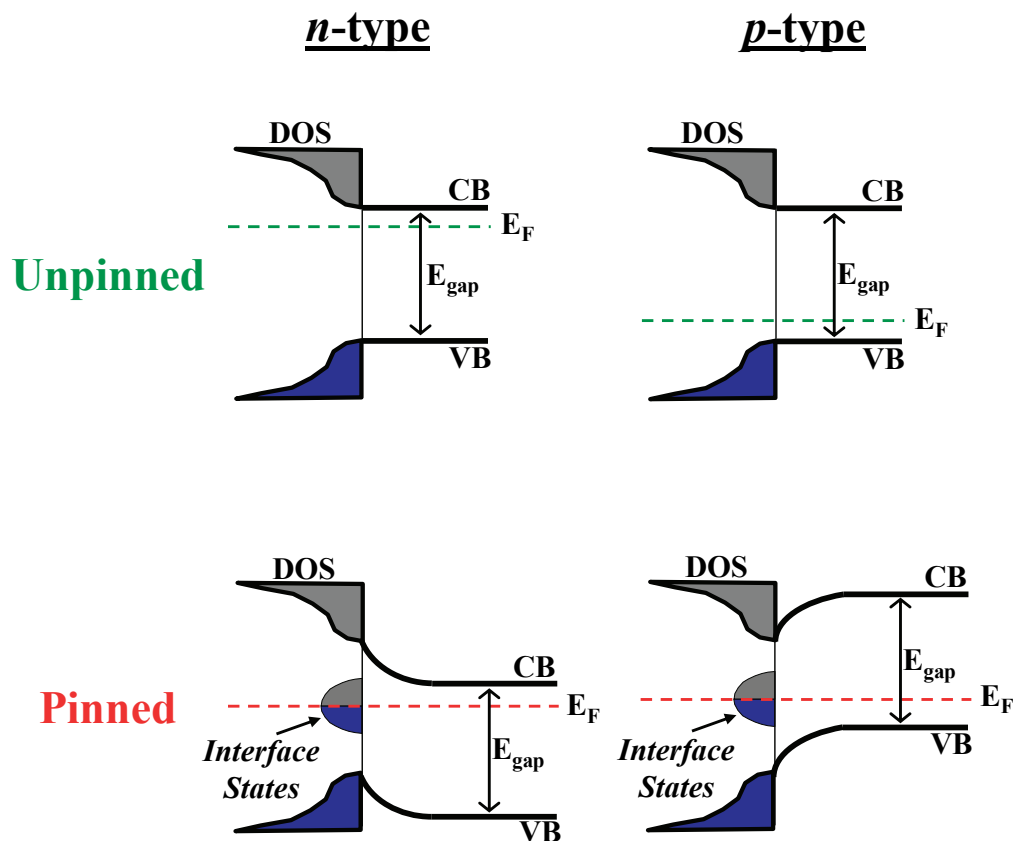
FIGURE 1.2. Conceptual schematic comparing interfaces with unpinned (top) and pinned (bottom) Fermi levels for both *n*- and *p*-type semiconductors. Unpinned interfaces are free of gap states, which allows for the VB and CB to be modulated by an applied gate bias in a MOSFET devices. A pinned interface results from a significant amount of induced gap (or band edge) states such that the bands at the interface must bend in order to satisfy charge neutrality. Because of this fixed band bending, the bands can no longer be adequately modulated by an applied gate bias, rendering the MOSFET effectively inoperable.

1.4 REFERENCES

[1]   R. H. Kingston, J. Appl. Phys. **27** (2), 101 (1956).

[2]   P. W. Loscutoff and S. F. Bent, Annu. Rev. Phys. Chem. **57** (1), 467 (2006).

[3]   K. Prabhakaran, F. Maeda, Y. Watanabe et al., Appl. Phys. Lett. **76** (16), 2244 (2000).

[4]   V. Craciun, I. W. Boyd, B. Hutton et al., Appl. Phys. Lett. **75** (9), 1261 (1999).

[5]   O. J. Gregory, E. E. Crisman, L. Pruitt et al., Mater. Res. Soc. Symp. Proc. **76**, 307 (1987).

[6]   Y. Wang, Y. Z. Hu, and E. A. Irene, J. Vac. Sci. Technol., A **12** (4), 1309 (1994).

[7]   D. B. Alford and L. G. Meiners, J. Electrochem. Soc. **134** (4), 979 (1987).

[8]   S. Huiling, H. Okorn-Schmidt, K. K. Chan et al., IEEE IEDM, 441 (2002).

[9]   C. M. Ransom, T. N. Jackson, and J. F. DeGelormo, IEEE Trans. Electron Devices **38** (12), 2695 (1991).

[10] R. S. Johnson, H. Niimi, and G. Lucovsky, J. Vac. Sci. Technol., A **18** (4), 1230 (2000).

[11] M. L. Lee, C. W. Leitz, Z. Cheng et al., Appl. Phys. Lett. **79** (20), 3344 (2001).

[12] K. C. Saraswat, C. O. Chui, T. Krishnamohan et al., Microelectron. Eng. **80**, 15 (2005).

[13] H. Shang, M. M. Frank, E. P. Gusev et al., IBM J. Res. & Dev. **50** (4/5), 377 (2006).

[14] R. A. McKee, F. J. Walker, and M. F. Chisholm, Science **293** (5529), 468 (2001).

[15] M. Meuris, A. Delabie, S. Van Elshocht et al., Mat. Sci. Semicond. Proc. **8** (1-3), 203 (2005).

[16] H. Kim, P. C. McIntyre, C. O. Chui et al., Appl. Phys. Lett. **85** (14), 2902 (2004).

[17] T. Fukuda, Surf. Sci. **417** (2-3), L1149 (1998).

[18] T. Fukuda and T. Ogino, Surf. Sci. **357-358**, 748 (1996).

[19] T. Fukuda and T. Ogino, Phys. Rev. B **56** (20), 13190 (1997).

[20]   T. Fukuda and T. Ogino, Surf. Sci. **380** (1), L469 (1997).

[21]   T. Fukuda and T. Ogino, Appl. Surf. Sci. **130-132**, 165 (1998).

[22]   T. Fukuda and T. Ogino, Appl. Phys. A **66** (0), S969 (1998).

[23]   S. Kurokawa, H. Yamashita, J. Yoshikawa et al., Jpn. J. Appl. Phys. **38** (Part 1, No. 6B), 3845 (1999).

[24]   E. J. J. Kirchner and E. J. Baerends, Surf. Sci. **311** (1-2), 126 (1994).

[25]   J. M. Soon, C. W. Lim, K. P. Loh et al., Phys. Rev. B **72** (11), 115343 (2005).

[26]   W. P. Bai, N. Lu, and D.-L. Kwong, IEEE Elec. Dev. Lett. **26** (6), 378 (2005).

[27]   K. T. Queeney, M. K. Weldon, J. P. Chang et al., J. Appl. Phys. **87** (3), 1322 (2000).

[28]   D. A. Muller, T. Sorsch, S. Moccio et al., Nature **399** (6738), 758 (1999).

[29]   M. C. Cheynet and T. Epicier, Philos. Mag. **84** (17), 1753 (2004).

[30]   N. Chand, J. E. Johnson, J. W. Osenbach et al., J. Cryst. Growth **148** (4), 336 (1995).

[31]   S. Joshi, C. Krug, D. Heh et al., IEEE Elec. Dev. Lett. **28** (4), 308 (2007).

[32]   Y. Kamata, Y. Kamimuta, T. Ino et al., Jpn. J. Appl. Phys. **44** (4B), 2323 (2005).

[33]   C. Chi On, H. Kim, D. Chi et al., IEEE Trans. Electr. Dev. **53** (7), 1509 (2006).

[34]   C. O. Chui, D.-I. Lee, A. A. Singh et al., J. Appl. Phys. **97**, 113518 (2005).

CHAPTER TWO

Experimental and Theoretical Methods

2.1 SEMICONDUCTOR SURFACE AND INTERFACE ANALYSIS

A. General Experimental Apparatus

All experiments were performed under ultra-high vacuum (UHV) conditions with a base chamber pressure of $2 - 3 \times 10^{-10}$ Torr. The UHV chamber is equipped with a water-cooled manipulator and sample holder, a VG Microtech EX05 differentially-pumped ion sputter gun, a custom-built differentially-pumped deposition source chamber (allowing for the low-background pressure deposition of various oxides from high-temperature effusion cells), a Park Scientific Autoprobe VP1 room-temperature scanning tunneling microscope (STM), and a standard set of analytical instruments: a PHI Model 10-155 Auger electron spectrometer (AES), a PRI low-energy electron defractometer (LEED), and a Hiden Analytical quadrupole mass spectrometer (QMS). Further experimental details pertaining to the individual experiments are detailed within their own specific chapter.

B. Ge Sample Preparation

Experiments were performed on 6 mm $\times$ 18 mm samples cut from n-type (Sb-doped, $1.88 \times 10^{17} - 1.54 \times 10^{18}$ cm^{-3}, $0.020 - 0.005$ Ω-cm) and p-type (Ga-doped,

$1.58 \times 10^{17} - 1.12 \times 10^{18}$ cm^{-3}, 0.040 – 0.010 Ω-cm) 100 mm Ge(100) wafers purchased from Wafer World (epi-grade, ±1° orientation tolerance). The samples were lightly cleaned of oils and particles using a lint-free cloth wetted with electronics grade (or better) methanol or isopropanol prior to insertion into the vacuum chamber.

The initial cleaning of the Ge surface is a challenge. The standard Si wafer wet etch methods result in the Ge(100) surface containing both native oxides and carbides (which do not dissolve into the bulk as is the case for Si), according to both literature[1,2] and the author's own experimental observations. In addition, with Si, it is often possible to prepare a clean,-well-ordered surface purely with high-temperature annealing. Such annealing was indeed found to remove the native oxides, but left behind rough surfaces with numerous large protrusions attributed to the formation of surface germanium carbides due to the insolubility of C in Ge. Therefore, it was necessary to develop a different method of sample preparation.

After an intensive literature review and much trial and error, a successful recipe was formulated. The Ge(100) samples were sputtered at normal incidence with 800 – 1000 V Ar$^+$ ions at a sample temperature of 500ºC, followed by resistive annealing at 700ºC for 20 minutes, with a 1ºC/min ramp down to room temperature. Typically, about three or four such cycles were required to reach acceptable surface cleanliness and order. This treatment produced large, well-ordered, defect-free terraces. Surface cleanliness and order was checked with AES, LEED, and STM.

C. Scanning Tunneling Microscopy and Spectroscopy

Scanning tunneling microscopy (STM) provides greater detail and resolution than

any other surface analysis technique (on conductive materials, at least), and was used in this work to identify surface bonding configurations of reaction products and adsorbates on the Ge(100) surface. The STM experiments were performed as follows: an atomically sharp metallic tip (electrochemically etched W, in this work) is positioned a few Angstroms above the surface of interest, and a bias is placed between the surface and tip (on the order of hundreds to thousands of millivolts) such that electrons will tunnel through the vacuum space to the substrate. The tip, which is attached to a piezoelectric actuation device (e.g. tube, tripod, etc.), is rastered across the surface, and a feedback loop is used to keep the tunneling current at a constant set value (on the order of hundredths of nanoamps to nanoamps); this is known as "constant-current" mode ("constant-height" mode, where the tip is kept at a fixed distance from the surface at all times is also possible, though used much less frequently). Because the tunneling current depends exponentially upon the tip-sample separation, it is very sensitive to changes in the surface structure. The result is an image of the surface topology (though it is somewhat convoluted with the electronic structure, as well).

When the surface is biased negative with respect to the tip, electrons tunnel *out* of the surface to the tip; this is known as "filled-state" imaging because the electrons are tunneling out of filled orbitals/bands. When the surface is biased positive with respect to the tip, electrons tunnel *into* the surface from the tip; this is known as "empty-state" imaging because the electrons are tunneling into empty orbitals/bands.

In the STM work presented in this dissertation, all images were taken using filled-state constant-current mode. STM images were generally taken at -1.5 V – -2.0 V sample

bias and 0.2 – 0.5 nA tunneling current using tungsten tips electrochemically etched in 2 M NaOH solution.

Scanning tunneling spectroscopy (STS) is a form of surface electronic structure measurement that can be carried out using the STM. Simple I-V spectroscopy can be performed by holding the tip in place above the surface, without rastering, and scanning the sample bias from negative to positive while tracking the resulting current. By placing a sine-wave modulation on the sample bias, and picking out the first harmonic of the resultant tunneling current signal with a lock-in amplified, one can measure dI/dV, which is understood to be roughly proportional to the local surface density of states.[3-9] Additionally, using a method developed by Feenstra *et al.*,[9] the tip-sample separate can be varied during the sample bias sweep, bringing the tip in and out from the surface. This technique is useful when performing STS on semiconducting samples in order to provide for increased dynamic range and sensitivity near the band gap.

STS experiments presented in this dissertation were performed with a 1.4 kHz, 0.2 V sine-wave sample bias modulation, and a Stanford Research Systems SR850 lock-in amplified was used to process the resulting tunneling signal. The spectra were subsequently normalized to unity for comparison.

2.2 DENSITY FUNCTIONAL THEORY

A. General Theoretical Framework

Density functional theory (DFT) is an *ab-initio* quantum mechanical method using the electron density (rather than the wave function) as the central variable to solve

the Schrödinger equation. DFT has been widely used in solid state physics theory work for three decades, and more recently within chemistry and materials science, with great success. Like with any quantum theory, DFT allows for the calculation of such properties as the molecular bonding structures and energies, surface reconstructions, chemical reactions, and the electronic structures of atoms, molecules, and solids (atomic and molecular orbitals, densities of states, band structures).

In standard wave function based quantum mechanics, the energy of a system with N electrons and M nuclei can be solved for, using the wave function Ψ, by calculating the expectation value of the Hamiltonian operator, $\hat{H}$,

$$E = \langle \Psi | \hat{H} | \Psi \rangle \tag{2.1}$$

$$\hat{H} = -\frac{1}{2} \sum_{i=1}^{N} \nabla_i^2 - \sum_{i=1}^{N} \sum_{A=1}^{M} \frac{Z_A}{r_{iA}} + \sum_{i=1}^{N} \sum_{j>i}^{N} \frac{1}{r_{ij}} = \hat{T} + V_{Ne} + V_{ee}. \tag{2.2}$$

The Hamiltonian is made up of three major parts (given in order of appearance in Equation 2.2): the electron kinetic energy, the electron-nuclei interaction (attraction), and the electron-electron interaction (repulsion). Note, the Hamiltonian given here has been simplified by the Born-Oppenheimer approximation, wherein the nuclear motion is considered fixed because of the large difference between electron and nuclear mass (and thus velocity), causing the nuclear kinetic energy term to drop out and the nuclei-nuclei interaction term becomes a constant.

However, according to the first Hohenberg and Kohn theorem,[10] the electron density, $\rho(\vec{r})$, can be used instead of the wave function, as it contains all of the same

information, but simplifies the calculations by reducing the number of variables involved. A total energy functional is then used to extract the same information as the Hamiltonian operator,

$$\rho(\vec{r}) = N \int \cdots \int |\Psi(\vec{x}_1, \vec{x}_2, \cdots \vec{x}_N)|^2 ds_1 d\vec{x}_2 \cdots d\vec{x}_N \qquad (2.3)$$

$$E[\rho] = T[\rho] + E_{Ne}[\rho] + E_{ee}[\rho] = \langle \Psi | \hat{H} | \Psi \rangle. \qquad (2.4)$$

The second theorem proves that the ground state energy can then be solved for variationally with respect to the system electron density, such that

$$E_0 = \min_{\rho \to N} \left(F[\rho] + \int \rho(\vec{r}) V_{Ne} d\vec{r} \right), \qquad (2.5)$$

where V_{Ne} is the potential due to the nuclei-electron interaction, and

$$F[\rho(\vec{r})] = T[\rho(\vec{r})] + J[\rho(\vec{r})] + E_{ncl}[\rho(\vec{r})], \qquad (2.6)$$

where $T[\rho]$ is the total electron kinetic energy, $J[\rho]$ is the classical Coulomb electron-electron interaction, and $E_{ncl}[\rho]$ is the non-classical electronic interaction. In simple terms, the equations state that the ground state energy is reached when the electron density approaches the true ground state electron density. Unfortunately, it does not provide a practical method with which to tackle the problem.

In 1965, Kohn and Sham[11] suggested that, in order to make these calculations a bit more practical, one could separate the terms that can be calculated exactly and those terms that cannot (because the exact functional form is not known, and must therefore be approximated). The true complex interacting system (i.e. having electrons that interact with each other) could then be mapped onto a less complex non-interacting system (i.e. the electrons only interact with an overall potential, not with each other), which can be explicitly described using a Slater determinant of one-electron spin orbitals, $\varphi_i(\vec{r}, s)$, such that the density resulting from the non-interacting system, ρ_S, exactly equals the ground state density of the true system of interacting electrons, ρ_0,

$$\rho_S(\vec{r}) = \sum_i^N \sum_s \left| \varphi_i(\vec{r}, s) \right|^2 = \rho_0(\vec{r}). \tag{2.7}$$

The separation of known and unknown terms produces the final expression for total energy,

$$E[\rho(\vec{r})] = T_S[\rho] + J[\rho] + E_{XC}[\rho] + E_{Ne}[\rho], \tag{2.8}$$

where $T_S[\rho]$ is the exact kinetic energy of the non-interacting reference system and $E_{XC}[\rho]$ is the exchange-correlation energy, which contains both the residual part of the true kinetic energy not covered by T_S and the non-classical electron-electron interaction, E_{ncl} (the exchange and correlation energies).

The Kohn-Sham formalism allows for the exact treatment of the majority of the contributions to the total energy, with everything else being covered by the exchange-correlation term. If the explicit functional form of E_{XC} was known, the Schrödinger equation could be solved for exactly. Unfortunately, this is not the case, and E_{XC} must therefore be approximated; the quality of density functional theory methods thus depends entirely upon the accuracy of the approximate exchange-correlation functional.

There are two main types of exchange-correlation (XC) functionals: LDA and GGA. The local density approximation (LDA), the first XC-functional to be introduced, defines the exchange-correlation energy per particle as that of a uniform electron gas. This approximation has proved to be remarkably accurate for use in bulk solids, especially metals, where the electron density varies slowly, but it is considerably less accurate in molecules and surfaces where the electron density varies rapidly. The generalized gradient approximation (GGA), however, provides improved accuracy in these systems by expressing the exchange-correlation energy in terms of local density gradients, which tend to better account for the rapidly varying electron densities found around atoms, molecules, and at surfaces.

B. Practical Computational Methodology

All of the computational DFT work presented in this dissertation was performed using the Vienna *Ab-initio* Simulation Package (VASP),[12-15] a well-known code designed for use in extended systems (e.g. solids, surfaces). VASP employs periodic boundary conditions and a plane-wave basis ($\exp[i\vec{k}\vec{r}]$) to describe systems extending infinitely in all three Cartesian coordinates. Surfaces can be studied by using a slab geometry

supercell in which there exists both the solid material, which will be continuous in two dimensions, and a vacuum space providing for discontinuity (and thus surfaces) in the third dimension.

An issue of great importance to computational work is that of convergence testing of such parameters as basis set size, k-point mesh density, surface slab and vacuum space thickness, and exchange-correlation functional. In the work presented in this dissertation, every attempt was made to ensure convergence and accuracy in all matters where possible. Plane wave basis set kinetic energy cut-off and k-point mesh densities were converged to within 1 meV/atom, whenever possible. Slab and vacuum thicknesses were similarly converged, with special attention paid to electronic interaction between slabs through the vacuum layer. Exchange-correlation functionals were tested for reproduction of properties of bulk materials, and literature was consulted for additional measures of accuracy.

The first four years of computational work were performed on 32-bit single-processor Linux PCs with 2 GB of RAM. The system sizes considered were usually quite large for these computers, and often the preferred parameter space was too large. In cases where absolute convergence (i.e. < 1 meV/atom) was not completely achievable, parameters were chosen as rigorously as possible. In all cases, however, the parameters used (cut-off energy, k-point mesh, slab and vacuum thickness) were on par with the vast majority of published work performed on similar systems, with special attention paid to the work of well-respected theoretical groups. The cut-off energies used in this work were always greater than the highest default energy chosen by VASP for any of the atoms ever to be considered in the work, which, according to the software documentation,

assured errors no larger than a few meV. Over the past year, however, large parallel Beowulf clusters were purchased, allowing for the performance of much larger calculations, and where the author felt necessary, calculation sets were repeated with an increased parameter space to assure the highest accuracy possible. The final values used are those reported in the individual chapters.

Estimation of the errors associated with these calculations, with respect to calculated ionization energies and enthalpies of adsorption, is not straightforward. When ionization energies and enthalpies of absorption have been experimentally measured, computational errors can be directly calculated; however, often this data does not exist (as is the case for most of the work presented in this dissertation). However, in an effort to attempt to quantify the errors expected in the computational work, two types of errors are estimated: convergence errors and method errors.

Convergence errors include both errors related to the choice of convergence parameters (plan-wave cutoff, k-point mesh density, slab and vacuum thickness, etc.), as well as relaxation parameters (maximum allowed interatomic forces). If the appropriate computational parameters are chosen, the convergence errors should be negligible compared to the method errors. The method errors encompass the errors inherent to the chosen computational method (exchange correlation functional, various approximations, atomic potentials, etc.) and can be further broken down into two subcategories: absolute method errors and relative method errors, or uncertainties.

Absolute method error refers to how well the computational results match with experimental data. For example, Paier *et al.* calculated the mean absolute error (absolute method error) with respect to experimental values for the G2-1 test set as 0.37 eV using

VASP, with PAW potentials and the PBE exchange correlation functional[16] (the same as was used in the Ge work presented in this dissertation). Although the absolute method error was calculated for a large set of widely varying molecular systems, 55 in total, the test set does not include any adsorbates on surfaces, which would be closer to the systems in the current study. Additional literature searches revealed no systematic studies of absolute method errors for adsorbates on surfaces. Although the absolute method error in this work is then potentially as large as 0.37 eV, the relative method errors are expected to be much smaller.

The relative method error refers to the uncertainty in the total energy difference between two similar adsorption sites or geometries. When comparing the relative total energies of a single adsorbate at two different sites on a surface, the relative error will be the most important error. For example, if the relative method uncertainty is ±0.10 eV and two structures, both having one adsorbate bonded in different locations, have adsorption energies of 1.00 and 1.05 eV, then the two structures must be considered degenerate due to computational uncertainties. A search of the literature revealed no systematic study of the relative method error for adsorbates on surfaces. However, we note that experts in the field report differences in binding energy at similar absorption sites on the same surface of ±0.10 eV to be significant using computational techniques similar to the ones in presented in this dissertation. Therefore, we have assumed a relative method error of ±0.10 eV for this work. Since the differences in calculated absorption energy are usually much larger than ±0.10 eV, the overall qualitative trends in both the calculations and the experiments should be in good agreement.

C. Issues with Density Functional Theory

While density functional theory is a powerful and useful a technique, it is not without its downfalls. Unfortunately, the work presented here on the Ge(100) system highlights one of the most egregious problems with standard approximate exchange-correlation DFT, the infamous band gap problem. DFT, using either the local density or the generalized gradient approximations, suffers from an underestimation of the semiconducting (or insulating) band gap of at least more than 30% (and often 40 – 50%). The problem is exacerbated when considering the small-gap semiconductors (e.g. Ge, InAs, GaSb, InSb), where the band gaps are predicted to be non-existent, with overlapping valence and conduction bands, producing a semi-metallic electronic structure.

The source of this problem lies in the Kohn-Sham formalism and approximation of the exchange-correlation potential, $V_{XC} = \partial E_{XC}/\partial \rho$. The difference between the true band gap, E_g, and the gap obtained for the exact Kohn-Sham non-interacting system, ε_g, is given by

$$E_g - \varepsilon_g \equiv \Delta = V_{XC}^{(+)} - V_{XC}^{(0)}, \qquad (2.9)$$

where $V_{XC}^{(+)}$ is the exchange-correlation potential due an increased electron density and $V_{XC}^{(0)}$ is the exchange-correlation potential belonging to the ground-state. The exact (true) exchange-correlation potential possesses a discontinuity upon the addition (or subtraction) of electron density to (from) the system, mostly existing in the self-

interaction term of the exchange potential (but there is also a discontinuity in the residual kinetic energy term, as well). However, due to the approximation of the exchange-correlation potential, this discontinuity gets smoothed over, giving $\Delta = 0$, thereby providing a reduced band gap, E_g.

Obviously, the band gap issue has no effect on the Al work presented in this dissertation. However, because Ge, which should posses a band gap of 0.67 eV, is predicted by DFT to lack a gap altogether, analysis of the electronic structure is problematic. Fortunately, because the overlap between the valence and conduction bands is small ($\sim$ 0.1 eV), the calculated molecular adsorbate structures and enthalpies of adsorption should not be strongly effected (i.e. bonding and non- or anti-bonding orbitals should still be significantly separated). The issue of electronic structure analysis is discussed in the individual chapters.

There are a few ways with which to remedy this situation, including self-interaction correction, Hartree-Fock exact exchange, and the GW approximation, but all of them increase computational expense by at least two orders of magnitude. Over the past five years, though, much progress has been made in the computational software community with regard to the inclusion of such higher-order methods, with expense approaching practicality.. Unfortunately, these upgrades for the VASP code have not yet been released, and as such these calculations have not yet been reworked (but we plan to recalculate our models with these advanced methods when they become available in VASP).

The two methods under consideration for the band gap correction reworking of these calculations are the use of hybrid functions and the GW approximation. Hybrid

functions are essentially regular LDA or GGA functionals that also include some amount of Hartree-Fock (HF) exchange. The exchange term is known exactly in the HF formalism, and has been shown to correct the problem due to the approximation of the XC potential in Kohn-Sham DFT. However, when used alone, the HF exchange term greatly overestimates the band gap so it is only added in small quantities to the hybrid function; for example, PBE0 utilized 25% HF exchange (as calculated via fourth-order perturbation theory) mixed with the regular PBE exchange-correlation function, and has been shown to not only help correct the band gap issue, but also improves overall chemical accuracy. However, there is concern that usage of hybrid functionals is not entirely theoretically rigorous; they are found to often actually overestimate the band gap and cause about a 10% flattening of the upper valence bands. In most cases, though, the pros greatly outweigh the cons.

The GW approximation is considered to be the most theoretically rigorous method available for the correction of the DFT electronic structure. This method expands the self-energy in terms of the single particle Green function (G) and the screened interaction (W), and provides for a correct description of the exchange-correlation discontinuity. The GW approximation is widely accepted as to be the method that provides the most accurate band structures. If the computational expense is acceptable, the GW approximation will be the preferred method of post-DFT electronic structure correction.

2.3 GAS-SURFACE DYNAMICS

A. General Experimental Apparatus

All experiments were performed under ultra-high vacuum (UHV) conditions, with a base chamber pressure of 2×10^{-10} Torr. A schematic diagram of the full vacuum chamber system used for these experiments, including laser and molecular beam paths, is presented in Figure 2.1. A detailed schematic of the molecular beam path is presented in Figure 2.2. The main chamber contains a standard suite of UHV analytical instruments, including a home-built ion gun, a UTI 100C quadrupole mass spectrometer (QMS), a PHI Model 10-155 Auger electron spectrometer (AES), and a PRI low-energy electron defractometer (LEED).

Experiments were performed on an aluminum single crystal (Monocrystals Company, 99.999+% purity, 10 mm diameter × 2 mm thickness) with a (111) surface orientation. The aluminum surface was cleaned by sputtering with normal incidence 2 kV Ar^+ ions, followed by a two minute anneal (500ºC) to reduce sputter damage and reorder the surface. Surface purity and order were checked by AES and LEED.

A mechanically chopped (7 µs chopper open time), 10 Hz pulsed supersonic molecular beam (General Valve, model #9-400-900, 2 mm orifice) of Cl_2 seeded in different noble gases was used to dose the aluminum surface at three different Cl_2 incident energies: pure Cl_2 at 0.11 ± 0.01 eV, 5% Cl_2/Ne at 0.27 ± 0.01 eV, and 5.32% Cl_2/He at 0.65 ± 0.02 eV. All related etching experiments were performed with the molecular beam at normal incidence to the surface, and products were detected just off-

normal (~9º from the surface perpendicular) in an effort to avoid interference from the incident beam.

All gases were purchased premixed from Matheson Tri-Gas, and no other halogen contaminants were detected by QMS. The average beam fluxes – as calculated via half surface coverage times from sticking data, and using a simple 1-θ sticking coefficient dependence – were found to be as follows: 3.0×10^{13} molecules cm^{-2} sec^{-1} for pure Cl_2, 2.6×10^{13} molecules cm^{-2} sec^{-1} for Cl_2/Ne, and 1.0×10^{13} molecules cm^{-2} sec^{-1} for Cl_2/He. All three molecular beam varieties gave an increase in background pressure of no more than 2×10^{-11} Torr when introduced into the main UHV chamber.

B. Time-of-Flight Mass Spectrometry

Time-of-flight mass spectrometry (TOF-MS) uses the difference in transit time through a drift region to separate ions of different masses, yielding a near-simultaneous recording of all species (without energy scanning). Figure 2.3 is a schematic diagram of a standard TOF-MS instrument. An electric field accelerates a pulse of ions into a field-free drift region with a kinetic energy of $E = qV = 0.5mv^2$, where q is the ion charge, V is the applied acceleration voltage, m is the ion mass, and v is the ion velocity. Because ions of different masses will possess different drift velocities, lighter ions will arrive at the detector earlier than the heavier ions, thereby separating the ions by mass (multiply-charged ions will appear to be much lighter than their singly-charge counterparts, but such species tend to occur in very low concentrations). Because TOF-MS operates in a pulsed mode, it couples very well to pulsed laser ionization methods, with shorter pulse widths providing enhanced resolution.

With knowledge of the various distances of travel for the incident Cl_2 beams and the desorbing $AlCl_3$ molecules, a well-defined triggering event (in this work, the chopper wheel open time), and a controllable ionization laser fire delay, one can produce a spectra of ion intensity vs. desorbed molecule flight time (from the surface to the ionization point). From this data, the velocity and translational energy of the desorbing molecules can be calculated. By fixing the laser fire delay to some particular time, which corresponds to a specific velocity of desorbing molecules, one can also measure the etch rate of $AlCl_3$ molecules desorbing from the surface at that exact velocity.

In the Cl_2/Al(111) work presented in this dissertation, the aluminum chloride desorption products were ionized via nonresonant multiphoton ionization (MPI) and detected via subsequent time-of-flight mass spectrometry (TOF-MS). A standard Thermionics time-of-flight mass spectrometer with a 10 cm flight tube was used. The pulsed UV laser was optimized for resonant multiphoton ionization (REMPI) of neutral chlorine atoms, but also provided sufficient fluence for both the dissociation of the aluminum chloride desorption products and a strong nonresonant aluminum MPI signal, as described by Equations 2.1 and 2.2.

$$Al_xCl_y \xrightarrow{\text{n}h\nu} xAl + yCl \qquad\qquad (2.10)$$

$$Al \xrightarrow{\text{n}h\nu} Al^+ \qquad\qquad (2.11)$$

The laser light was prepared by using the frequency-doubled fundamental from a Q-switched Nd:YAG laser (Continuum, 581C-SF; 532 nm, 10 Hz, 7 ns pulse width) to

pump a tunable dye laser (Lambda-Physik, FL 3002) running DCM/methanol, tuned to 630.3 nm. The dye laser output was frequency-doubled with a KDP-C crystal housed in a wavelength-tracking package (Inrad, UV Autotracker III). This doubled light was then added to the remaining dye laser fundamental (via a BBO crystal in an identical Autotracker device) to produce a final output of 210.1 nm, with average pulse energy of 1.5 mJ, pulse widths of 7 ns, and a rate of 10 Hz.

Experiments were performed at aluminum surface temperatures of both 100 K and 500 K. The TOF-MS detection method was used to probe incident and scattered Cl_2 species, as well as abstraction (Cl) and desorption (Al_xCl_y) products. Sample temperature, just like incident beam energy, allows for the elucidation of energy-dependent effects, such as kinetic barriers to adsorption, reaction, and desorption, helping to decipher the various mechanisms involved.
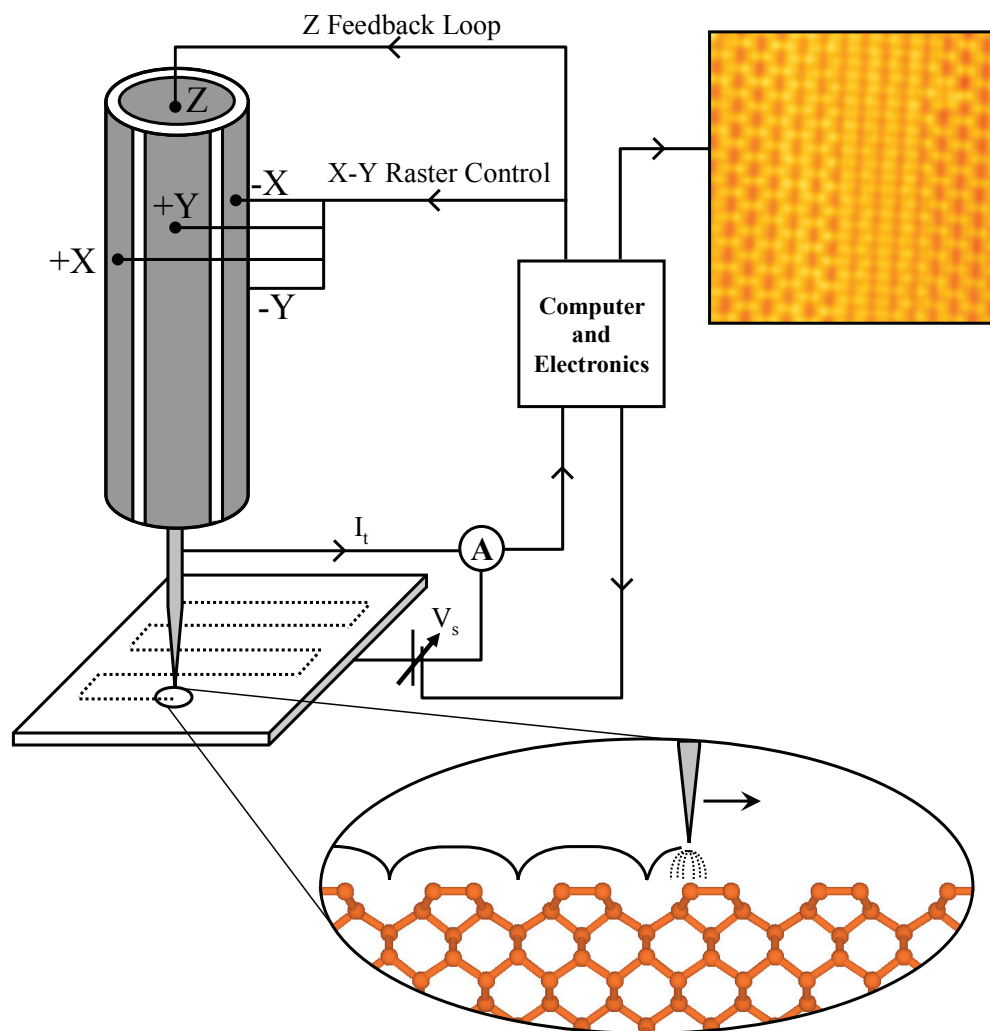
FIGURE 2.1. Schematic diagram of the scanning tunneling microscope (STM), scanning the Ge(100)-2×1 surface.
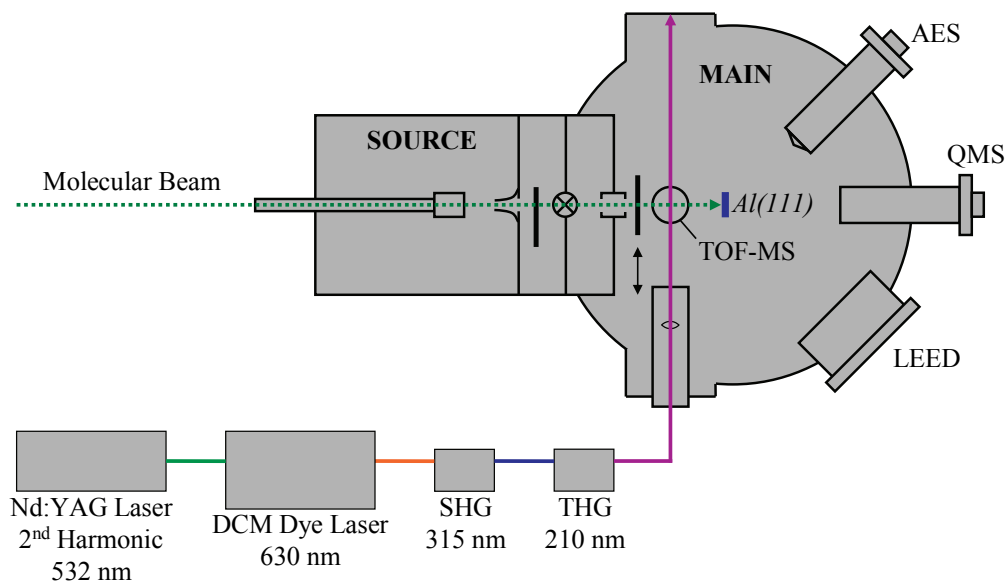
FIGURE 2.2. Schematic diagram of the vacuum chamber used for Cl₂/Al(111) experiments, including the molecular beam and laser paths.
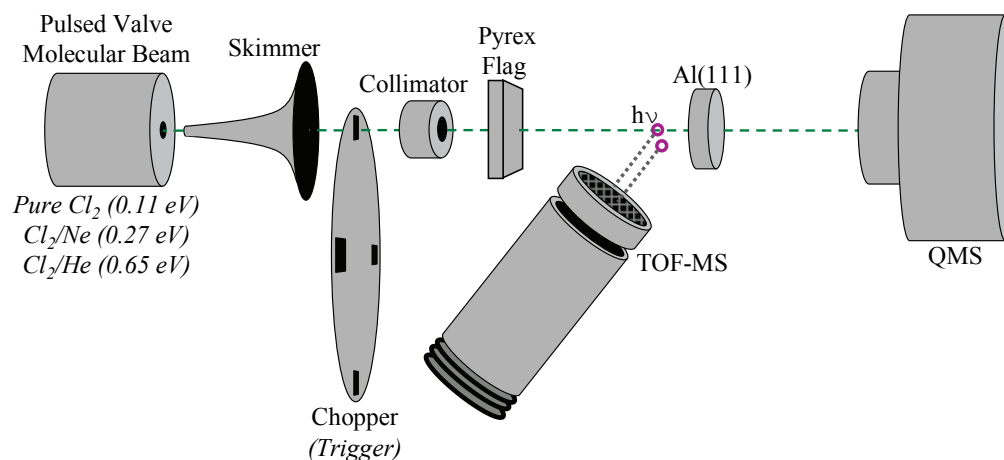
FIGURE 2.3. Schematic diagram of the molecular beam path. Note the indication of the laser ionization spots for the incident Cl_2 beams (top spot) and the desorbed aluminum chlorides (bottom spot), and the location of the time-of-flight mass spectrometer tube.

Pulsed laser
ionization

Ion pulse

Acceleration
region

AlCl⁺

Drift region

Cl⁺

Al⁺

Electron multiplier
(detector)
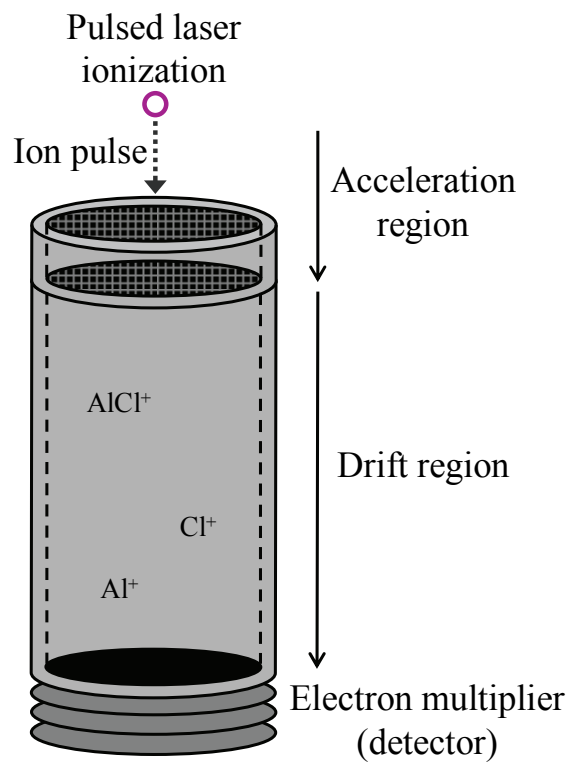
FIGURE 2.4. Schematic diagram of a standard time-of-flight mass spectrometer.

2.5 REFERENCES

[1]   L. H. Chan, E. I. Altman, and Y. Liang, J. Vac. Sci. Technol., A **19** (3), 976 (2001).

[2]   C. O. Chui, H. Kim, D. Chi et al., IEEE Trans. Elec. Dev. **53** (7), 1509 (2006).

[3]   J. Tersoff and D. R. Hamann, Phys. Rev. Lett. **50** (25), 1998 (1983).

[4]   J. Tersoff and D. R. Hamann, Phys. Rev. B **31** (2), 805 (1985).

[5]   J. A. Strosico and R. M. Feenstra, in *Scanning Tunneling Microscopy*, edited by J. A. Strosico and W. J. Kaiser (Academic Press, San Diego, 1993).

[6]   A. Selloni, P. Carnevali, E. Tosatti et al., Phys. Rev. B **31** (4), 2602 (1985).

[7]   N. Li, M. Zinke-Allmang, and H. Iwasaki, Surf. Sci. **554** (2-3), 253 (2004).

[8]   N. D. Lang, Phys. Rev. B **34** (8), 5947 (1986).

[9]   R. M. Feenstra, J. A. Stroscio, and A. P. Fein, Surf. Sci. **181** (1-2), 295 (1987).

[10] P. Hohenberg and W. Kohn, Phys. Rev. **136** (3B), B864 (1964).

[11] W. Kohn and L. J. Sham, Phys. Rev. **140** (4A), A1133 (1965).

[12] G. Kresse, Thesis, Technische Universität Wien, 1993.

[13] G. Kresse and J. Furthmüller, Comp. Mat. Sci. **6** (1), 15 (1996).

[14] G. Kresse and J. Furthmüller, Phys. Rev. B **54** (16), 11169 (1996).

[15] G. Kresse and J. Hafner, Phys. Rev. B **47** (1), 558 (1993).

[16] J. Paier, R. Hirschl, M. Marsman et al., J. Chem. Phys. **122** (23), 234102 (2005).

CHAPTER THREE

An Atomic View of Fermi Level Pinning of Ge(100) by O$_2$

3.1 ABSTRACT

We have performed an atomic-level study of the structure and electronic properties of the oxidation of the Ge(100) surface using STM and STS experiments and DFT modeling. Room-temperature O$_2$-dosed Ge(100) surfaces at sub-monolayer coverages (with and without post-oxidation anneals at 300ºC - 500ºC) were imaged via STM in order to identify the bonding geometries of the oxidation reaction products, and STS spectra were taken for the characterization of the surface electronic structures resulting from those structures. DFT modeling was performed on the various adsorbate structures in order to both elucidate the most likely bonding geometries and compare computed densities-of-states to measured STS spectra. The O$_2$-reacted Ge(100) surfaces, pre- and post-annealed (325ºC), were found to exhibit Fermi level pinning near the valence band. Proper Fermi level position was restored upon desorption of the GeO at temperatures above 425ºC. DFT results indicate that the pinning is most likely due to a strong coverage effect, wherein coverages of ≥0.5 ML of GeO on the surface are found to induce large near-E$_F$ densities of states, while lower coverages (0.25 ML) do not seem to be as problematic, in addition to local oxygen-induced bond strain.

3.2 INTRODUCTION

Due to the approach of the fundamental limits of classical silicon CMOS scaling, recent years have seen a great deal of work focused on alternative channel materials for high-speed MOS-type field-effect transistors. One such alternative material is germanium, whose greater low-field intrinsic carrier mobilities may provide for a significant increase in saturation current over state-of-the-art silicon MOSFET devices. However, in contrast to Si, Ge does not have a suitably stable electrically-passivating native oxide. The Ge native oxide, GeO_2, is both water-soluble and thermally unstable at elevated temperatures; GeO_2 decomposes and desorbs as GeO above 400ºC.[1-3] Therefore, an alternative dielectric and/or electrical passivation method is needed.

Numerous experiments have attempted the fabrication of Ge-based MOSFET or MOSCAP devices using a great diversity of insulators, including GeO_2,[4-6] Ge_3N_4,[7] GeO_xN_y,[5,8,9] SiO_2 (with and without a Si interlayer/cap),[10,11] and high-k metal-oxides ($BaStTiO_3$, ZrO_2, HfO_2).[12-14] The success (or failure) of these different dielectric materials has been found to depend on the chemical passivation of the Ge at the semiconductor-oxide interface. In general, devices that were fabricated with interfacial GeO_2 were consistently found to yield poor C-V (capacitance-voltage) characteristics; large frequency dispersion in accumulation, capacitance peaks within the band gap, gate leakage, and/or flatband shifts, all of which are associated with interfacial or oxide traps and fixed charge. Those devices that were fabricated with no interfacial GeO_2 were found to exhibit superior C-V characteristics. From these C-V studies, one can conclude that even the highest-quality GeO_2, regardless of further dielectric growth or deposition,

makes for a very low-quality passivant. However, it is unknown if the GeO_2/Ge trap state formation and associated Fermi level pinning is due to the formation of Ge-O bonds or due to the properties of bulk GeO_2; it is critical to determine if Ge-O bonding alone can pin the Fermi level, as this will help determine if other oxides can be directly deposited on Ge while retaining a passive interface.

While Ge-O bonding might pin the Fermi level, we note that the pinning may not be intrinsic to all Ge-O bonds on the Ge(100) surface. For example, while the GeO_2/Ge interface is pinned a ZrO_2/Ge interface may be unpinned, even though both interfaces contain Ge-O bonds. Furthermore, even for a given interface, the deposition method can change the electronic structure because the bonding geometries of adsorbates on surfaces play a definitive role in the determination of the electronic properties of the resultant interfaces. This is an especially important issue in the consideration of electrical passivation of semiconductor surfaces, where bond angles and coordination numbers can have a large effect on the electronic structure. Therefore, a thorough characterization and understanding of the effect of Ge-O bonding at the Ge(100) surface is paramount for understanding the interfaces made with potential gate dielectric oxides for Ge-based MOSFET devices.

Much work has been performed over the past decade using STM-based experiments to characterize the initial oxidation of the Ge(100)-2×1 surface, including the effect of post-oxidation annealing and elevated-temperature oxidation.[15-21] A few studies utilizing density functional theory modeling have also been produced,[22,23] but these have mostly concentrated on the initial metastable oxygen adsorption sites. While these various works have provided much insight into the physical nature of the Ge(100)

oxidation reaction, a thorough and unambiguous identification of the various adsorbate and reaction product geometries has remained elusive, as well as has a characterization of electronic structure of the oxidized Ge(100) surface.

We have performed an atomic-level study of the structural and electronic properties of the O_2 oxidation reaction on the Ge(100) surface utilizing scanning tunneling microscopy (STM), scanning tunneling spectroscopy (STS), and density functional theory (DFT) modeling, in order to get at a fundamental understanding of the atomic geometries of the surface binding sites (STM, DFT) and the resultant electronic structure of those sites (STS, DFT). Long, low-temperature post-oxidation anneals allowed us to eliminate various metastable and/or transitional reaction sites so that the effect of specific reaction products on the electronic structure could be elucidated. For definitive determination of the effect of O_2 dosing and annealing on the electronic structure, we measured the STS spectra on the clean and O_2 dosed surfaces of both *n*-type and *p*-type substrates, and modeled the observed reaction sites with DFT to help better characterize the physical and electronic structures.

3.3 METHODS

A. Experimental Setup

All experiments were performed under ultra-high vacuum (UHV) conditions with a base chamber pressure of $2 - 3 \times 10^{-10}$ Torr. The UHV chamber is equipped with a water-cooled manipulator and sample holder, a differentially-pumped ion gun (VG Microtech EX05), a custom-built differentially-pumped deposition source chamber

(allowing for the low-background pressure deposition of various oxides from high-temperature effusion cells), a room-temperature scanning tunneling microscope (Park Scientific Autoprobe VP1), and a standard set of analytical instruments: Auger electron spectrometer (AES), low-energy electron defractometer (LEED), and quadrupole mass spectrometer (QMS).

Experiments were performed on 6 mm × 18 mm samples cut from n-type (Sb-doped, 1.88×10^{17} – 1.54×10^{18} cm^{-3}, 0.020 – 0.005 Ω-cm) and p-type (Ga-doped, 1.58×10^{17} – 1.12×10^{18} cm^{-3}, 0.040 – 0.010 Ω-cm) 100 mm Ge(100) wafers purchased from Wafer World (epi-grade, ±1° orientation tolerance). The samples were lightly cleaned of oils and particles using a lint-free cloth wetted with methanol or isopropanol prior to insertion into the vacuum chamber. The Ge(100) samples were prepared by successive sputter/anneal cycles of the following recipe: sputtering at normal incidence with 800 – 1000 V Ar$^+$ ions at a sample temperature of 500ºC, followed by resistive annealing at 700ºC for 20 minutes, with a 1ºC/min ramp down to room temperature. Typically, about three such cycles were required to reach peak surface cleanliness and order. This treatment produced large, well-ordered, defect-free terraces. Surface cleanliness and order was checked with Auger electron spectroscopy, low-energy electron diffraction, and scanning tunneling microscopy (STM).

Following a successful STM-based check for surface cleanliness and order and an STS check for electronic structure, the sample was then dosed with pure O$_2$ via a leak-valve in the main UHV chamber (either with the sample still on the STM stage or after being picked up with the manipulator). Subsequently, the dosed sample was either transferred back to the STM for scanning of the room-temperature reacted surface, or

annealed at temperatures ranging between 300ºC and 500ºC before being returned to the STM.

Filled-state constant-current STM images were generally taken at -1.8 V – -2.0 V sample bias and 0.2 – 0.5 nA tunneling current with electrochemically-etched tungsten tips. Scanning tunneling spectroscopy (STS) was performed using the variable tip-sample separation method developed by Feenstra *et al.*, yielding a unitless spectrum that is an approximation to the surface density of states[24-30] (which were subsequently normalized to unity). A 1.4 kHz, 0.2 V sine-wave was used for the bias modulation, and the signal was extracted with a digital lock-in amplifier (Stanford Research Systems SR850).

B. Computational Details

All density functional theory (DFT) calculations presented in this paper were performed using the Vienna Ab-Initio Simulation Package (VASP)[31-34] in the generalized gradient approximation (PBE exchange-correlation functional), with projector augmented wave (PAW) potentials[35,36] (as supplied by the VASP group), a 4×4×1 Monkhorst-Pack k-point mesh generation scheme (for a total of 4 irreducible k-points), and plane-wave basis cut-off of 450 eV. All parameters (i.e. k-points, cut-off energy, vacuum space, slab thickness, etc.) were chosen such that they were each individually converged to within 1 meV/atom for the system of study. The absolute error of this type of calculation is estimated to be up to 0.37 eV,[37] but it is difficult to say exactly what this error is with respect to the O/Ge(100) system presented here. Regardless of absolute numerical accuracy, the qualitative results from these calculations should be quite reasonable

because comparisons are being made merely between different bonding geometries that have all been calculated under identical conditions and with similar types of bonds. Therefore, the calculations in this paper should have good relative accuracy, with an estimated relative error of $\pm$ 0.1 eV.[38]

The system studied consisted of an Ge(100) slab supercell with a 4×2 surface dimer reconstruction, as this is the lowest energy configuration (compared to the 2×1 flat dimer and 1×1 unreconstructed geometries). The germanium slab was 8 atomic layers thick, with each layer being 2×4 atoms in area, for a total of 64 Ge atoms per unit cell (for the clean, Ge surface/substrate calculations). The bottom of the slab was unreconstructed and terminated with 16 hydrogen atoms (two H atoms per Ge). The clean Ge supercell contained 12 atomic layers of vacuum space in the z-direction. The bottom three Ge layers were constrained to the minimum-energy bulk DFT geometry, which was found through a series of bulk Ge calculations to have a lattice parameter of 5.795 Å (2.6% larger than the experimental result of 5.646 Å due to the well-known GGA overestimation of lattice parameters). The terminating H atoms were initially allowed to relax and were kept fixed at these optimized positions for all subsequent calculations. All other atoms (upper substrate, adsorbate, gas-phase) were allowed to structurally relax with respect to interatomic forces to a tolerance of 0.01 eV/Å.

DFT-based STM simulations are produced using the Tersoff-Hamann approach, wherein the charge density is calculated for the energy range of interest – in this case 0 eV to -2 eV to match the STM conditions – and an isodensity plot of the computational slab surface is produced as an approximation to a constant-current style STM image. In order to try to best match the sites observed in the experimental STM images, both 2×1-

and 4×2-based sites were modeled. That is, because the 4x2 dimers on the experimental Ge(100) surface buckle rapidly at room temperature, and faster than the sampling time of the STM, they appear to consist of flat 2x1 dimers. Thus, it was found that a combination of 4x2- and 2x1-based STM simulations was needed to provide a full, consistent picture of the various sites observed on the oxidized Ge(100)-2×1/4×2 surface. It must be noted, however, that while STM simulations were generated for both the 2×1 and 4×2 reconstructions, only the energies for the 4×2 sites are considered in this report, as the clean Ge(100)-4×2 reconstruction is the energetically preferred surface (i.e. adsorption energies calculated from the 2×1 sites are not consistent with experiments). All of the STM simulations presented in this report were generated with the same contrast (i.e. color minima and maxima) as the clean Ge simulations for the sake of direct comparison.

3.4 RESULTS AND DISCUSSION

A. O/Ge(100) Adsorbate Bonding Geometry Characterization

1. Clean Ge(100)-2×1/4×2

Figure 3.1a is a typical filled-state STM image of the clean Ge(100)-2×1 surface. The 2×1 dimer row reconstruction is a 4×2 buckled dimer reconstruction with a low activation energy to intra-dimer rocking (giving it an overall 2×1 periodicity and making the dimer rows appear flat). In addition to the flat-looking 2×1 rows, one can also see other rows, as well as small domains, where the 4×2 buckled dimer configuration has been frozen due to stabilization by step-edge and/or lattice defects; this is also observed

on Si(100) at cryogenic temperatures. Also in Fig. 3.1a are DFT-based STM simulations of the 2×1 and 4×2 reconstructions, overlayed on 2×1 and 4×2 regions of the surface, respectively.

Fig. 3.1b displays ball-and-stick models of the top three layers for the two different dimer reconstruction geometries. We note that the 4×2 buckled dimer structure is significant because it is accompanied by electron transfer from the "low" dimer atoms to the "high" dimer atoms, which changes the reactivity of the two respective dangling bonds.

2. Room-Temperature Oxidized Ge(100)

Figure 3.2 is a typical filled-state STM image of the Ge(100)-2×1 surface after exposure to 100 L O_2 at room temperature (no post-oxidation anneal). Two main types of sites, with two sub-types each, are found on the unannealed oxidized surface: "bright sites", which image above the original Ge(100) lattice, and "dark sites", which image below the original Ge(100) lattice. According to the site designation nomenclature introduced by Fukuda, the four different site sub-types indicated in Fig. 3.2 are as follows: type A (square), type B (hexagon), type C (diamond), and type D (circle).

There are two distinct types of bright sites observable with STM on the room temperature oxidized Ge(100) surface; these sites can be clearly differentiated by line scan analysis. The brighter and larger of the two, type A, are found to image 1.2 – 1.4 Å above the surface (the dimer plane), which is consistent with the Ge(100) step height, indicating that these sites are Ge adatoms. The dimmer and smaller of the two sites, type B, are found to image at a range of about 0.6 – 0.9 Å above the surface. These sites are

consistent with metastable oxygen adsorption sites – the dimer adsorption/insertion site and the back-bond insertion site – suggested by previous theory work.[22,23] In these sites a single O atom inserts into a Ge-Ge bond without displacing any Ge atoms. Insertion into and adsorption onto the surface dimers is denoted as "dimer insertion" and "dimer adsorption," respectively, while insertion into the bond between 1st and 2nd layer Ge atoms is denoted as "backbond insertion." As can be seen by the STM simulations in Table 2.1, the dimer insertion site is unlikely to be observable in the experimental images, but the dimer adsorption and backbond insertion sites should be visible.

There are also two different observable dark sites. Type C sites exist on the edge of the dimer row and image about 0.6 Å below the surface. They are somewhat difficult to distinguish between the "holes" formed by buckled dimers, but they do image slightly deeper and more distinct. These sites also seem to help stabilize the dimer buckling, locking it into place. This site is consistent with a single oxygen displacement site, where a single Ge atom has been displaced by an oxygen atom, producing type A sites. Type D sites image as a dark cut across the dimer row 1.0 – 1.2 Å deep below the surface. This site is consistent with a double oxygen displacement site, where a full Ge dimer has been displaced by two oxygen atoms, also producing type A sites. Both types of dark sites have previously been reported to image as bright sites in empty-state imaging, confirming the presence of oxygen rather than being merely missing Ge defects.[17,20]

In order to provide additional evidence for the identification of the various features observed in the STM images, DFT modeling was employed to simulate the various O/Ge(100) reaction sites suggested by experimental results, standard chemical reasoning, and claims in the literature. Figure 3.1 provides the results from the DFT

modeling of the observed and suggested reaction sites from the O/Ge(100) oxidation process, including ball-and-stick diagrams of the surface bonding configurations, STM simulations (with the computational unit cell indicated by the dashed red line), and calculated adsorption enthalpies. Note that these calculations were performed at a coverage (25%) such that the adsorbate and/or reaction sites were not adjacent within the computational unit cell, making them essentially isolated.

Adsorption enthalpies were extracted from the computational work using the Hess's law method of "products minus reactants." The calculated values can strongly indicate which of the potential simulated geometries are thermodynamically favorable (and therefore stable at room temperature and above) and those that are unlikely to occur. The reported adsorption enthalpies are per adsorbed O atom, with respect to an O_2 molecule reactant. Reaction sites that involve the displacement of Ge atoms from the surface to form ad-atoms and/or ad-dimers are calculated with respect to the formation of ad-dimers, as ad-dimers are the lower energy configuration of the two ad-species (-0.78 eV decrease in total energy due to dimerization). This combination of experiment and theory allows for the unambiguous assignment of low-coverage O_2 reaction sites and resultant bonding geometries.

All of the calculated adsorption enthalpies indicate room and somewhat elevated temperature stability, with dimer and low backbond insertion yielding the highest adsorption enthalpies, -2.65 eV and -2.43 eV, respectively, and the high and low single displacement geometries having the lowest, -1.87 eV and -2.02 eV, respectively. It is interesting that the displacement sites, especially the full dimer displacement, with an adsorption energy of -2.11 eV, show lower enthalpies than the insertion sites, though this

result is consistent with the initial-stage oxidation mechanism calculations reported by Soon *et al*[23] (though their calculations utilized Gaussian-type basis sets and were performed on Ge clusters). The STM simulations indicate a very subtle appearance for the single displacement sites in the experimental images, so it is difficult to quantify the site surface coverage. The dimer displacement sites, however, are quite obvious in both the simulations and the experimental images, and they are of significant coverage. We suspect that the reaction to form the dimer displacement sites, rather than merely insertion sites, is stabilized by entropy effects. That is, each O atom may reversibly sample any of the insertion reaction products before settling on the dimer or low backbond insertion, but any displacement sites sampled are final products by the nature of their irreversibility because the Ge atom that gets displaced is essentially removed from the reaction environment.

3. Annealed Oxidized Ge(100)

Following the work of Fukuda *et al,* the oxidized samples were annealed at 325ºC, well below the GeO desorption temperature of about 425ºC.[15,17,19,20] By annealing the oxidized sample, many of the different reaction sites could be eliminated so that the effect of particular reaction sites on the electronic structure could be elucidated. The 325ºC anneal converts the oxygen insertion sites (B sites) to displacement sites, and coalesces the individual oxygen displacement sites (sites C and D) into mostly long rows. The dark rows consisted of single atomic width rows and double atomic width rows (designated as S and 2S rows by Fukuda). These extended dark sites have been previously verified as oxide structures with ultraviolet photoelectron spectroscopy

(UPS).[19] The continued presence of oxygen on the surface after the long, low-temperature anneal was also verified for this work by performing temperature programmed desorption (TPD) while monitoring O, O_2, GeO, and GeO_2 with a quadrupole mass spectrometer (QMS); GeO was found to be the only detectable desorption product, and only began to appear after reaching a surface temperatures above ~425ºC, consistent with our 325ºC anneal allowing oxygen to remain on the surface while eliminating the metastable sites.

In contrast to Fukuda *et al*, however, we performed much longer anneals (20 minutes vs. 5 minutes). It was found that if the room-temperature oxidized sample was subjected to this longer anneal time, the O dark sites coalesced into much longer rows than reported by Fukuda (up to and over 500 Å), and the Ge ad-atom reaction products tended to either coalesce into larger regrowth areas or were diffusively driven to the step edges, leaving behind very few isolated Ge ad-atoms or ad-dimers compared to the as-is room temperature oxidized surface. Shorter anneal times were found to yield surfaces still containing most of the Ge ad-structure (ad-atoms, ad-dimers, small regrowth islands) on the terraces and shorter O dark site rows. Figure 3.3a is a high-resolution STM image of the extended dark-site structures resulting from this procedure. Because the dark O-related sites also coalesce into larger regions, the STM tip is allowed better access, and some structure can actually be seen in these regions.

In order to try to model higher local dimer displacement coverages, as well as the coalesced oxide dark row features observed on the post-annealed oxidized Ge(100) surface, higher coverage (50%) dimer displacement features were considered. Given the unit cell size and geometry (four Ge-Ge dimers), this allowed for the modeling of three

different simple dimer displacement-type configurations: checkered dimer displacement, perpendicular dimer displacement, and row dimer displacement. Table 2 contains space-filling models of the three 50% coverage geometries and their calculated enthalpies of adsorption.

The enthalpies of adsorption for the checkered and perpendicular dimer displacement geometries are degenerate with the single dimer displacement configuration (-2.09 and -2.10 eV/O vs. -2.11 eV/O), but the row dimer displacement geometry is much less stable (-1.41 eV/O) due to considerable bond strain felt by the O atoms. At such a low energy we would not actually expect such row dimer displacement features to actually form, especially at elevated annealing temperatures. Additionally, neither the geometry nor the STM simulation of the row dimer displacement geometry is entirely consistent with the dark row structures seen in the post-annealed STM images. Therefore, we can only assume that the coalesced oxide dark row structures are more complicated than the simple model suggested here.

Finally, upon annealing the oxidized sample to temperatures above ~425ºC, the clean surface could be recovered due to desorption of all of the GeO reaction products, as verified by TPD, and a reorganization of the surface to fill in the surface vacancies (see Figure 3.3b). Recovery of the clean surface was possible regardless of whether the oxidized surface was low-temperature annealed or left as-is after room temperature O_2 exposure.

B. O/Ge(100) Electronic Structure Characterization

1. Experimental Surface Electronic Structures

Scanning tunneling spectroscopy (STS) measurements yield (dI/dV)/(I/V) curves that give an approximation to the local surface density of states.[24-30] Therefore, these spectra possess the same features as a standard DOS plot, namely a valence band, conduction band, band gap, and Fermi level. The Fermi level is found at the zero volt position, while a negative sample bias probes "filled" electronic states (valence band, VB), and a positive sample bias probes "empty" electronic states (conduction band, CB). In between the finite VB and CB DOS edges is the band gap (i.e. where the DOS is equal to zero). Therefore, in STS spectra, a *p*-type sample has a Fermi level position near the VB and an *n*-type sample has a Fermi level position near the CB. It is this property that will be employed in this work, since a misplaced Fermi level is consistent with electronic pinning due to a high density of surface states within the band gap.[39,40] STS experiments have been performed on both *p*- and *n*-type Ge(100)-2×1/4×2 surfaces under various conditions (clean, room-temperature oxidized, post-oxidized annealed, and oxide-desorbed clean).

Figure 3.4a presents spectra for clean *p*- and *n*-type Ge(100)-2×1/4×2 surfaces. For the clean *p*-type sample the Fermi level is found to be located near the VB (negative sample bias), and for the clean *n*-type sample the Fermi level is located near the CB (positive sample bias).

Figure 3.4b presents STS spectra taken on the room-temperature oxidized *p*- and *n*-type Ge(100) surfaces after exposure to 100 L of O_2 (corresponding to a surface

coverage of about 20%), without post-oxidation anneal. The *p*-type surface displays a Fermi level position near the VB, the same as on the clean surface, but the *n*-type surface Fermi level is also found near the VB, opposite to what is seen on the clean surface. These results indicate Fermi level pinning due to the oxidation of the surface. These results are found to be repeatable at O_2 exposures at least as low as 10 L, corresponding to a surface coverage of about 2%.

Because the existence of both oxygen adsorption sites and displaced Ge adatoms on the as-oxidized Ge(100) surface makes it difficult to pin-point the cause of the Fermi level pinning, the oxidized samples were annealed for long times at low temperature (20 minutes at 325ºC) to remove the Ge ad-atoms and metastable O adsorbates from the terraces. STS spectra taken on the post-annealed samples (Fig. 3.4c) reveal the same Fermi level pinning as observed on the as-oxidized samples: both the *p*- and *n*-type samples display a Fermi level position near the VB.

Finally, the samples were annealed at sufficiently high temperature ($\geq$ 425ºC) to desorb the GeO oxidation products completely from the surface. STS spectra taken on these desorption-cleaned samples (Fig. 3.4d) reveal recovered electronic structures identical to that observed on the clean surface: the *p*-type samples display a Fermi level position that is still near the VB, and the *n*-type samples display a Fermi level that has returned to the original clean-surface position near the CB.

2. *Theoretical Electronic Structures*

Densities of states were calculated from the previously-discussed oxidation reaction product DFT simulations in order to provide further insight to the effect of

oxidation on the Ge(100) electronic structure. It must be noted, however, that there are well-known problems with standard LDA- and GGA-based DFT with respect to the electronic structures of semiconducting and insulating materials, namely a general underestimation of the band gap by 30 – 100%, due to the approximation of the exchange potential.[41,42] Unfortunately, this problem is at its worst for small band gap semiconductors, such as germanium. In fact, standard DFT predicts a slight overlap of the Ge VB maximum and CB minimum, producing a semi-metallic electronic structure (see Figure 3.5a).

However, because there is still a significant minimum in the DOS at the Fermi level, it is possible to extract useful information from standard DFT calculations of Ge(100). Specifically, we compare the calculated DOS of the clean Ge(100)-4×2 slab with the DOS of the various Ge(100) slabs with oxygen adsorbates on them. We note that we can check the validity of this approach because we have the experimental STS data for comparison. Because we are particularly interested in the induction of electronic states within the band gap, a potential cause of Fermi level pinning, special attention will be paid to the near-Fermi level region of the calculated densities of states. There are two general changes to the DOS induced by the addition of oxygen adsorbates to the Ge(100) surface: (a) the DOS at the near-E_F region decreases (or exhibits no change) after the addition of the oxygen induced sites, or (b) the DOS at the near-E_F region increases after the addition of oxygen induced sites. If the DOS decreases or shows no change, it is reasonable to conclude that the reaction site is not a potential source of Fermi level pinning, while if the DOS increases it is reasonable to conclude that pinning is possible

because of the induction of band gap or band edge states that are consistent with Fermi level pinning.

It must be noted that, because of the small size of the computational slab (2×2 surface dimers, four dimers in total), the lowest site coverages that can be modeled are at 25% coverage. This coverage, in general, is greater than that actually utilized in the course of the experimental work performed in this study (~20%), but in some cases is relatively close.

Figure 3.6a presents the calculated DOS for the type A sites (Ge ad-atom and ad-dimer), along with the DOS of the clean Ge(100)-4×2 surface for comparison. It is quite clear that both ad-species cause a large disturbance of the near-E_F DOS. In both cases, this increased density is most likely due to the addition of dangling bonds to the surface. The dangling bonds on the clean Ge(100)-2×1/4×2 surface are not actually half-filled due to the charge transfer related to the buckling of the dimers, which causes one dangling bond (on the sp^3-like upper Ge) to be more than half full and the other dangling bond (on the sp^2-like lower Ge) to be less than half full (see the projected densities of states in Fig. 3.5b). It is likely this 4×2-based charge transfer that gives Ge(100) its semiconducting surface, as the transient flat 2×1-type dimers, with their half-filled dangling bonds, are believed to be the source of small metallic electronic states within the Ge band gap.[43] While one might expect Ge ad-atoms to pin the Fermi level because they have two half-filled dangling bonds, the pinning induced by the Ge ad-dimers is unexpected. However, the isolated ad-dimers are computationally predicted to be unbuckled, causing their dangling bonds to be half-filled, which will induce states in the band gap.

It must be noted, however, that these models do not necessarily accurately reflect the experimental room temperature oxidized surface, so the magnitude of the role played by the Ge ad-species is debatable. The coverage of Ge ad-atoms on the 100 L O_2-dosed surface room temperature surface is far below the computational coverage of 25%, and the actual coverage of ad-dimers is even smaller. The experimental coverage of these ad-species after annealing becomes nearly zero because the vast majority of the liberated Ge on the surface coalesces into large regrowth islands or diffuses to the step edges. Therefore, by coverage alone, both the Ge ad-species are expected to play a smaller, but not unimportant, role in the observed pinning than indicated by the computational results. The Ge ad-dimers are anticipated to play an even smaller role because of the likelihood of dynamic buckling on the experimental surface; while the ad-dimer was found to prefer the flat, symmetric dimer geometry in the 0 K computational environment (i.e. initially tilted ad-dimers always ended up relaxing to flat ad-dimers), resulting in the increased near-E_F DOS, this is not expected to be true in reality at non-cryogenic temperatures.

Figure 3.7 presents calculated densities of states for the type B oxidation sites on the Ge(100)-4×2 surface: dimer insertion, backbond (low) insertion, and backbond (high) insertion. The dimer adsorption case is not presented here, because it was not found to be stable on the 4×2 reconstructed surface. In all three systems the near-E_F DOS is unperturbed, and even slightly reduced, indicating that these sites are not inducing any states that could potentially pin the interface.

Figure 3.8 displays the calculated densities of states for the type C oxidation sites on the Ge(100)-4×2 surface: single displacement (low) and single displacement (high). It should be noted, however, that the designations of "low" and "high" for these two sites

indicate the starting point, or the Ge dimer atom that was displaced. The geometry wherein the high Ge was displaced was found to relax such that the O that did the displacement ends up in the low configuration in order to satisfy its desire for shorter bonds (Ge-O vs. Ge-Ge). Thus, the main difference between the two sites becomes one of registry within the slab supercell: the "low" geometry Ge-O heterodimer matches the original 4×2 registry (tilt direction), while the "high" geometry Ge-O heterodimer is in opposite registry to the original 4×2 configuration. It is this low geometry single displacement site that is found to induce a small state density in the near-E_F region, but of insufficient magnitude to be anything but a minor constituent of the observed Fermi level pinning.

One of the most common reactions sites on the room temperature oxidized surface is the type D site, or the single dimer displacement site. Figure 3.9a presents the calculated DOS for the single dimer displacement site, in comparison with the clean Ge(100)-4×2 surface, and shows a small but noticeable increase in near-E_F DOS for the single dimer displacement site.

Analysis of the projected densities of states (PDOS) for the affected surface atoms, displayed in Fig. 3.9b, helps to explain some of the reasons for this induction of states. The near-E_F PDOS for the two O atoms is surprisingly small, such that it probably has very little to do with the increase in the total DOS. However, the second layer Ge atoms to which the O atoms are bonded to (four in total, two distinct examples of which are presented in Fig. 3.9b) are found to posses a larger near-E_F PDOS than they would normally have (see Fig. 3.5b), with a decreased filled-state (VB) density and an increased empty-state (CB) density, due to the strong electron-withdrawing nature of the O atoms;

O has the second-highest electronegativity of all the elements. Interestingly, the largest near-E_F PDOS constituent for the single dimer displacement site actually belongs to the Ge atoms in the neighboring dimer (in the same row as the displaced Ge dimer, where the Ge atoms themselves are actually next-nearest-neighbors to the O atoms, and are therefore labeled as NNN-O in Fig. 3.9b). Comparison with the PDOS of the clean Ge dimers in Fig. 3.5b shows an increase in state density at the Fermi level for both NNN-O Ge atoms of at least a factor of two and a partial equalization of the empty-state and filled-state densities of the "high" and "low" Ge dimer atoms.

The cause of these changes can be elucidated with a simple analysis of the bonding geometries (bond lengths and angles) resulting from the formation of the single dimer displacement site. Figure 3.10 gives the calculated bond angles and bond lengths of the surface atoms of the clean Ge(100)-4×2 and the single dimer displacement surfaces. The 4×2 buckling of the clean Ge(100) surface is accompanied by a slight distortion of the second layer Ge atoms, allowing for the bond angles of the surface dimer atoms (with the two second layer Ge atoms to which they are bonded) to adjust.

The displacement of the Ge dimer with O atoms, however, forces a different sort of distortion due to the shorter Ge-O bond length. Because of the O-induced distortion, the bond angle of the high Ge dimer atom with respect to the second layer Ge atoms is increased by 16.1°, while the angle of the low atom increases by 1.5°. The dimer atoms' bond lengths are also stretched, by 0.24 Å for the high atom and 0.19 Å for the low atom. That is, the high atom is forced into a geometry more like that of the low atom, which explains why their respective densities of states become similar, and the Ge dimer itself approaches a configuration more like the flat dimer of the 2×1 surface (with the increased

near-E_F DOS). The Ge surface itself seems to be flexible enough to accept some of this distortion, as the single dimer displacement site DFT results do not indicate a huge induction of near-E_F DOS for this geometry, and as such appears that it may only be a small constituent of the Fermi level pinning of the room-temperature as-is oxidized Ge(100) surface.

When higher displacement site surface coverage is considered, however, large changes in the calculated densities of states, in comparison to the clean surface, become visible. Figure 3.11a displays the calculated densities of states for the three 50% coverage geometries: checkered dimer displacement, perpendicular dimer displacement, row dimer displacement. These geometries were intended to help model areas of high local concentrations of dimer displacement sites, as appears to be somewhat common on the as-is room temperature oxidized Ge(100) surface (i.e. checkered geometry), and very common on the low-temperature annealed oxidized surface (i.e. perpendicular and row geometries). As seen in Fig. 3.11a, all three geometries induce a significant density of near-E_F states. The causes for the increased DOS in the checkered and perpendicular dimer displacement geometries are the same as discussed for the single dimer displacement site (see PDOS for checkered geometry in Fig. 3.11b; note that the PDOS for the perpendicular site is nearly identical), except that the coverage is twice as high. Interestingly, however, the magnitude of the increase in DOS appears to be non-linear with coverage; the near-E_F DOS for the checkered and perpendicular dimer displacement geometries are actually a factor of three greater than that of the single dimer displacement geometry, rather than the expected factor of two due to the doubling of the site coverage.

While at first glance it would appear that the dimer row displacement is the most common of the O sites seen on the 325ºC annealed oxidized surface (the long, dark rows), as discussed previously the calculated enthalpy of adsorption, as well as the internal structure of the dark rows, indicates that this geometry is not likely. The structure of the coalesced oxide dark rows, as seen in the low-temperature annealed STM images, appears to be more complex than what we have currently modeled. As such we shall not consider the calculated electronic structure of this site any further than to say that the increased DOS seen in Fig. 3.11a is due to a combination of coverage (as was the case for the checkered and perpendicular geometries) and Ge-O-Ge bond strain, which is most likely the reason the enthalpy of adsorption is so low.

The exact nature of the oxide coverage effect is difficult to ascertain. However, as indicated by both experimental and computational results, it is most likely a combination of charge withdrawal by the electronegative oxygen atoms and strain within the local bonding environment due to the stringent bonding requirements of those same oxygen atoms. The large difference between equilibrium Ge-Ge bond lengths, 2.50 – 2.59 Å on the clean Ge(100) surface, and Ge-O bond lengths, 1.87 – 1.88 Å for the single dimer displacement site, certainly points the way to large amounts of localized bond strain, especially in areas of high O adsorbate concentrations. The high local concentrations of adsorbed oxygen, especially of displacement-type sites, on Ge(100) are also likely to cause a considerable withdrawal of charge from the germanium within the local area, thereby potentially inducing some amount of ionic bonding and exacerbating the bond strain issue. Perhaps the slightly shorter bond lengths in Si, with a lattice parameter 4% smaller than Ge, are enough to mitigate some of the same bond strain

problems. Although there must be other differences in the Si-O vs. Ge-O bonding, however, simply bearing in mind the considerable differences in bulk materials properties of SiO_2 and GeO_2.

3.5 CONCLUSIONS

We have found that both the room-temperature as-oxidized $Ge(100)$-$4\times2/2\times1$ surface and the post-oxidation 325ºC annealed surface suffer from Fermi level pinning, with the Fermi level pinned near the valence band for both *n*- and *p*-type $Ge(100)$ samples. While the as-oxidized surface contains too many various reaction sites to reliably identify the exact reason for the pinning, DFT modeling indicates that the pinning is most likely due to a combination of displaced Ge ad-species (ad-atoms, possibly flat ad-dimers) and areas of high concentrations of dimer displacement sites (because of a strong coverage effect, attributed to the strong electron withdrawing nature of oxygen). The low-temperature annealed surface, on the other hand, is mostly clear of the Ge ad-species, but still suffers from Fermi level pinning, apparently due to the extended GeO structures. We conclude that the structure and/or oxide content of these extended structures causes the Fermi level pinning due to an excess of local charge withdrawal and bond strain. These results help provide insight into the problem of germanium oxide formation at the dielectric-semiconductor interface in Ge-based MOSFETs.

3.6 ACKNOWLEDGEMENTS

Chapter 3, in part or in full, is in preparation for submission for publication in the Journal of Chemical Physics. The dissertation author is the primary investigator and author of this paper:

T. J. Grassman, S. R. Bishop, A. C. Kummel, "An atomic view of Fermi level pinning of Ge(100) by O_2." *In preparation for submission to the Journal of Chemical Physics.*

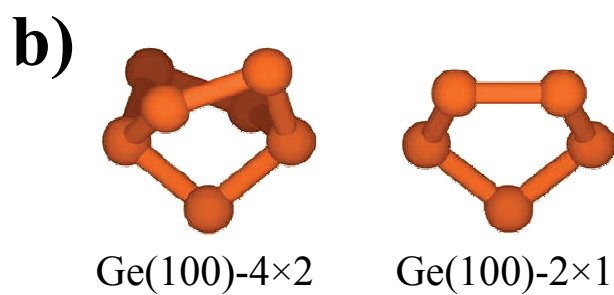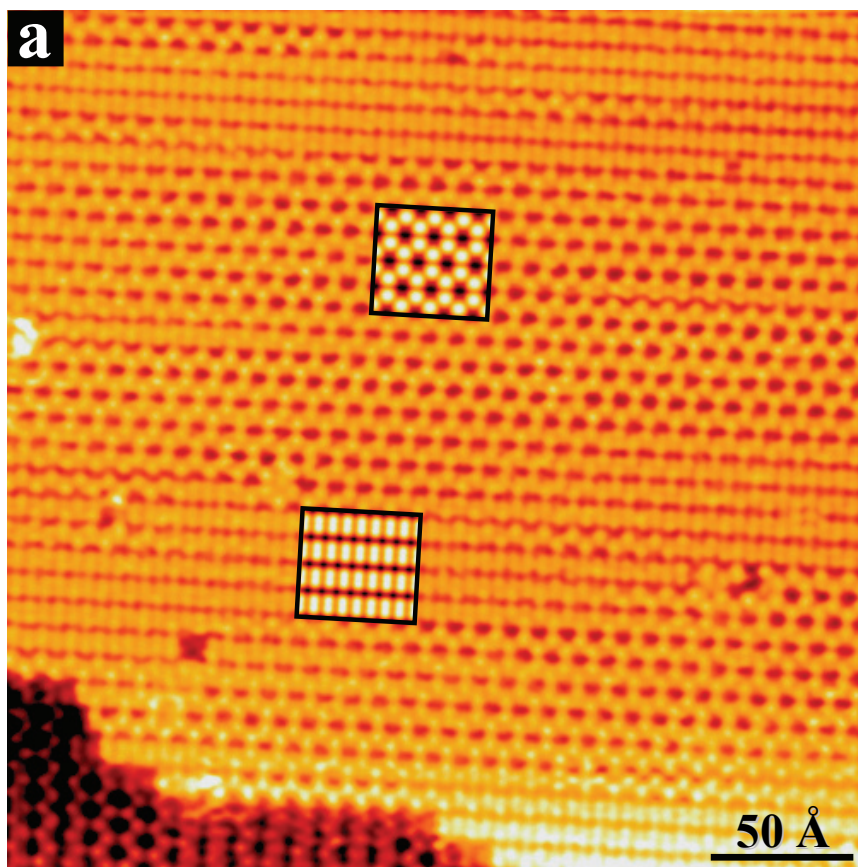FIGURE 3.1. (a) Filled-state STM image (V_s = -2.0, I_t = 0.2 nA) of the Ge(100)-2×1/4×2 surface with inlayed DFT-based STM simulations of the 4×2 (upper) and 2×1 (lower) regions. (b) Ball-and-stick diagrams of the 4×2 and 2×1 dimer reconstructions
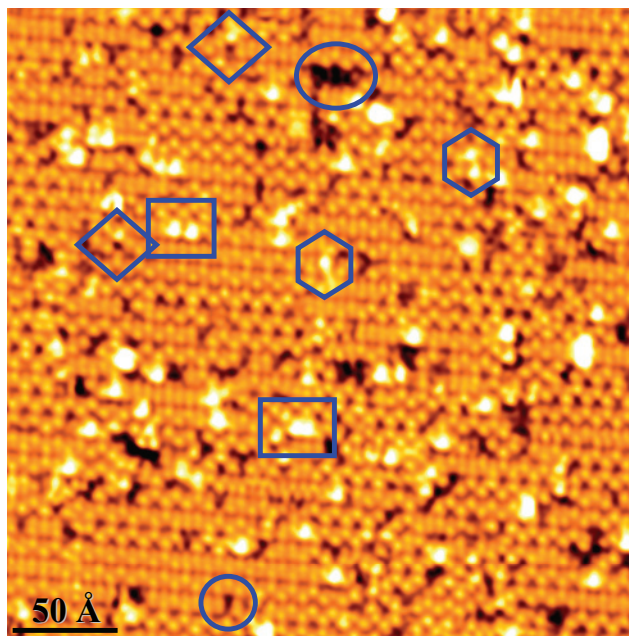
FIGURE 3.2. Filled-state STM image (V_s = -2.0 V, I_t = 0.2 nA) of room-temperature Ge(100) surface exposed to 100 L O_2. Examples of the major types of post-oxidation features (A, B, C, and D) are highlighted with geometric symbol.

TABLE 3.1. Summary of computational results for the post-oxidation features indicated in Fig. 3.2, including ball-and-stick diagrams for both 4×2- and 2×1-based geometries, STM simulations for both 4×2 and 2×1 geometries, and enthalpies of adsorption (only for 4×2). Enthalpies of adsorption are given per adsorbed O, and calculated with respect to molecular O_2 reactant and the formation of Ge ad-dimers.

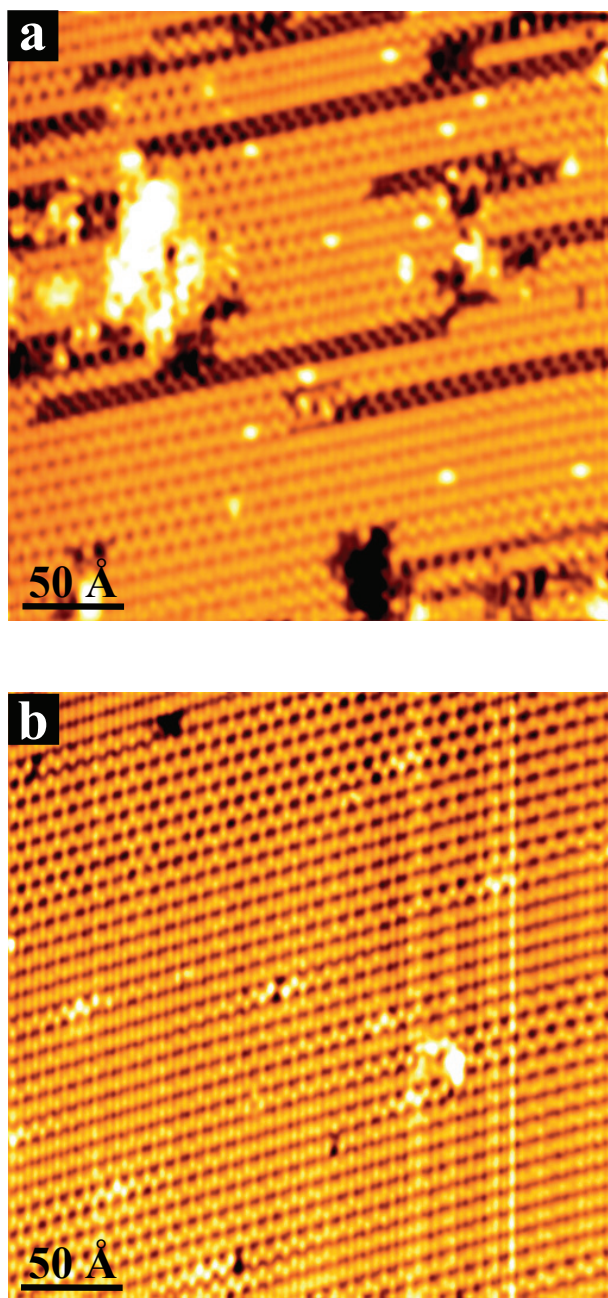| Identification		Geometry [4×2 | 2×1]	STM Simulations [4×2 | 2×1]	$\Delta H_{ads}^{4\times2}$ (eV)[a]
A	Ge ad-atom			N/A
	Ge ad-dimer			N/A
B	O insertion, *O adsorption*			-2.65
	O backbond (low, high)			-2.43, -2.17
C	O single displacement (low, high)			-2.02, -1.87
D	O dimer displacement			-2.11
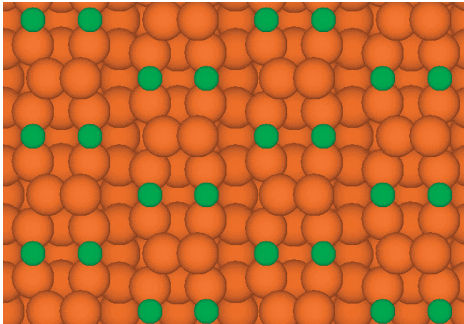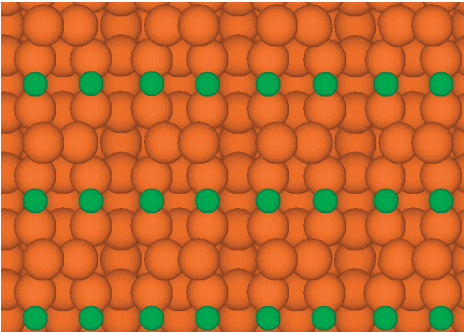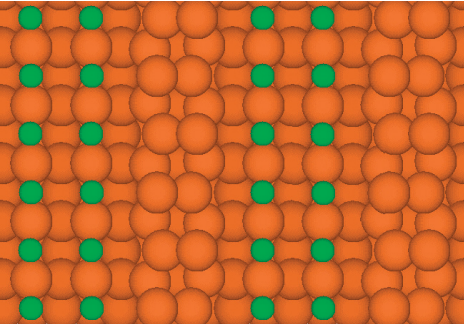
FIGURE 3.3. Filled-state STM images (V_s = -2.0 V, I_t = 0.2 nA) of 100 L O_2-dosed Ge(100) (a) after 20 min anneal at 325ºC and (b) after 5 min anneal at 500ºC.

TABLE 3.2. Summary of computational results for 50% coverage dimer displacement sites, including space-filling top-down diagrams of the geometries and calculated enthalpies of adsorption.

Identification	Geometry [4×2]	$\Delta H_{ads}^{4\times2}$ (eV)[a]
Checkered dimer displacement		-2.09
Perpendicular dimer displacement		-2.10
Row dimer displacement		-1.41

a: Calculated adsorption energies, ΔHads, are given only for the 4×2 surface sites. Values given are per adsorbed O atom, with respect to O2. Displacement sites are calculated with respect to the formation of Ge ad-dimers.
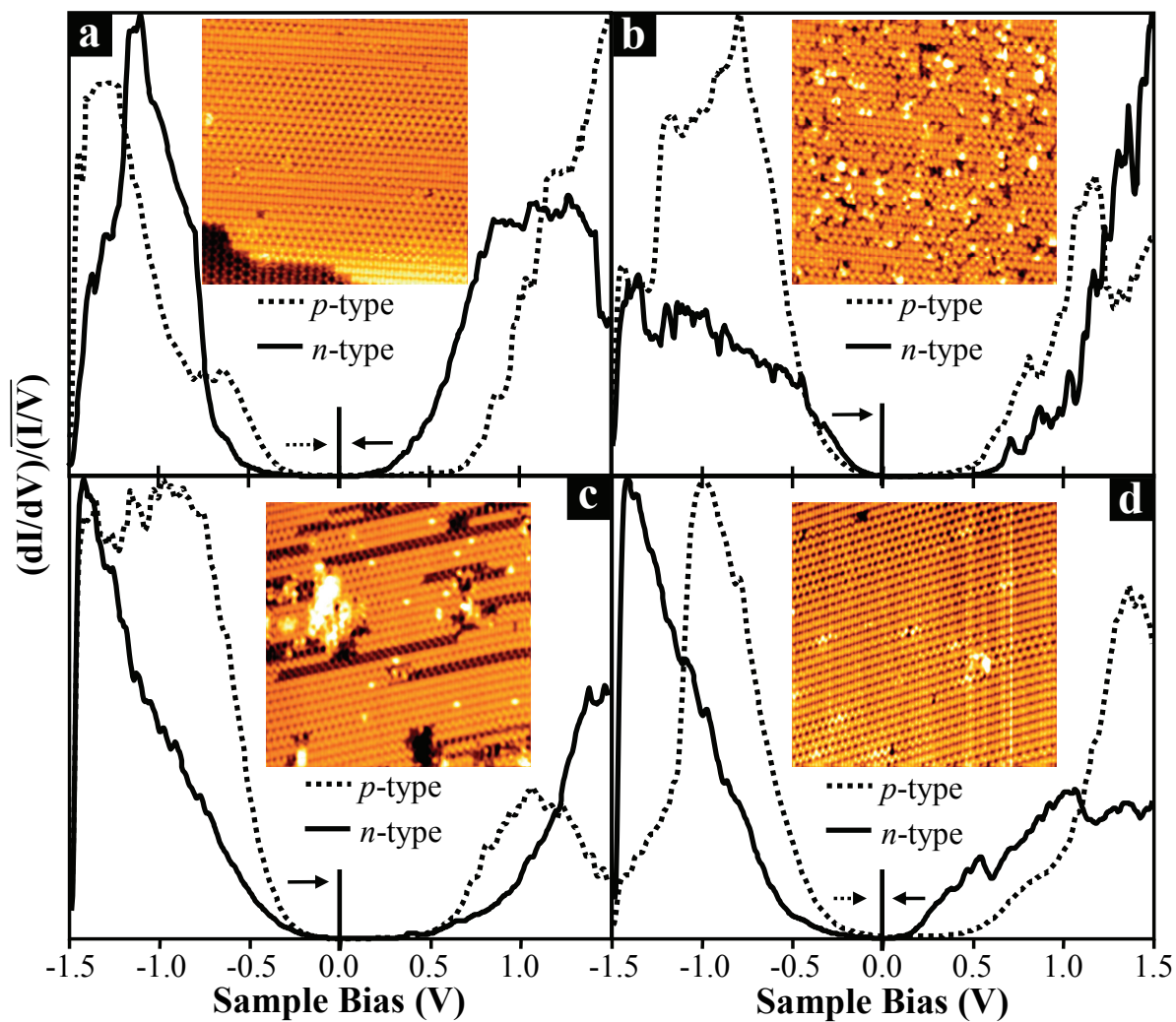
FIGURE 3.4. Scanning tunneling results, with inlayed associated STM image for reference, for both *p*- and *n*-type (a) clean Ge(100), (b) room-temperature 100 L O_2-dosed Ge(100), (c) room-temperature oxidized Ge(100) annealed to 325ºC, and (d) room-temperature oxidized Ge(100) annealed to 500ºC. Note that for both the clean (a) and re-cleaned (d) surfaces the Fermi level (0 V) lies near the valence band (VB) for *p*-type and conduction band (CB) for *n*-type, but for both room-temperature oxidized and post-annealed oxidized samples the Fermi level lies near the VB for both *p*- and *n*-type, indicating Fermi level pinning.
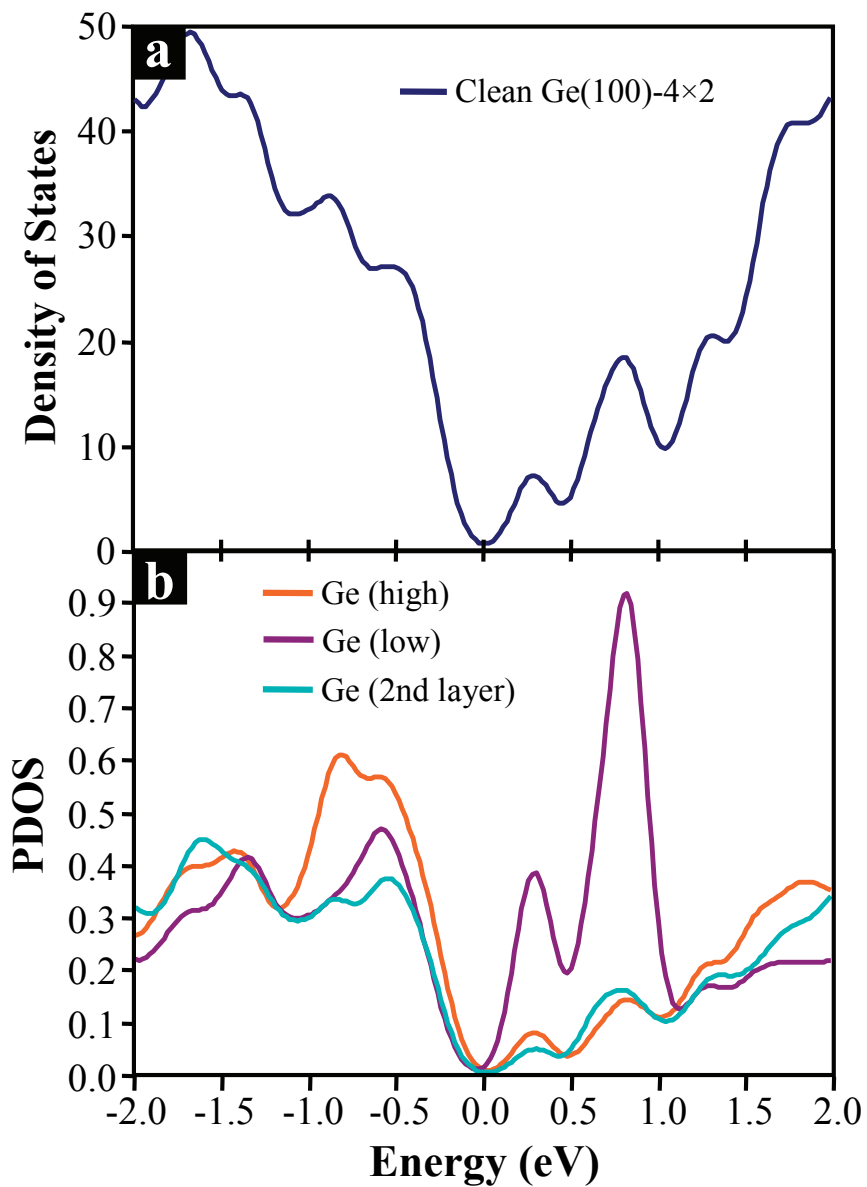
FIGURE 3.5. DFT calculated (a) density of states, DOS, and (b) projected densities of states, PDOS, for clean Ge(100)-4×2. Note the different electronic structures for the high vs. low Ge surface dimer atoms, where the sp[2]-like low atom has a large empty-state (CB) density, while the sp[3]-like high atom has a greater filled-state (VB) density.
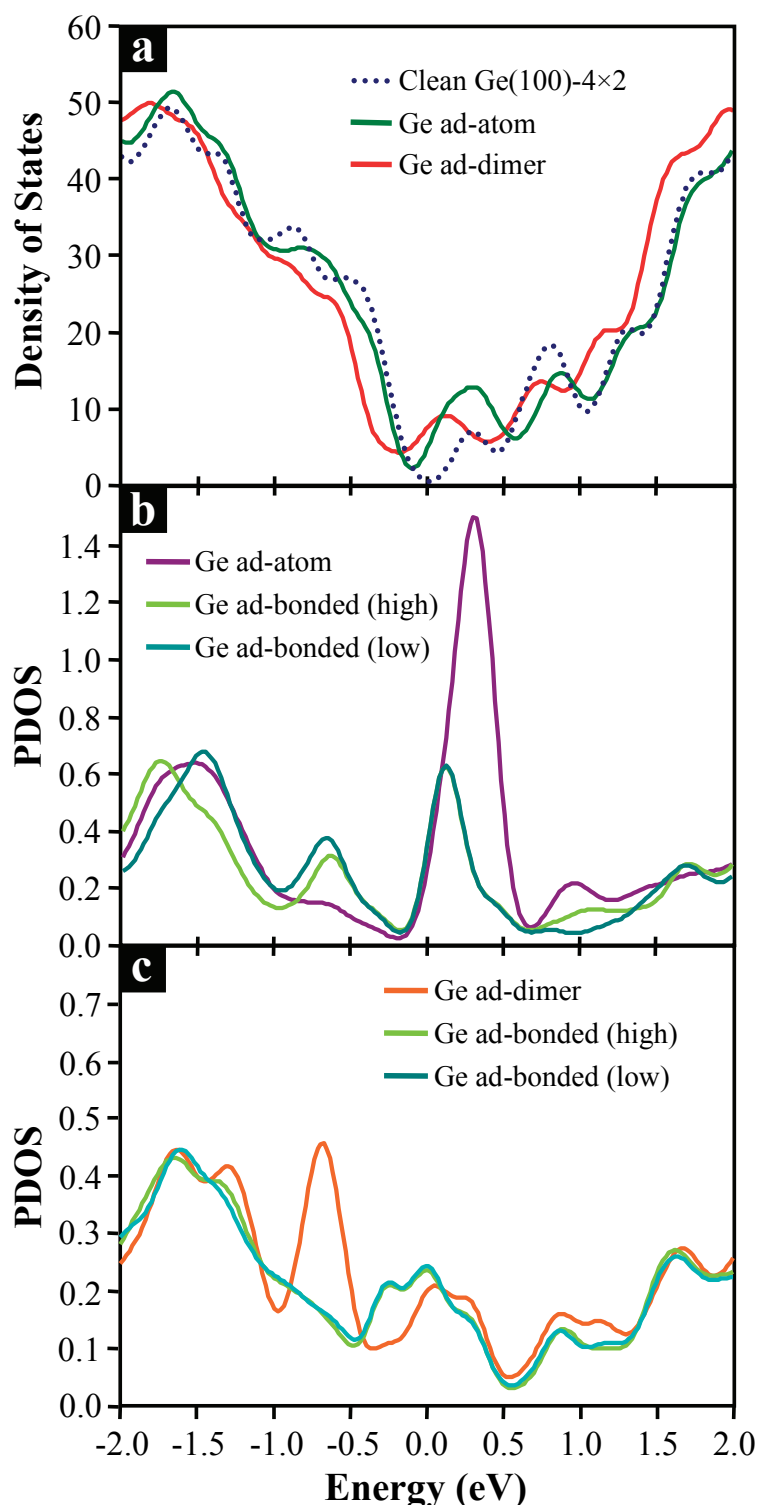
FIGURE 3.6. DFT calculated densities of states and projected densities of states for type A features. (a) Total DOS for both sites, compared with clean Ge(100) surface. (b) PDOS for Ge ad-atom and affected surface Ge atoms, and (c) PDOS for Ge ad-dimer and affected surface Ge atoms.
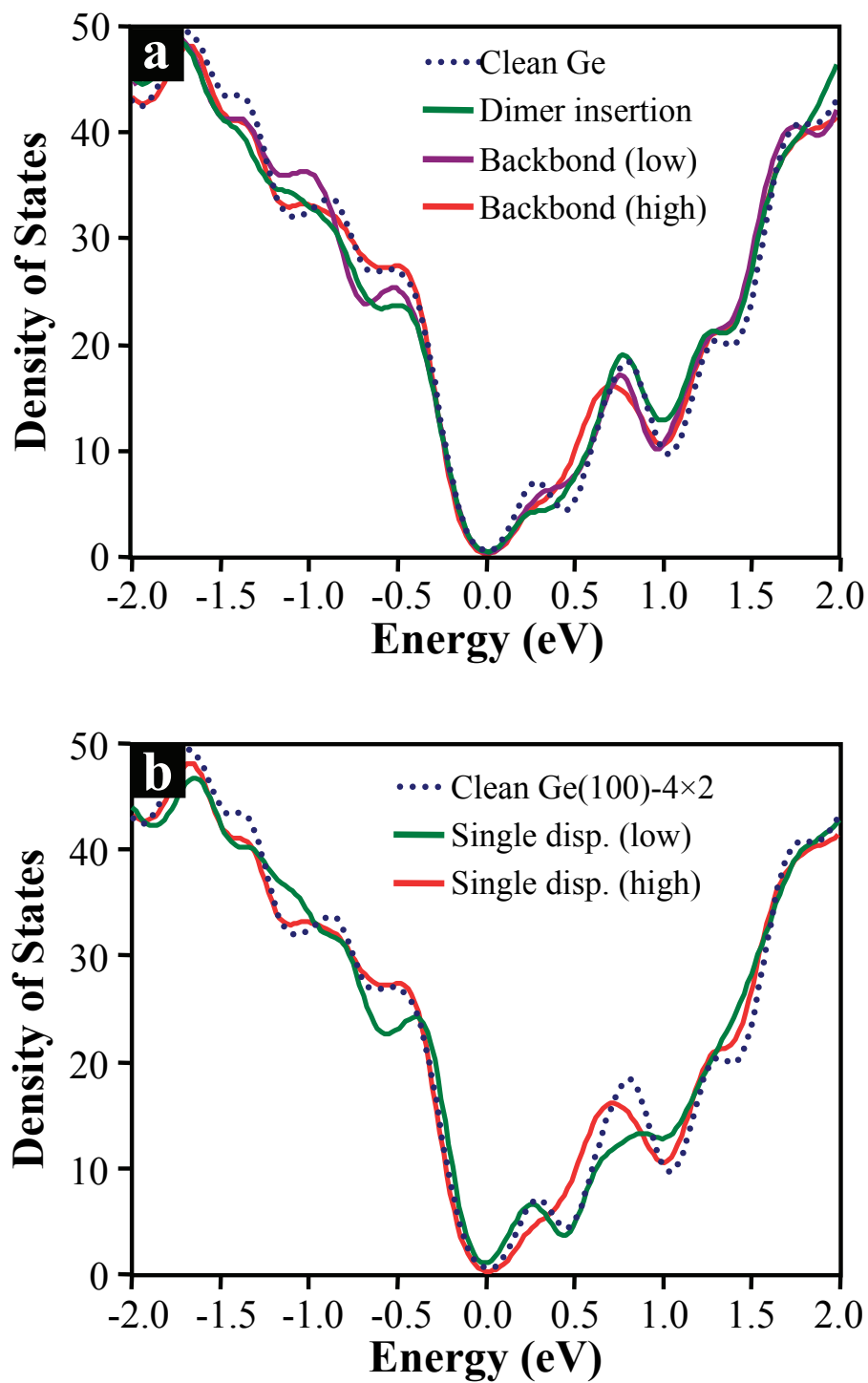
FIGURE 3.7. DFT calculated densities of states for (a) type B reaction products and (b) type C reaction products from the room-temperature oxidation of Ge(100).
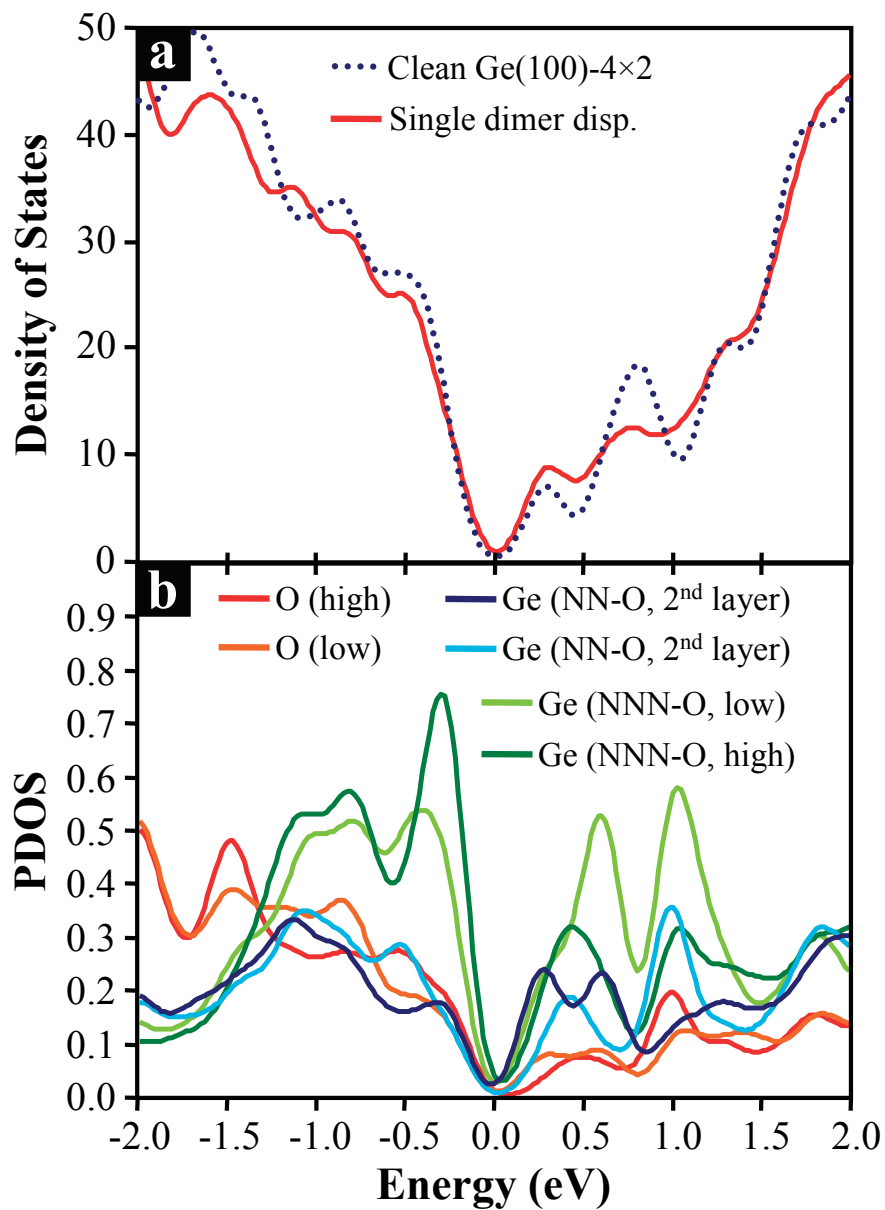
FIGURE 3.8. DFT calculated (a) density of states and (b) projected density of states for the type D reaction product from the room-temperature oxidation of Ge(100).
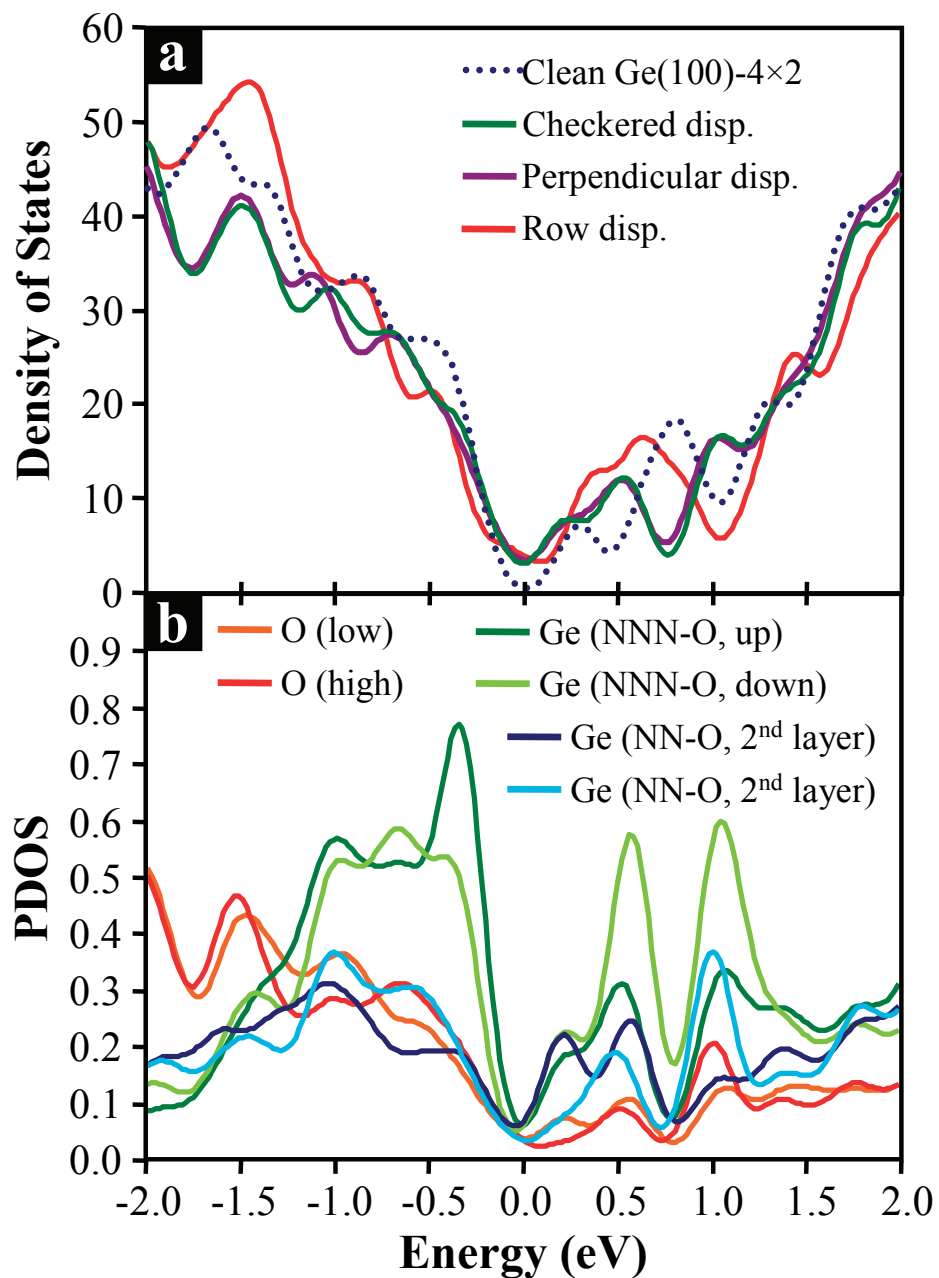
FIGURE 3.9. DFT calculated (a) densities of states for two high coverage (50%) dimer displacement geometries. (b) PDOS for the checkered dimer displacement geometry.

3.8 REFERECES

[1] R. H. Kingston, J. Appl. Phys. **27** (2), 101 (1956).

[2] P. W. Loscutoff and S. F. Bent, Annu. Rev. Phys. Chem. **57** (1), 467 (2006).

[3] K. Prabhakaran, F. Maeda, Y. Watanabe et al., Appl. Phys. Lett. **76** (16), 2244 (2000).

[4] V. Craciun, I. W. Boyd, B. Hutton et al., Appl. Phys. Lett. **75** (9), 1261 (1999).

[5] O. J. Gregory, E. E. Crisman, L. Pruitt et al., Mater. Res. Soc. Symp. Proc. **76**, 307 (1987).

[6] Y. Wang, Y. Z. Hu, and E. A. Irene, J. Vac. Sci. Technol., A **12** (4), 1309 (1994).

[7] D. B. Alford and L. G. Meiners, J. Electrochem. Soc. **134** (4), 979 (1987).

[8] S. Huiling, H. Okorn-Schmidt, K. K. Chan et al., IEEE IEDM, 441 (2002).

[9] C. M. Ransom, T. N. Jackson, and J. F. DeGelormo, IEEE Trans. Electron Devices **38** (12), 2695 (1991).

[10] R. S. Johnson, H. Niimi, and G. Lucovsky, J. Vac. Sci. Technol., A **18** (4), 1230 (2000).

[11] M. L. Lee, C. W. Leitz, Z. Cheng et al., Appl. Phys. Lett. **79** (20), 3344 (2001).

[12] R. A. McKee, F. J. Walker, and M. F. Chisholm, Science **293** (5529), 468 (2001).

[13] M. Meuris, A. Delabie, S. Van Elshocht et al., Mat. Sci. Semicond. Proc. **8** (1-3), 203 (2005).

[14] K. C. Saraswat, C. O. Chui, T. Krishnamohan et al., Microelectron. Eng. **80**, 15 (2005).

[15] T. Fukuda, Surf. Sci. **417** (2-3), L1149 (1998).

[16] T. Fukuda and T. Ogino, Surf. Sci. **357-358**, 748 (1996).

[17] T. Fukuda and T. Ogino, Phys. Rev. B **56** (20), 13190 (1997).

[18] T. Fukuda and T. Ogino, Surf. Sci. **380** (1), L469 (1997).

[19] T. Fukuda and T. Ogino, Appl. Surf. Sci. **130-132**, 165 (1998).

[20] T. Fukuda and T. Ogino, Appl. Phys. A **66** (0), S969 (1998).

[21] S. Kurokawa, H. Yamashita, J. Yoshikawa et al., Jpn. J. Appl. Phys. **38** (Part 1, No. 6B), 3845 (1999).

[22] E. J. J. Kirchner and E. J. Baerends, Surf. Sci. **311** (1-2), 126 (1994).

[23] J. M. Soon, C. W. Lim, K. P. Loh et al., Phys. Rev. B **72** (11), 115343 (2005).

[24] R. M. Feenstra, J. A. Stroscio, and A. P. Fein, Surf. Sci. **181** (1-2), 295 (1987).

[25] N. D. Lang, Phys. Rev. B **34** (8), 5947 (1986).

[26] N. Li, M. Zinke-Allmang, and H. Iwasaki, Surf. Sci. **554** (2-3), 253 (2004).

[27] A. Selloni, P. Carnevali, E. Tosatti et al., Phys. Rev. B **31** (4), 2602 (1985).

[28] J. Tersoff and D. R. Hamann, Phys. Rev. Lett. **50** (25), 1998 (1983).

[29] J. Tersoff and D. R. Hamann, Phys. Rev. B **31** (2), 805 (1985).

[30] J. A. Strosico and R. M. Feenstra, in *Scanning Tunneling Microscopy*, edited by J. A. Strosico and W. J. Kaiser (Academic Press, San Diego, 1993).

[31] G. Kresse, Thesis, Technische Universität Wien, 1993.

[32] G. Kresse and J. Furthmüller, Phys. Rev. B **54** (16), 11169 (1996).

[33] G. Kresse and J. Furthmüller, Comp. Mat. Sci. **6** (1), 15 (1996).

[34] G. Kresse and J. Hafner, Phys. Rev. B **47** (1), 558 (1993).

[35] P. E. Blöchl, Phys. Rev. B **50** (24), 17953 (1994).

[36] G. Kresse and D. Joubert, Phys. Rev. B **59** (3), 1758 (1999).

[37] J. Paier, R. Hirschl, M. Marsman et al., J. Chem. Phys. **122** (23), 234102 (2005).

[38] D. L. Winn, M. J. Hale, T. J. Grassman et al., J. Chem. Phys. **126** (8), 084703 (2007).

[39] W. E. Spicer, P. W. Chye, P. R. Skeath et al., J. Vac. Sci. Technol. **16** (5), 1422 (1979).

[40] W. E. Spicer, Z. Liliental-Weber, E. Weber et al., J. Vac. Sci. Technol., B **6** (4), 1245 (1988).

[41] J. P. Perdew and M. Levy, Phys. Rev. Lett. **51** (20), 1884 (1983).

[42] L. J. Sham and M. Schlüter, Phys. Rev. Lett. **51** (20), 1888 (1983).

[43]   O. Gurlu, H. J. W. Zandvliet, and B. Poelsema, Phys. Rev. Lett. **93** (6), 066101 (2004).

CHAPTER FOUR

Passivation of the Ge(100) Surface Using Molecular SiO

4.1 ABSTRACT

Molecular SiO deposited onto the Ge(100)-2×1/4×2 surface was studied using scanning tunneling microscopy/spectroscopy (STM/STS), and density functional theory (DFT) modeling. STM images of the SiO-dosed Ge(100) surface indicate that the major adsorption geometry for the system is a pyramid-like $(SiO)_3$ molecular trimer, bonding to the surface via the Si atoms, bridging the trough between Ge dimer rows. Annealing studies and DFT modeling reveal that the adsorbate-type $(SiO)_3$ pyramid geometry, in which the two of the Si atoms bond to two trough-edge Ge atoms, is metastable ($<\Delta H_{ads}>$ = -1.56 eV), while the displacement-type geometry, in which two of the Si atoms displace two trough-edge Ge atoms, is the most stable configuration ($<\Delta H_{ads}$ = -1.96 eV). STS dI/dV spectra of the associated surface density of states show that SiO adsorption onto both n- and p-type Ge(100) surfaces yields an unpinned Fermi level, indicating a low defect density interface and the potential for use of SiO films for Ge passivation during the deposition of MOSFET gate oxides.

4.2 INTRODUCTION

Due to the approach of the fundamental limits of classical silicon CMOS (complementary metal-oxide-semiconductor) device scaling, alternative channel materials for high-speed metal-oxide-semiconductor field-effect transistors (MOSFET) are being thoroughly investigated. One such alternative material is germanium, which possesses greater low-field intrinsic carrier mobilities may provide for a significant increase in saturation current over state-of-the-art MOSFET devices. However, in contrast to Si, Ge does not have a suitably stable electrically-passivating native oxide. The Ge native oxide, GeO_2, is both water-soluble and thermally unstable at elevated temperatures; GeO_2 decomposes and desorbs as GeO above 400ºC.[1-3] Therefore, an alternative dielectric and/or electrical passivation method is needed.

Numerous experiments have attempted the fabrication of Ge-based MOSFETs (as well as MOS capacitors) using a great diversity of insulators, including GeO_2,[4-6] Ge_3N_4,[7] GeO_xN_y,[5,8,9] SiO_2 (with and without a Si interlayer/cap),[10,11] and high-k metal-oxides ($BaStTiO_3$, ZrO_2, HfO_2).[12-14] The success (or failure) of these different dielectric materials has been found to depend on the chemical passivation of the Ge at the semiconductor-oxide interface. In general, devices that were fabricated without sufficient passivation of the Ge(100) surface contained interfacial GeO_2 and were consistently found to yield poor C-V (capacitance-voltage) characteristics: large frequency dispersion in accumulation, capacitance peaks within the band gap, gate leakage, and/or flat-band shifts, all of which are associated with interfacial or oxide traps and fixed charge. However, those devices that were fabricated with sufficient passivation, thereby

preventing the formation of interfacial GeO_2, were found to exhibit superior C-V characteristics. It has been shown that the oxidation of Ge(100) by O_2, and the formation of germanium suboxides at the surface, causes Fermi level pinning,[15] so avoiding the formation of the Ge native oxide is paramount.

Si-O and Si-Ge bonding is known to be unproblematic. SiO is a non-pinning transitional species at the Si/SiO_2 interface,[16-18] one of the lowest defect and electrically passive interfaces known, and epitaxially-grown Si (with and without subsequent oxidation) capping layers have been utilized to produce reasonably successful high-κ/Ge-based MOS devices.[10,11,19] High-quality solid SiO source MBE-grown epitaxial layers have been reported on the GaAs(100) surface, but no such attempts appear to have been made on the Ge(100) surface. However, because SiO also evaporates congruently and is therefore very easy to deposit cleanly on the Ge surface, it is possible SiO can passivate Ge without forming a high density of Ge-O bonds.

We have performed an atomic-level study of the structural and electronic properties of SiO deposited on the Ge(100) surface utilizing scanning tunneling microscopy (STM), scanning tunneling spectroscopy (STS), and density functional theory (DFT) modeling to provide a fundamental understanding of the atomic structure of the surface binding sites (STM, DFT) and the resultant electronic structures (STS, DFT). For definitive determination of the effect of SiO deposition and on the electronic structure, we measured the STS spectra on the clean and SiO-deposited surfaces of both *n*-type and *p*-type substrates, and modeled the observed reaction sites with DFT to help better characterize the physical and electronic structures.

4.3 METHODS

A. Experimental Setup

All experiments were performed under ultra-high vacuum (UHV) conditions with a base chamber pressure of $2 - 3 \times 10^{-10}$ Torr. The UHV chamber is equipped with a water-cooled manipulator and sample holder, a differentially-pumped ion gun (VG Microtech EX05), a custom-built differentially-pumped deposition source chamber (allowing for the low-background pressure deposition of various oxides from high-temperature effusion cells), a room-temperature scanning tunneling microscope (Park Scientific Autoprobe VP1), and a standard set of analytical instruments: Auger electron spectrometer (AES), low-energy electron defractometer (LEED), and quadrupole mass spectrometer (QMS).

Experiments were performed on 18 mm × 6 mm samples cut from *n*-type (Sb-doped, $1.88 \times 10^{17} - 1.54 \times 10^{18}$ cm^{-3}, $0.020 - 0.005$ Ω-cm) and *p*-type (Ga-doped, $1.58 \times 10^{17} - 1.12 \times 10^{18}$ cm^{-3}, $0.040 - 0.010$ Ω-cm) 100 mm Ge(100) wafers purchased from Wafer World (epi-grade, ±1° orientation tolerance). The samples were lightly cleaned of oils and particles using a lint-free cloth wetted with methanol or isopropanol prior to insertion into the vacuum chamber. The Ge(100) samples were prepared by successive sputter/anneal cycles: sputtering at normal incidence with $800 - 1000$ V Ar^{+} ions at a sample temperature of 500ºC, followed by resistive annealing at 700ºC for 20 minutes, with a 1ºC/min ramp down to room temperature. Typically, about three or four cycles were required to reach peak surface cleanliness and order. This treatment produced large, well-ordered, defect-free terraces. Surface cleanliness and order was

checked with Auger electron spectroscopy, low-energy electron diffraction, and scanning tunneling microscopy (STM).

Following a successful STM-based check for surface cleanliness and order, the sample was returned to the main chamber for SiO dosing. Solid SiO (sintered powder, Alfa-Aesar) was heated to 925ºC in a high-temperature effusion cell in the differentially-pumped deposition source chamber. Opening the source chamber to the main chamber caused a background pressure rise of no more than 2×10^{-10} Torr. SiO was deposited onto room-temperature Ge(100) samples for $1 - 10$ seconds (depending on coverage desired). The SiO-dosed samples were then resistively annealed to either 200ºC or 300ºC, with a 1ºC/min temperature ramp down to room-temperature. The samples were then returned to the STM for further analysis.

 Filled-state constant-current STM images were generally taken at -1.8 V – -2.0 V sample bias and $0.2 - 0.5$ nA tunneling current with electrochemically-etched tungsten tips. Scanning tunneling spectroscopy (STS) was performed using the variable tip-sample separation method developed by Feenstra *et al.*, yielding a dimensionless spectrum that is an approximation to the surface density of states[20-26] (which were subsequently normalized to unity). A 1.4 kHz, 0.2 V sine-wave was used for the bias modulation, and the signal was extracted with a digital lock-in amplifier (Stanford Research Systems SR850).

B. Computational Details

All density functional theory (DFT) calculations presented in this paper were performed using the Vienna Ab-Initio Simulation Package (VASP)[27-30] in the generalized

gradient approximation (PBE exchange-correlation functional), with projector augmented wave (PAW) potentials[31,32] (as supplied by the VASP group), a 4×4×1 Monkhorst-Pack k-point mesh generation scheme (for a total of 4 irreducible k-points), and plane-wave basis cut-off of 450 eV. All parameters (i.e. k-points, cut-off energy, vacuum space, slab thickness, etc.) were chosen such that they were each individually converged to within 1 meV/atom for the system of study. The absolute error of this type of calculation is estimated to be up to 0.37 eV,[33] but it is difficult to quantify the error for the SiO/Ge(100) system presented in this report. Regardless of absolute numerical accuracy, the qualitative results from these calculations should be quite reasonable because comparisons are being made merely between different bonding geometries that have all been calculated under identical conditions and with similar types of bonds. Therefore, the calculations in this paper should have good relative accuracy, with an estimated relative error of ±0.1 eV.[34] We also note that all of the experiments reported in this manuscript was performed at 300 K so differences in energies less than 0.1 eV are probably immaterial for comparison between experiment and theory anyway.

The system studied consisted of an Ge(100) slab supercell with a 4×2 surface dimer reconstruction, as this is the lowest energy configuration (compared to the 2×1 flat dimer and 1×1 unreconstructed geometries). The germanium slab was 8 atomic layers thick, with each layer being 2×4 atoms in area, for a total of 64 Ge atoms per unit cell (for the clean, Ge surface/substrate calculations). The bottom of the slab was unreconstructed and terminated with 16 hydrogen atoms (two H atoms per Ge). The clean Ge supercell contained 12 atomic layers of vacuum space in the z-direction. The bottom three Ge layers were constrained to the minimum-energy bulk DFT geometry,

which was found through a series of bulk Ge calculations to have a lattice parameter of 5.795 Å (2.6% larger than the experimental result of 5.646 Å due to the well-known GGA overestimation of lattice parameters). The terminating H atoms were initially allowed to relax and were kept fixed at these optimized positions for all subsequent calculations. All other atoms (upper substrate, adsorbate, gas-phase) were allowed to structurally relax with respect to interatomic forces to a tolerance of 0.01 eV/Å.

DFT-based STM simulations were produced using the Tersoff-Hamann approach, wherein the charge density is calculated for the energy range of interest – in this case 0 eV to -2 eV to match the STM conditions – and an isodensity plot of the computational slab surface is produced as an approximation to a constant-current style STM image. All of the STM simulations presented in this report were generated with the same contrast (i.e. color minima and maxima) as the clean Ge simulations for the sake of direct comparison.

4.4 RESULTS AND DISCUSSION

A. SiO/Ge(100) Bonding Geometry Characterization

The bonding geometries of adsorbates on surfaces, in addition to the intrinsic properties of the materials themselves, play a definitive role in the determination of the electronic properties of the resultant interfaces. This is an especially important issue in the consideration of passivation of semiconductor surfaces, where knowledge of the chemical nature of the interface can yield a large amount of insight. In this work, the physical adsorbate structures resulting from the exposure of Ge(100) to an effusive beam

of SiO have been directly investigated using scanning tunneling microscopy (STM) of the dosed surface. To complement the experimental STM work, many possible adsorbate geometries were investigated with density functional theory (DFT) modeling, including both configurations indicated by the STM imaging and structures considered possible through simple chemical reasoning. Adsorption energies calculated from the DFT models are used to help examine which of the possible geometries are thermodynamically reasonable and stable at the experimental conditions, and which would be unlikely or impossible. The combination of STM imaging, DFT adsorption energy calculations, and DFT-based STM simulations allows for the unambiguous assignment of SiO adsorption sites and resultant bonding geometries.

Figure 4.1a is a typical filled-state STM image of the clean, prepared Ge(100)-2×1/4×2 surface. This surface exhibits what is commonly referred to as a 2×1 dimer row reconstruction, which is a dynamic 4×2 buckled dimer reconstruction with a low activation energy to intra-dimer rocking (giving it an overall 2×1 periodicity and making the dimer rows appear flat due to time-averaging during the course of the scan). In addition to the flat-looking 2×1 rows, one can also see other rows, as well as small domains, where the 4×2 buckled dimer configuration has been frozen due to stabilization by step-edge and/or lattice defects; this effect is also observed on Si(100) at cryogenic temperatures. Also in Fig. 4.1a are DFT-based STM simulations of the 2×1 and 4×2 reconstructions, overlayed on 2×1 and 4×2 regions of the surface, respectively.

Table 4.1b displays ball-and-stick models of the top three layers for the two different dimer reconstruction geometries. We note that the 4×2 buckled dimer structure is significant because it is accompanied by electron transfer from the "low" dimer atoms

(sp^2-like) to the "high" dimer atoms (sp^3-like), which changes the reactivity of the two respective dangling bonds and changes the electronic structure from metallic to semiconducting.

Figure 4.2a is a typical filled-state STM image of the Ge(100)-2×1/4×2 surface after being dosed with ~10% ML molecular SiO and annealed at 200ºC for 5 minutes. The most noticeable features on the surface are the large, bright, round sites bridging the troughs (indicated by the hexagon), often lining up perpendicular to the row direction. Because such sites do not appear on either the clean or the oxidized Ge(100) surface, we conclude that these large, bright, round sites are SiO-based adsorbates. A few other sites are also visible in the STM images, as indicated in Fig. 4.2a: (ovals) Ge and/or Si ad-atoms and ad-dimers, as evidenced by the tell-tale 4×2 dimer zigzag, (rectangles) single SiO or O adsorbates residing on the Ge rows, and (diamonds) dark O-induced Ge displacement sites, presumably a result of either a slightly "dirty" SiO dosing beam or some amount of SiO decomposition on the surface. Line-scans of the STM images of the various observed sites were used to help in their identification, and examples are given in Fig. 4.2b.

The line-scan over two of the large, bright, round SiO-based sites shows that these sites each image with a height of 2.0 Å above the Ge dimer surface plane and about 8 Å wide. The size of these sites, therefore, indicates that they are not merely single SiO molecular adsorbates. It is also quite unlikely that a single SiO molecule could span the entire trough while these bright sites clearly do. Chemical reasoning and DFT modeling lead to the conclusion that these SiO adsorbates reside on the surface as pyramid-like trough-bridging SiO trimers, or (SiO)$_3$ molecular units. The alignment of these sites,

even at low SiO coverages, indicates that there is either a thermodynamic benefit (i.e.

greater overall enthalpy of adsorption) or a reduction of kinetic barriers for adsorption of

new incoming $(SiO)_3$ trimers induced by previous adsorbates.

Table 4.1 displays DFT modeling results for the various $(SiO)_3$ adsorbate

configurations considered for the identification of the large, bright, round SiO sites seen

on the SiO-dosed Ge(100)-4×2 surface, including ball-and-stick diagrams, DFT-based

STM simulations, and calculated enthalpies of adsorption. Geometries consisting of SiO

monomers and $(SiO)_2$ dimers were also considered, but all were found to have enthalpies

of adsorption smaller than -1.06 eV/SiO, which is significantly lower than even the least

stable $(SiO)_3$ pyramid geometry (ΔH_{ads} = -1.37 eV/SiO). Therefore, the monomer and

dimer sites were dismissed from further consideration, and are expected to be, at best,

short-lived metastable sites.

There were two distinct types of trough-bridging $(SiO)_3$ trimer pyramid sites

considered in this work: adsorbate-type, where each bottom Si atom bonds directly to one

Ge atom on opposite sides of the trough, and displacement-type, where each bottom Si

atom displaces one Ge atom on opposite sides of the trough. The individual sites were

performed at a surface coverage of 25% such that pyramids within the computational unit

cell were not directly adjacent to each other in either lateral direction. The displacement-

type $(SiO)_3$ pyramid sites were found to be the most energetically favorable, with

enthalpies of adsorption of -1.92 and -1.99 eV/SiO for the high and low geometries,

respectively, which are considered degenerate within the estimated accuracy of the

calculations. The adsorbate-type $(SiO)_3$ pyramid sites were found to have enthalpies of

adsorption of -1.37 and -1.67 eV/SiO for the high and low geometries, respectively. Note

the slight twist of the high adsorbate-type geometry, putting the bottom Si atoms closer to their proper tetrahedral sp^3 configuration. The low geometry is slightly more stretched out due to the longer distance between the Ge atoms on opposite sides of the trough, and is therefore unable to twist in the same manner; twisting was found to increase reduce the magnitude of the enthalpy of adsorption for the low adsorbate site, opposite to the behavior seen for the high adsorbate case.

Higher $(SiO)_3$ pyramid site coverages were also considered, namely perpendicularly-aligned (50%) and full coverage (100%) configurations for both the adsorbate and displacement geometries. The perpendicular alignment of the adsorbate-type $(SiO)_3$ pyramid sites was found to yield a slightly higher enthalpy of adsorption, -1.60 eV/SiO, compared to the average of the two single singles sites, -1.52 eV/SiO, due to the ability of all the pyramids to slightly twist, similar to the single high $(SiO)_3$ adsorbate case. Full coverage of the adsorbate-type sites gave an enthalpy of adsorption equal to the perpendicularly-aligned geometry, -1.61 eV/SiO. Both perpendicular alignment and full coverage of the displacement-type $(SiO)_3$ pyramid sites was found to yield an enthalpy of adsorption equal to the average of the two single sites, -1.96 eV/SiO. The lack of any significant difference in energy between the perpendicularly-aligned and the single site enthalpies of adsorption for either $(SiO)_3$ geometry type leads to the conclusion that the experimentally-observed alignment is most likely a kinetic effect (i.e. reduced barrier to further adsorption) rather than thermodynamic.

The difference in enthalpies of adsorption for the adsorbate-type and displacement-type geometries, -0.44 eV/SiO in favor of the displacement-type, is definitely large enough to be considered experimentally significant. It may be reasonable

to expect some percentage of adsorbate-type geometries to exist on the surface as metastable sites, but given sufficient annealing they should all be converted to displacement-type sites. Most likely this reaction is a source of a substantial fraction of the displaced Ge atoms and dimers observed on the 200ºC post-deposition annealed SiO/Ge(100) surface (see Fig. 4.2a). The DFT simulations for the displacement-type geometries also appear to be most consistent with the sites seen in the STM images due to their slightly elongated appearance and more appropriate image contrast level. Additionally, we believe that the low displacement-type $(SiO)_3$ pyramid STM simulation appears to be most consistent with the isolated sites observed in the STM images.

Figure 4.3 contains filled-state STM images of higher coverages of SiO on the Ge(100)-2×1/4×2 surface. Fig. 4.3a is about 50% ML coverage, while 3b is roughly 1 ML; both samples were post-deposition annealed to 200ºC. As the coverage increases and the density of $(SiO)_3$ pyramid sites also increases, the contrast ratio decreases and the pyramid sites appear smaller, but they are still the same size. Fig. 4.3b shows that at full coverage SiO forms a relatively uniform film, as the two step edges in the upper right-hand corner can easily be distinguished. At high coverage, the ratio of pyramids to dark sites increases but the ratio of pyramids to dimmer bright sites remains constant. This is consistent with displacement pyramid sites being favored at high coverage since the dimmer bright sites are likely to be displaced Ge atoms from the formation reaction.

To distinguish between adsorption and displacement pyramid sites, the samples were annealed to 300ºC. On annealing the SiO-dosed sample up to 300ºC, we find what appears to be a greater ratio of Ge ad-atoms and ad-dimers to $(SiO)_3$ pyramids than seen on the 200ºC annealed surface, as shown in Figure 4.4. For example, counting up the ad-

dimers (encircled in Fig. 4.4) and $(SiO)_3$ pyramid sites yields a ratio of about 75%, almost two Ge atoms for every $(SiO)_3$ pyramid site located within the same image area; some of the other, less bright sites could also be Ge ad-atoms, and because of their mobility at the annealing temperature it is reasonable to expect that a fair number of them may have been incorporated into the proximal step edges. The lack of O-induced dark sites in Fig. 4.4 suggests that very few of the Ge ad-atoms resulted from displacement by oxygen (due to decomposition of SiO or even the presence of O_2 in the deposition beam). The oxygen sites should be easy to image because at these annealing temperatures oxidation reaction dark sites are well-known to coalesce into dark rows.[15,35-38] This is consistent with the Ge ad-atoms seen on this surface primarily being created by the formation of displacement-type $(SiO)_3$ pyramids.

While it is a bit more difficult to quantify the number of Ge ad-atoms and ad-dimers on the 200ºC annealed sample because of the reduced surface order, it does appear to possess considerably fewer Ge ad-species. The apparent evolution of a greater number of Ge ad-species indicates that the displacement-type $(SiO)_3$ pyramids are indeed the thermodynamically preferred geometry, as predicted by the DFT modeling results, and that annealing up to 300ºC vs. 200ºC allows for the surmounting of any kinetic barriers to the displacement reaction.

B. SiO/Ge(100) Electronic Structure Characterization

1. Experimental Electronic Structures

Scanning tunneling spectroscopy (STS) measurements yield (dI/dV)/(I/V) curves

that give an approximation to the local surface density of states.[20-26] Therefore, these spectra possess the same features as a standard density of states (DOS) plot, namely a valence band, conduction band, band gap, and Fermi level. The Fermi level is found at the zero volt position, while a negative sample bias probes "filled" electronic states (valence band, VB) and a positive sample bias probes "empty" electronic states (conduction band, CB). In between the VB and CB edges is the band gap (i.e. where the DOS, and thus the STS signal, is equal to zero). Therefore, in STS spectra, a *p*-type sample has a Fermi level position near the VB and an *n*-type sample has a Fermi level position near the CB. It is this property that will be employed in this work, since a misplaced Fermi level is consistent with electronic pinning due to a high density of surface states within the band gap.[39,40] STS experiments were performed on both clean and SiO-dosed *p*- and *n*-type Ge(100)-2×1/4×2 surfaces in order to discover whether SiO will work as a passivant or cause Fermi level pinning.

Presented in Figure 4.5 are STS results for the clean and 200ºC post-deposition annealed SiO-dosed (~20% ML) samples, for both *p*- (Fig. 4.5a) and *n*-type (Fig. 4.5b) Ge(100) substrates. Clearly, deposition of SiO onto the Ge(100) surface does not pin the Fermi level for either *p*- or *n*-type samples, as the Fermi level resides in its proper location for each, near the VB for *p*-type Ge(100) and near the CB for *n*-type Ge(100). Such results indicate that SiO is at the very least a non-pinning species on the Ge(100)-2×1/4×2 surface.

These results are in contrast to what is seen for the GaAs(100)-*β*2(2×4) surface, where SiO coverages of ≤ 10% are found to induce mid-gap Fermi level pinning.[34] In this case, the pinning was attributed to one major cause: the generation of partially-filled

dangling bonds. These dangling bonds were located on both undimerized As atoms and the bottom Si atoms in $(SiO)_3$ pyramids. The standard electron counting model yields a GaAs(100)-$\beta2$(2×4) surface with either completely filled (As) or completely empty (Ga) dangling bonds. Therefore, the generation of partially-filled dangling bonds is likely to induce states into the band gap (as the gap is essentially defined as the energy space between filled states and empty states).

The Ge(100)-2×1/4×2 surface, however, is full of partially-filled dangling bonds (one per atom, to be exact). It is the 4×2 buckling of the surface dimers, with the associated intradimer electron transfer, that prevents their dangling bonds from being exactly half full (as they would be for the 2×1 flat dimer configuration). Gurlu *et al.* showed that even the transitory existence of the 2×1 flat dimers on the Ge(100) surface as the 4×2 dimers rock side to side leads to the induction of small metallic states within the band gap, near the Fermi level.[41] Therefore, it seems that as long as dangling bonds on the surface are not exactly half full, the resulting electronic states will be shifted away from the Fermi level.

2. Theoretical Electronic Structures

Densities of states were calculated from the previously-discussed $(SiO)_3$ trough-bridging pyramid adsorbate system DFT simulations in order to provide further insight to the electronic structures of the various types of adsorbate geometries, and how those electronic structures relate to the experimental results. It must be noted, however, that there are well-known problems with standard LDA- and GGA-based DFT with respect to the electronic structures of semiconducting and insulating materials, namely a general

underestimation of the band gap by 30 – 100%, due to the approximation of the exchange potential.[42,43] Unfortunately, this problem is at its worst for small band gap semiconductors, such as germanium. In fact, standard DFT predicts a slight overlap of the Ge VB maximum and CB minimum, producing a semi-metallic electronic structure (see Figure 4.6a).

However, because there is still a significant minimum in the DOS at the Fermi level, it is possible to extract useful information from standard DFT calculations of Ge(100). Specifically, we compare the calculated DOS of the clean Ge(100)-4×2 slab with the DOS of the various Ge(100) slabs with SiO adsorbates on them. We note that we can check the validity of this approach because we have the experimental STS data for comparison. Because we are particularly interested in the induction of electronic states within the band gap, a potential cause of Fermi level pinning, special attention will be paid to the near-Fermi level region of the calculated densities of states. There are two general changes to the DOS induced by the addition of SiO adsorbates to the Ge(100) surface: (a) the DOS at the near-E_F region decreases (or exhibits no change) after the addition of the oxygen induced sites, or (b) the DOS at the near-E_F region increases after the addition of oxygen induced sites. If the DOS decreases or shows no change, it is reasonable to conclude that the reaction site is not a potential source of Fermi level pinning, while if the DOS increases it is reasonable to conclude that pinning is possible because of the induction of band gap or band edge states that are consistent with Fermi level pinning.

Figure 4.7 presents the calculated densities of states for the two different isolated adsorbate-type $(SiO)_3$ pyramid sites considered – trough-bridging via low Ge atoms and

trough-bridging via high Ge atoms – at a homogeneous 25% surface coverage. The low adsorbate site considerable DOS at the clean Ge(100) Fermi level, with a shifted minimum, while the high adsorbate site displays a very clean electronic structures (i.e. essentially equal to the clean Ge DOS in the near-E_F region).

PDOS analysis for the low adsorbate $(SiO)_3$ pyramid site (see Figure 4.8) indicates that the majority of the state density in the near-E_F region belongs to the Si atoms at the bottom of the pyramid, with the states being slightly delocalized throughout the local covalent bonding network. Most likely this is a result of the sp^3-like Si atom being forced into a flat, sp^2-like geometry. That is, the electron density belonging to the dangling bond that would be present in the sp^3 geometry is being forced into the surrounding bonds, perhaps creating some strained π-bonding between the two bottom Si atoms and to the Ge atoms to which they are bonded. The high adsorbate geometry does not suffer this same fate because of the previously-discussed twist in the pyramid structure, allowing the bottom Si atoms to reside in sp^3-like geometries. The upper Si atom is unaffected in either case because it is in a proper sp^2 situation, making a double bond to the upper O atom, and two single bonds to the two lower O atoms.

The calculated densities of states for 25% surface coverage of the two displacement-type $(SiO)_3$ pyramid sites, shown in Figure 4.9, appear to be problematic, with large induced Fermi level density in both cases. PDOS analysis of both cases, trough-bridging via low Ge displacement and trough-bridging via high Ge displacement (see Figures 3.10 and 3.11, respectively), indicates that the vast majority of near-E_F state density belongs to the Ge dimer atoms to which the displacing Si atoms are bonded. That is, for the low displacement site, the remaining high Ge contains the large PDOS, while

for the high displacement site, the remaining low Ge contains the large PDOS. This behavior appears to stem from the fact that in both cases the resulting bonding geometry puts the remaining Ge dimer atom in a position closer to that in the flat 2×1 dimer, in which the atoms possess half-filled dangling bonds, whereas the Si atoms themselves have satisfied all of their dangling bonds. The Ge geometry change is also most likely accompanied by a small charge withdrawal by the Si atoms as a secondary effect of the larger charge withdrawal by the O atoms, thereby helping to further decrease the filling of the Ge dangling bonds and shift the Ge electronic states into the Fermi level region.

Of course, the displacement of Ge atoms onto the surface does indeed generate new Ge dangling bonds, two per Ge ad-atom, and these dangling bonds should be half-filled and would most likely induce states within the band gap. However, because of the high surface mobility of these ad-atoms at the very same annealing temperatures that allow the displacement reaction to proceed, the vast majority of the Ge ad-atoms appear to either find their way to step edges or into regrowth islands, where they are incorporated into dimers exhibiting 4×2 buckling (see Fig. 4.4), thereby shifting their induced electronic states out of the band gap.

The 25% surface coverage configurations, however, do not necessarily match actual experimental conditions. That is, we see in the STM images that the $(SiO)_3$ pyramids tend to line up, usually in the direction perpendicular to the rows, sharing the Ge dimers to which they are adsorbed (or displacing). In this case, the sites are no longer isolated, and one should expect differing electronic structures from such geometries. Figure 4.12a presents calculated densities of states for 50% surface coverage configurations in which the pyramid sites are aligned perpendicular to the Ge dimer rows,

similar to what is observed experimentally. Here, the adsorbate sites share the Ge dimers to which they are bonded, and the displacement sites end up displacing the Ge dimers altogether, resulting in the formation of Si dimers.

The perpendicularly-aligned adsorbate-type geometry shows a clean near-E_F DOS, just like the single high adsorbate case, because all the pyramids are now in the twisted configuration. The Ge dangling bond problem of the isolated displacement-type geometry has also been solved due to the removal of the dangling bonds (on half the surface) altogether. Therefore, not only is there some kinetic drive toward the alignment of the $(SiO)_3$ sites on the surface, but such alignment exhibits considerable improvement of any problematic near-E_F electronic states. Even if some of the single pyramid site geometries truly do induce near-E_F state density as the DFT result indicate, the fact that at least half of the $(SiO)_3$ pyramids on the surface are lined up with at least one other $(SiO)_3$ pyramid prevents much of the problematic density from ever even arising, apparently leaving the density of negative sites below some threshold for Fermi level pinning.

At full coverage, shown in Fig. 4.12b, we see additional improvement in both adsorbate and displacement $(SiO)_3$ pyramid geometries, especially in the displacement-type case. The reason for the large reduction in near-E_F DOS for the displacement configuration is straightforward: all partially-filled dangling bonds have been removed from the surface, and the resulting perturbation of the electronic structure is enough to open a semiconducting band gap. The reason for the small reduction in near-E_F DOS for the adsorbate-type full coverage geometry is probably a matter of removal of all of the Ge dangling bonds, replacing them with the seemingly less problem-prone Si dangling bonds.

4.5 CONCLUSIONS

We have performed an atomic-level study of the structural and electronic properties of SiO deposited on the Ge(100) surface utilizing scanning tunneling microscopy (STM), scanning tunneling spectroscopy (STS), and density functional theory (DFT) modeling to provide a fundamental understanding of the atomic structure of the surface binding sites (STM, DFT) and the resultant electronic structures (STS, DFT). Both experimental and theoretical work indicate that the major SiO adsorption site observed on the post-annealed surface is that of $(SiO)_3$ trimer pyramids. Adsorbate-type pyramids were computationally found to be metastable in comparison to displacement-type pyramids, a fact reinforced by experimental annealing studies of the SiO-dosed Ge(100) surface and DFT-based STM simulations. Additionally, the calculated electronic structures for the perpendicularly-aligned and full coverage displacement-type $(SiO)_3$ pyramid geometries are consistent with STS data showing the SiO/Ge(100) interface to be unpinned.

4.6 ACKNOWLEDGEMENTS

Chapter 4, in part or in full, is in preparation for submission for publication in the Journal of Chemical Physics. The dissertation author is the primary investigator and author of this paper:

T. J. Grassman, A. C. Kummel, "Passivation of the Ge(100) surface using molecular SiO." *In preparation for submission to the Journal of Chemical Physics.*
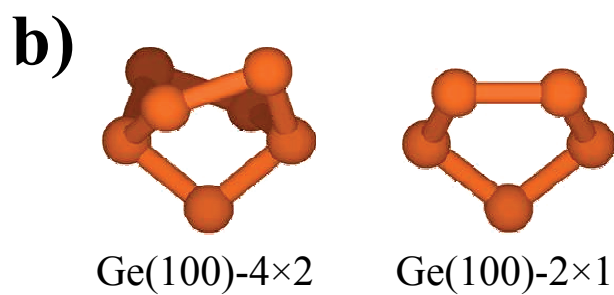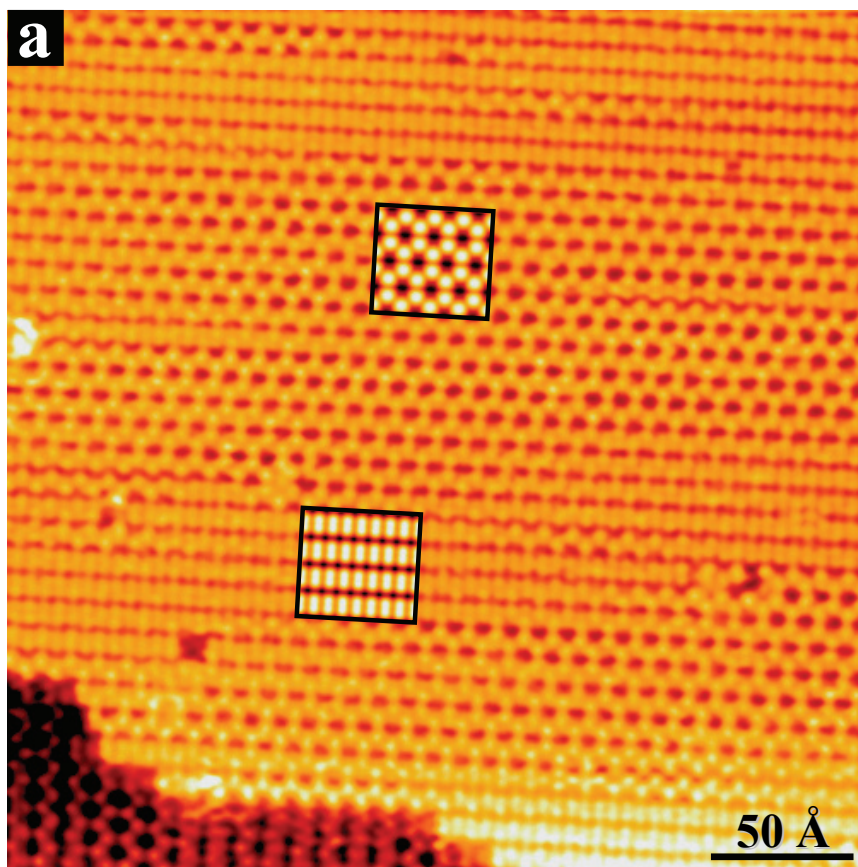
FIGURE 4.1. (a) Filled-state STM image (V_s = -2.0, I_t = 0.2 nA) of the Ge(100)-2×1/4×2 surface with inlayed DFT-based STM simulations of the 4×2 (upper) and 2×1 (lower) regions. (b) Ball-and-stick diagrams of the 4×2 and 2×1 dimer reconstructions
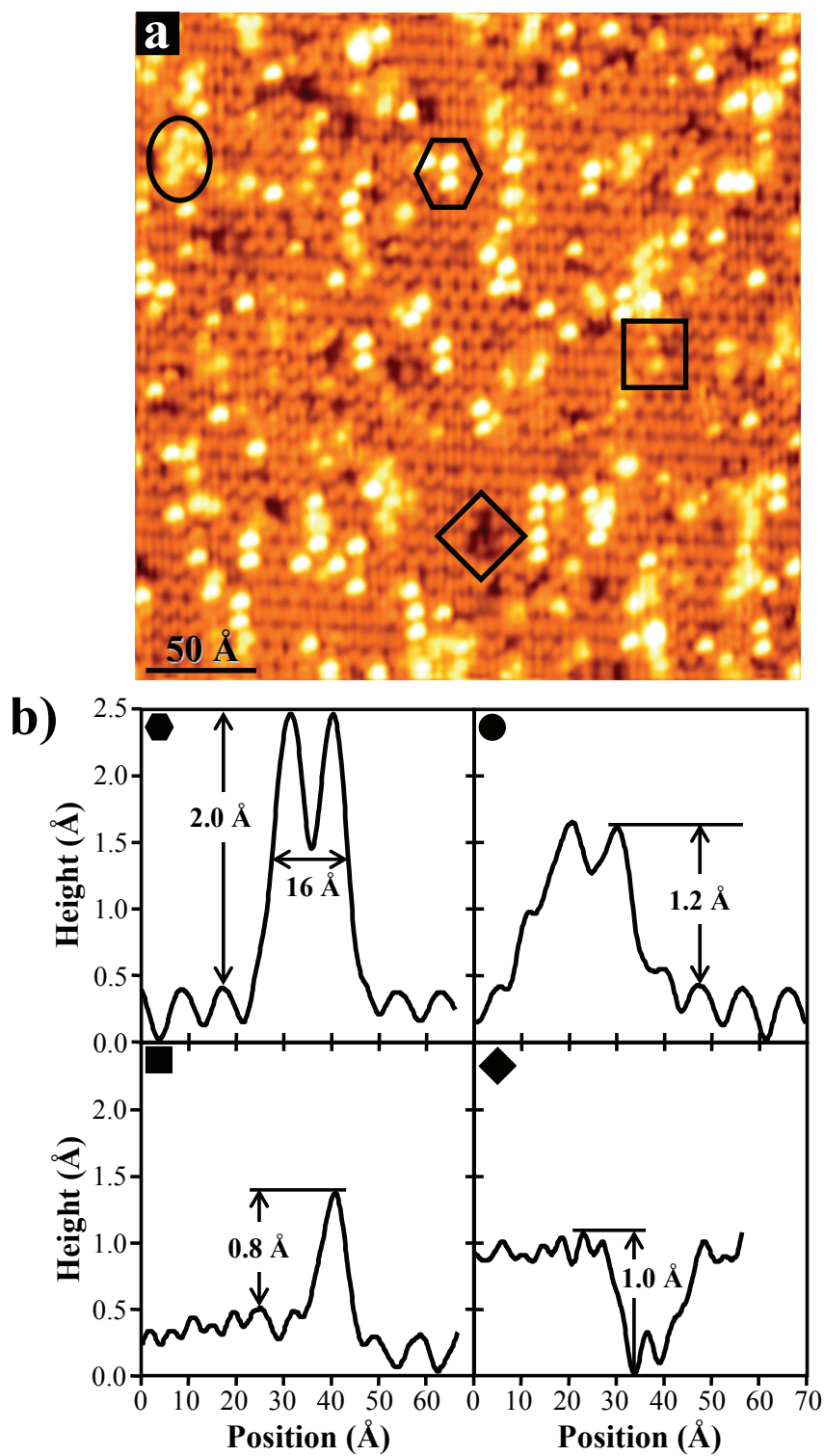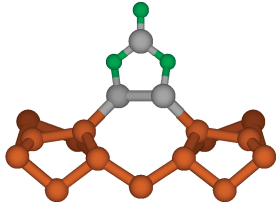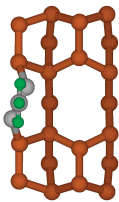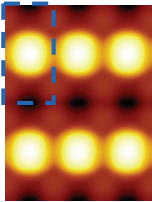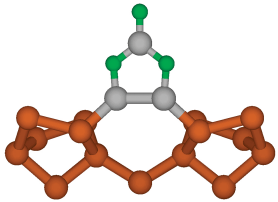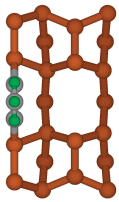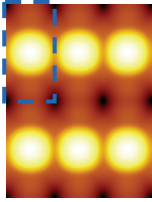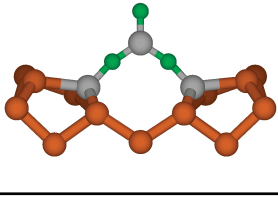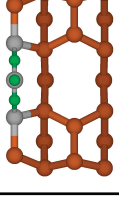
FIGURE 4.2. (a) Filled-state STM image (V_s = -2.0, I_t = 0.2 nA) of ~10% ML SiO deposited onto Ge(100). Image taken after 200ºC anneal. The various observable reaction/adsorbate sites are indicated: $(SiO)_3$ pyramid sites (hexagon), Ge regrowth (oval), SiO monomer or O adsorbate (square), and O displacement (diamond). (b) STM image line-scans of the various indicated reaction sites.

TABLE 4.1. Summary of the various (SiO)$_3$ pyramid sites considered in this work, including ball-and-stick diagrams, STM simulations, and enthalpies of adsorption. Diagrams of calculated (SiO)$_3$ pyramid site cells are given as side and top-down views; top-down view corresponds to dashed line on STM simulations.

Identification	Geometry	STM Simulation	ΔH_{ads} (eV)[a]
Ads-(SiO)$_3$ *[high-Ge's]*			-1.37
Ads-(SiO)$_3$ *[low-Ge's]*			-1.67
Disp-(SiO)$_3$ *[high-Ge's]*			-1.92
Disp-(SiO)$_3$ *[low-Ge's]*			-1.99

a: Calculated adsorption energies, ΔH_{ads}, are given with respect to the clean Ge(100)-4×2 surface and single SiO molecules. Displacement sites are calculated with respect to the creation of Ge ad-dimers.
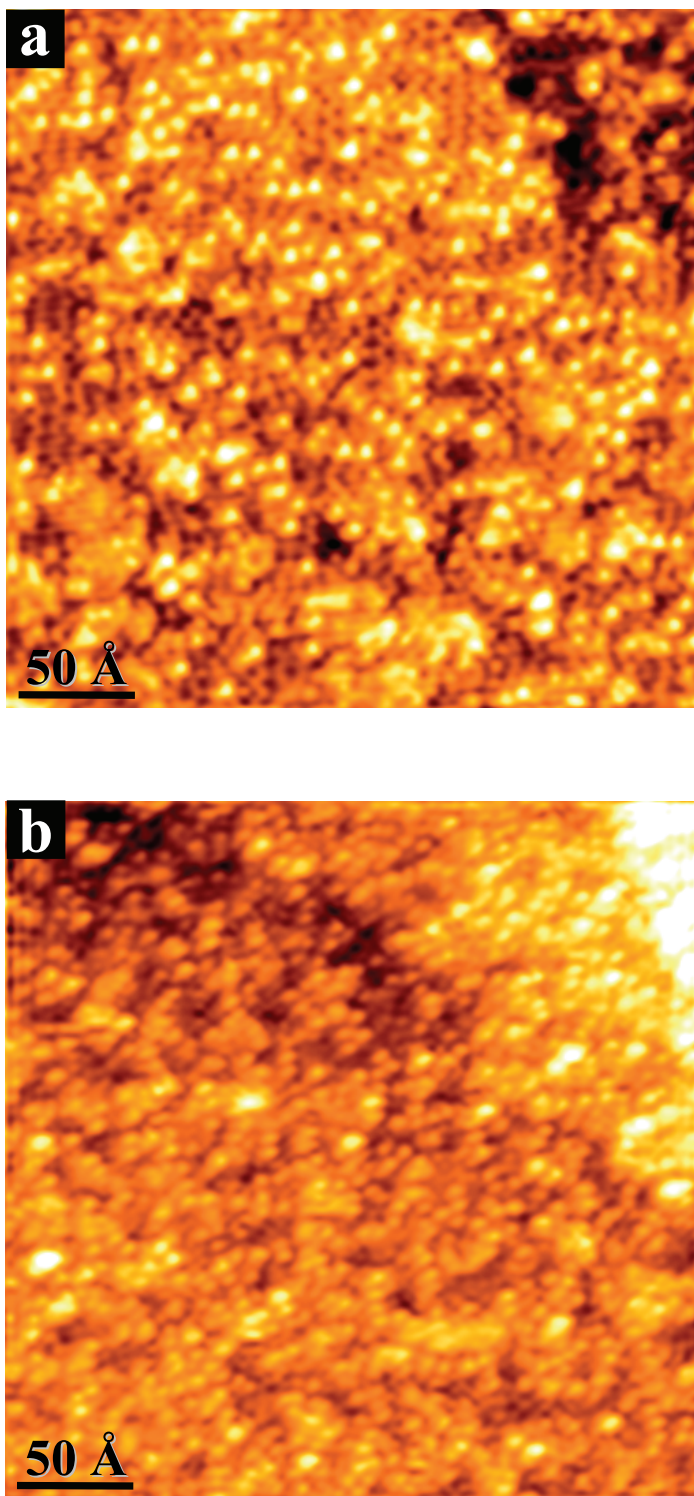
FIGURE 4.3. Filled-state STM image (V_s = -2.0, I_t = 0.2 nA) of (a) ~50% ML and (b) ~1 ML SiO deposited onto Ge(100). Images taken after 200ºC anneal. Note that as the $(SiO)_3$ pyramid coverage increases the image contrast ratio decreases, making the adsorbates appear smaller, though they do remain the same size.
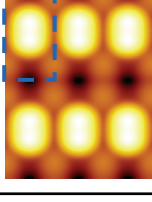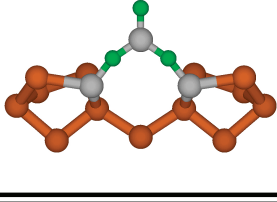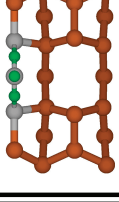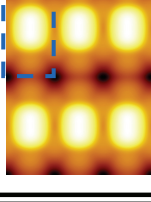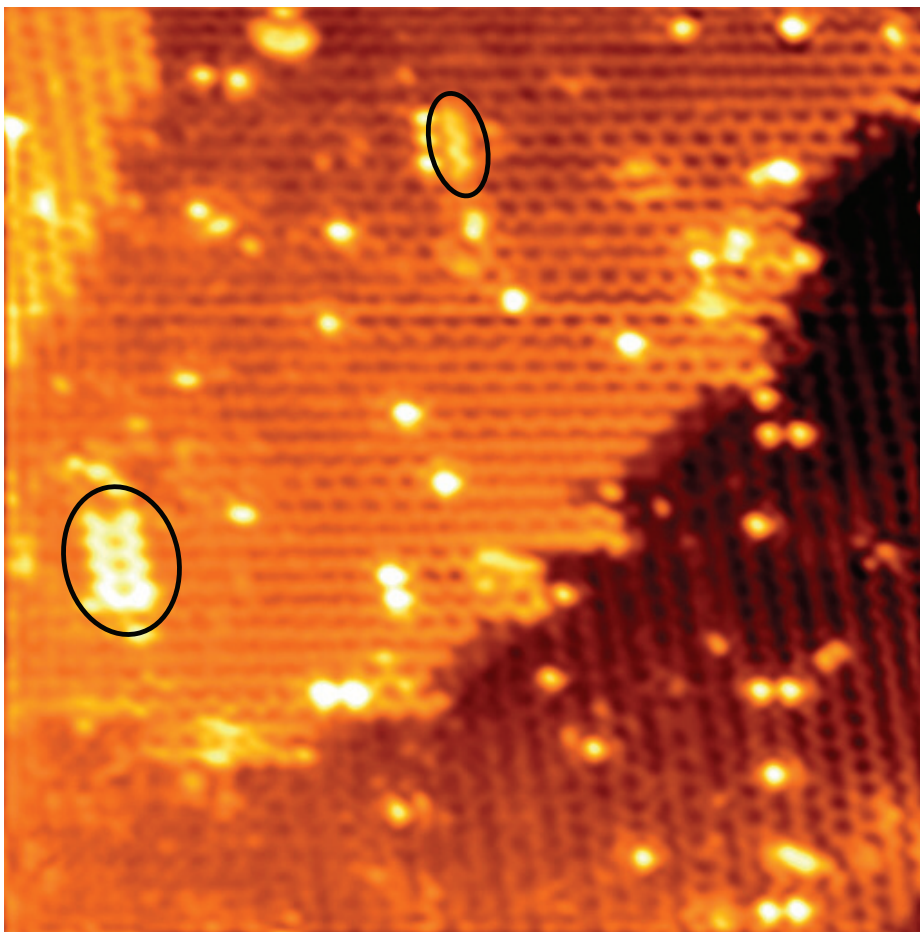
FIGURE 4.4. Filled-state STM image (V_s = -2.0, I_t = 0.2 nA) of ~5% ML SiO deposited onto Ge(100). Image taken after 300ºC. Note roughly equal numbers of Ge regrowth (circled in the image) and $(SiO)_3$ pyramid sites.
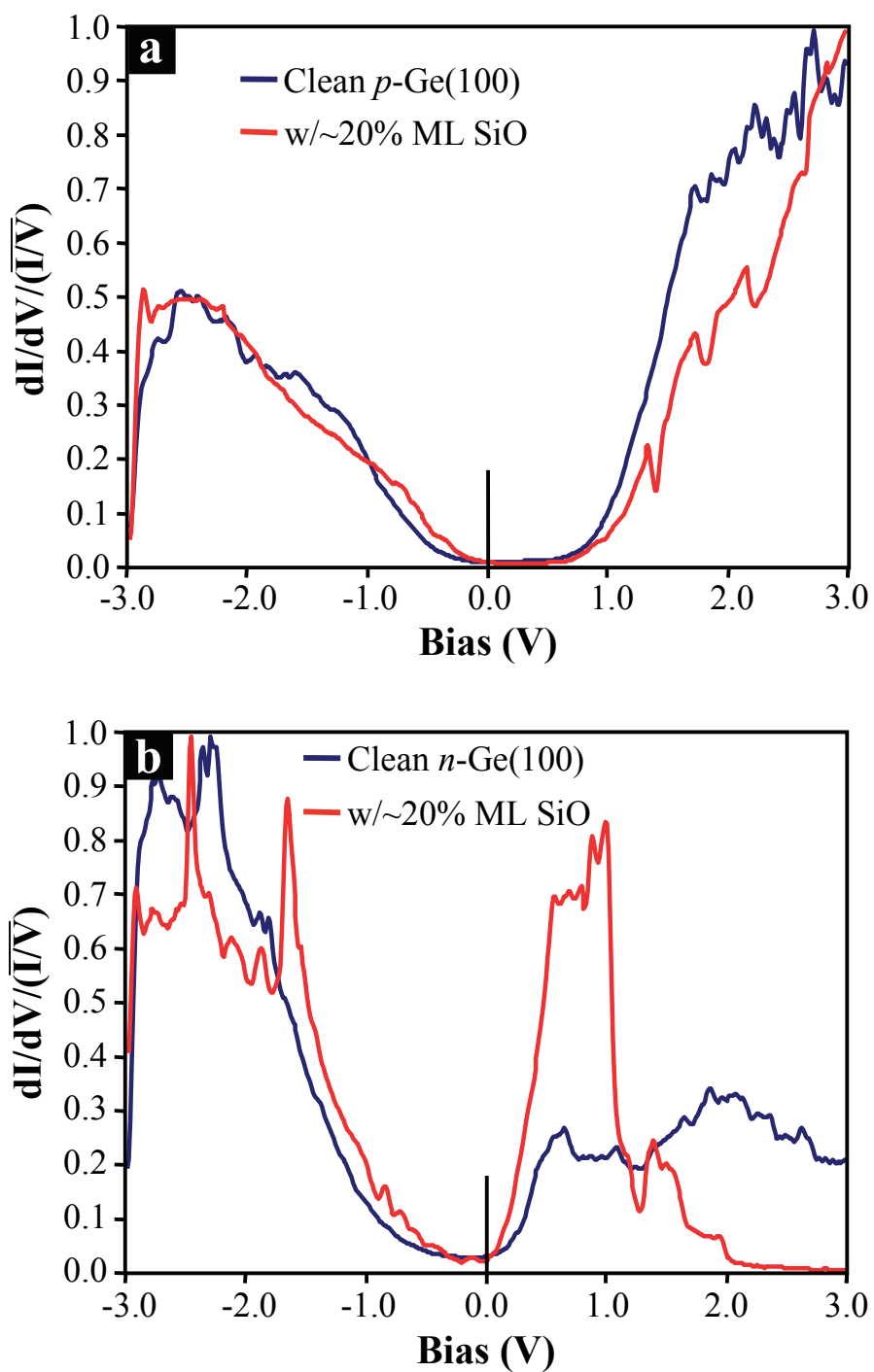
FIGURE 4.5. Scanning tunneling spectroscopy (STS) results for ~20% ML SiO deposited onto (a) p-type and (b) n-type Ge(100), annealed to 200ºC. Note that the Fermi level position (0 V) remains near the valence band (VB) for the *p*-type sample and near the conduction band (CB) for the *n*-type sample, indicative of an unpinned interface.
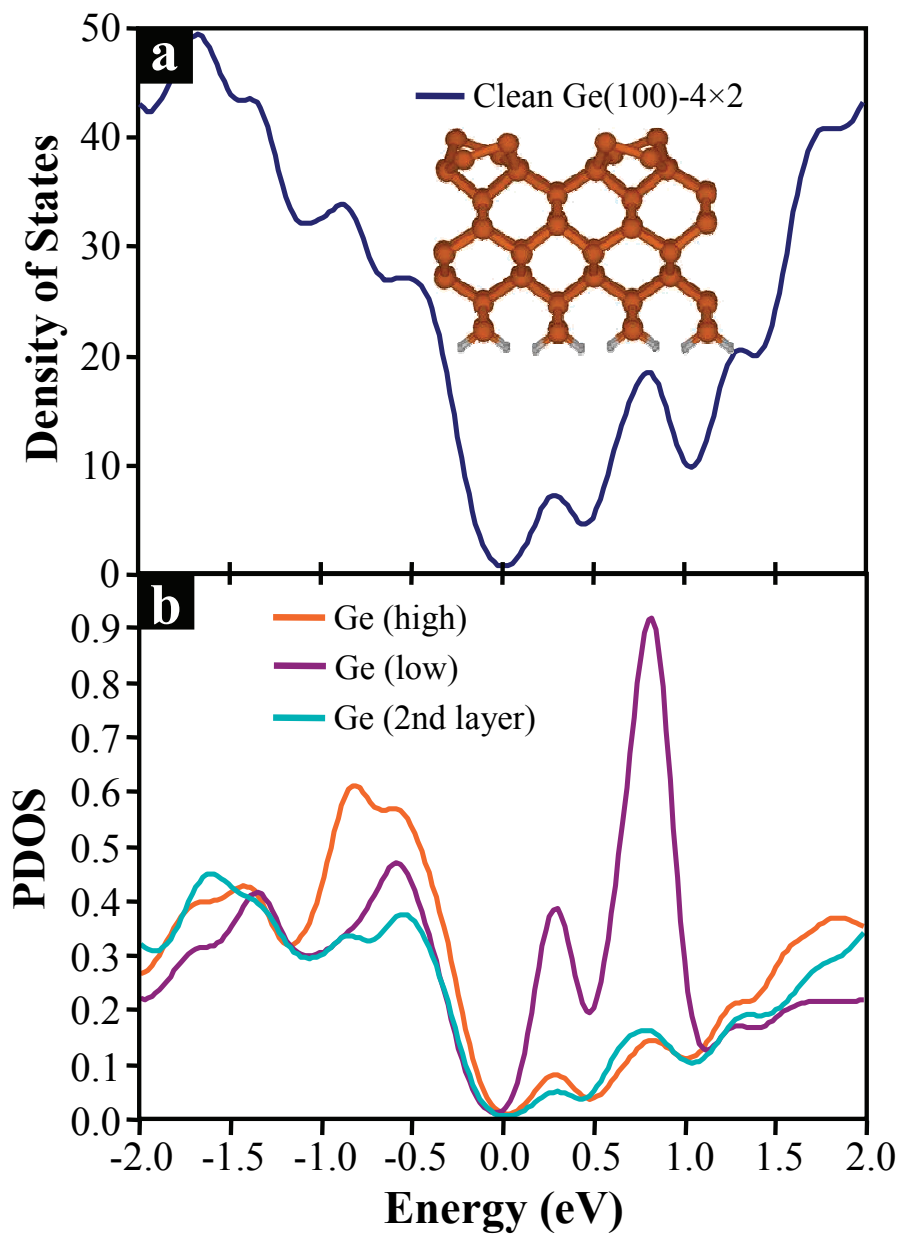
FIGURE 4.6. DFT calculated (a) density of states, DOS, and (b) projected densities of states, PDOS, for clean Ge(100)-4×2. Note the different electronic structures for the high vs. low Ge surface dimer atoms, where the sp^2-like low atom has a large empty-state (CB) density, while the sp^3-like high atom has a greater filled-state (VB) density.
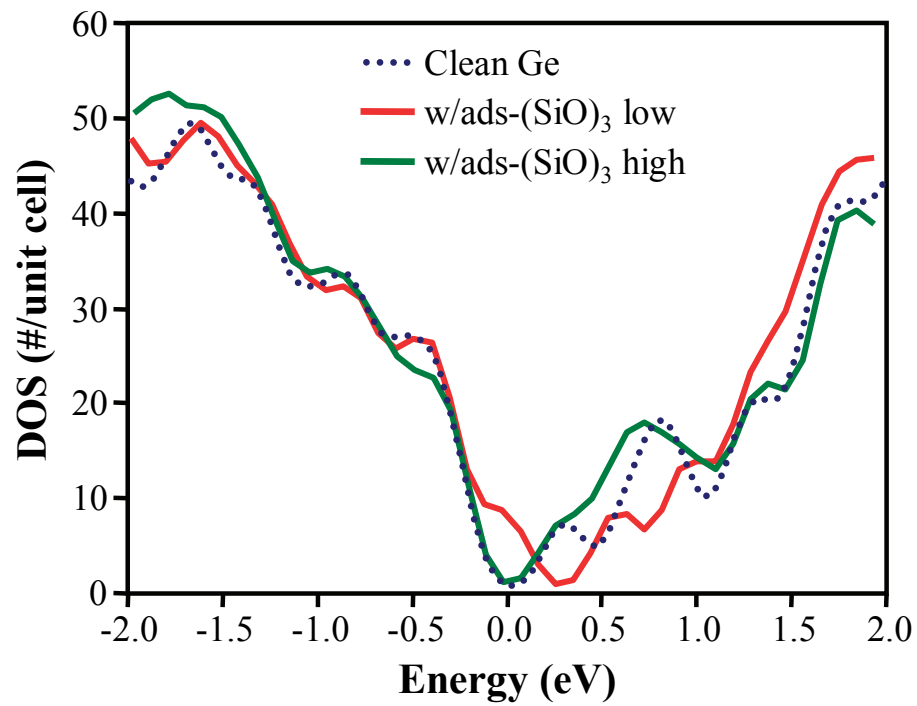
FIGURE 4.7. DFT calculated densities of states for the two different adsorbate-type $(SiO)_3$ pyramid geometries at 25% surface coverage.
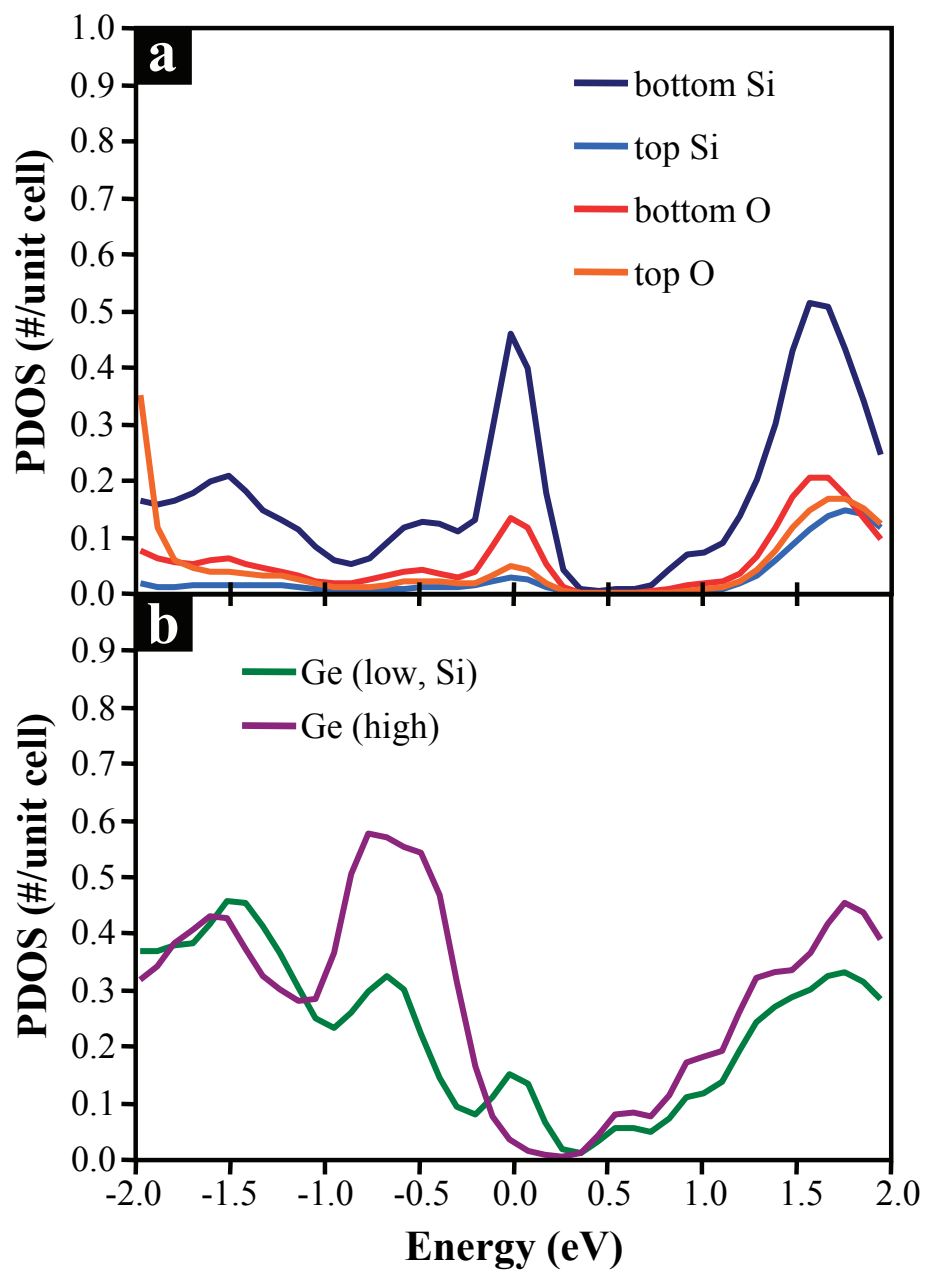
FIGURE 4.8. DFT calculated projected densities of states for the adsorbate-type $(SiO)_3$ pyramid bonded to the low Ge atoms. (a) PDOS of the Si and O atoms and (b) PDOS of the affected surface Ge atoms.
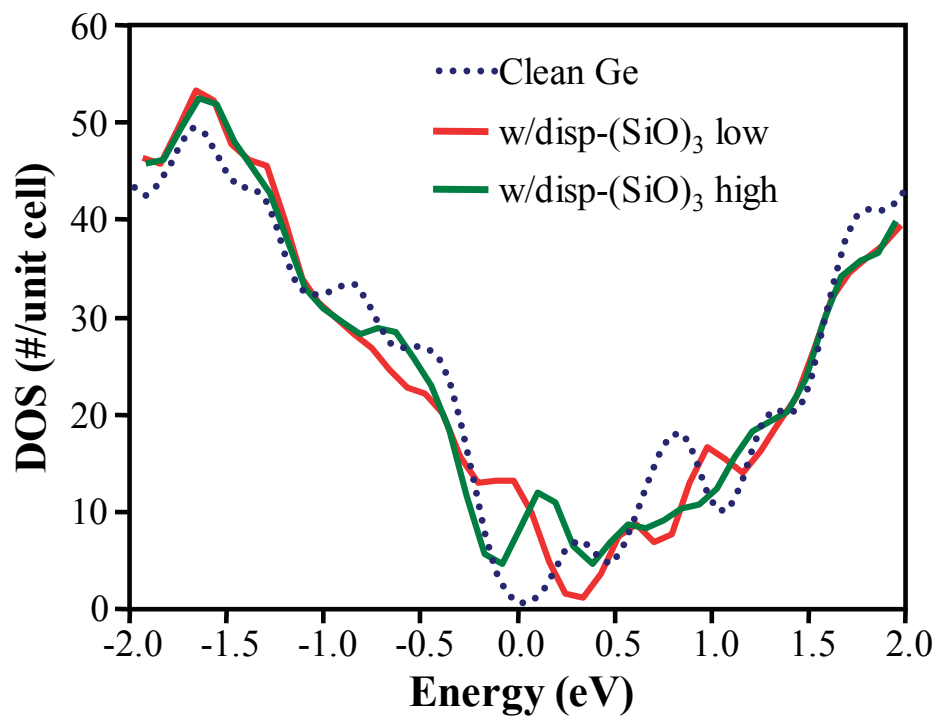
FIGURE 4.9. DFT calculated densities of states for the two displacement-type $(SiO)_3$ pyramid sites at 25% surface coverage.
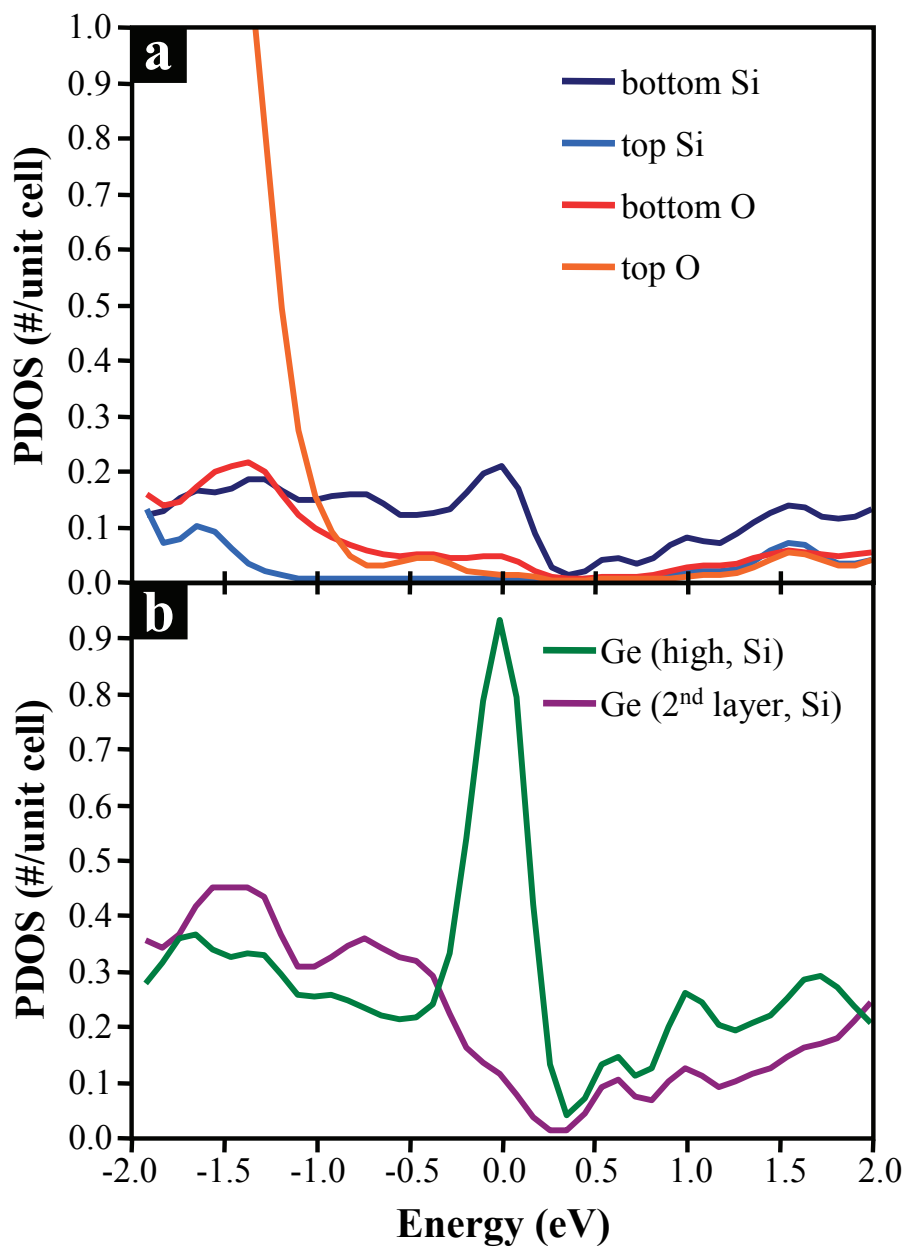
FIGURE 4.10. DFT calculated projected densities of states for the low displacement-type $(SiO)_3$ pyramid, in which the pyramid bottom Si atoms have displaced one low Ge dimer atom on each side of the trough. (a) PDOS of the Si and O atoms and (b) PDOS of the affected surface and second layer Ge atoms.
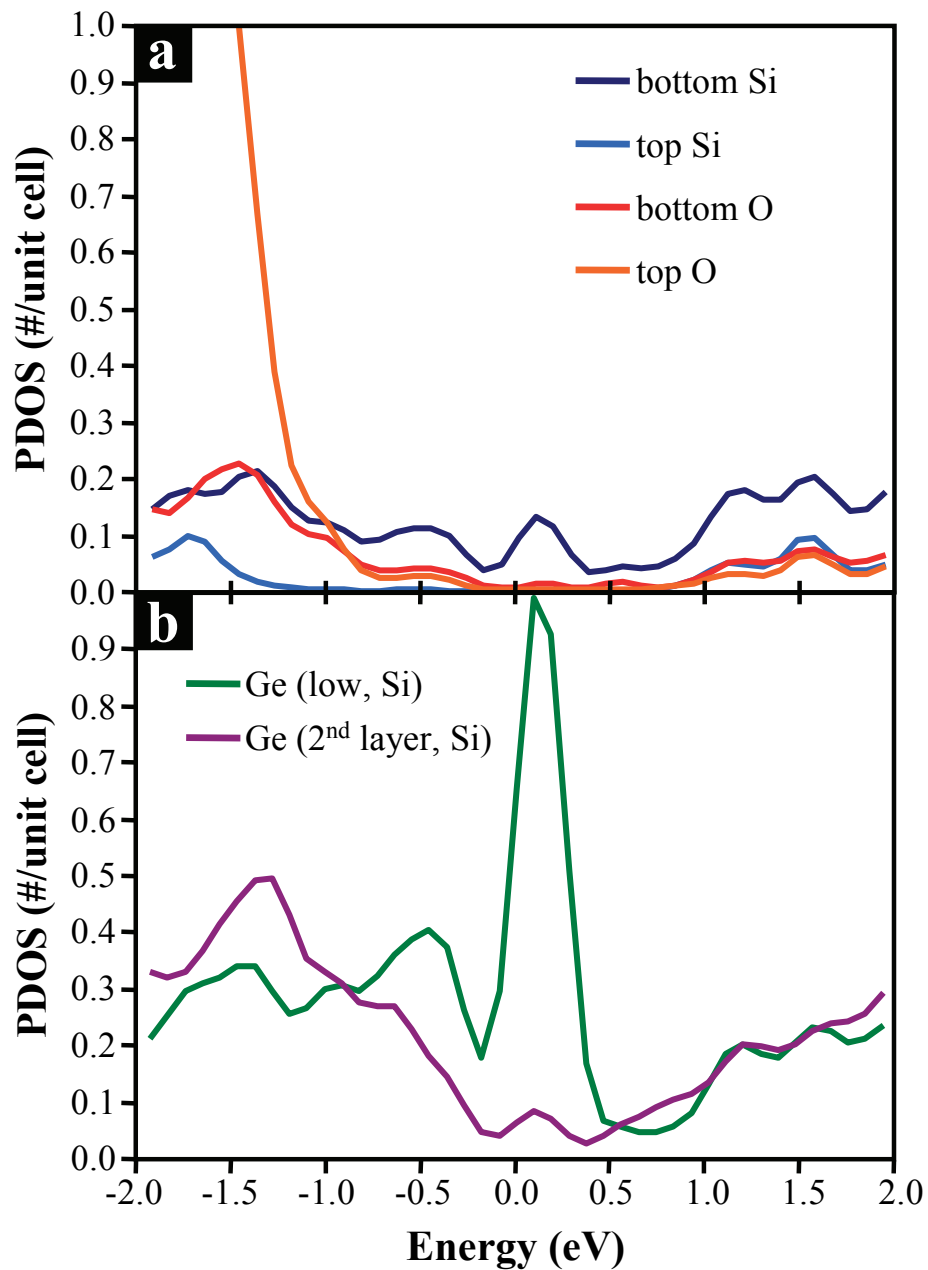
FIGURE 4.11. DFT calculated projected densities of states for the high displacement-type $(SiO)_3$ pyramid, in which the pyramid bottom Si atoms have displaced one high Ge dimer atom on each side of the trough. (a) PDOS of the Si and O atoms and (b) PDOS of the affected surface and second layer Ge atoms.
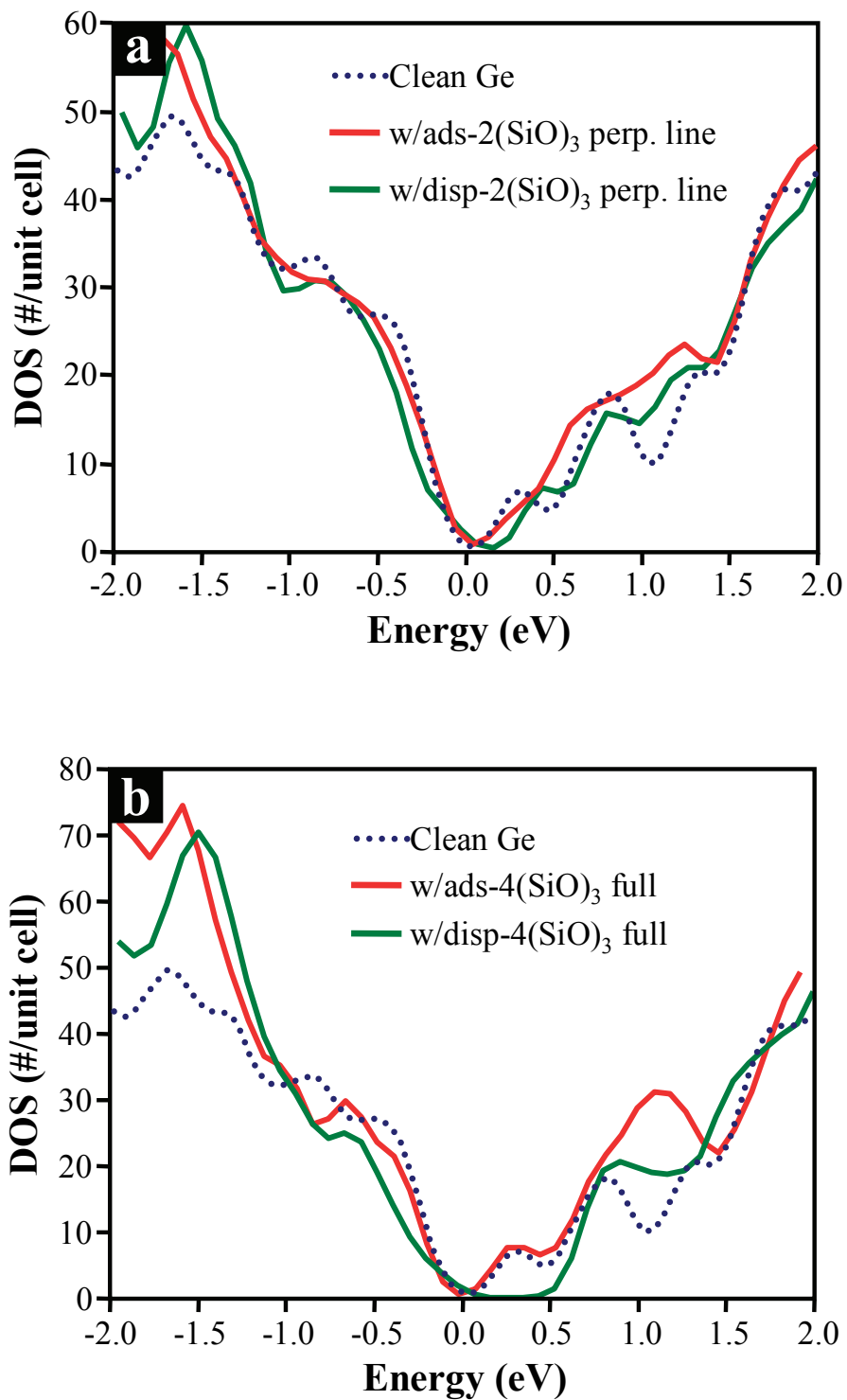
FIGURE 4.12. DFT calculated densities of states for (a) 50% surface coverage and (b) 100% surface coverage (SiO)$_3$ pyramid sites.

4.8 REFERENCES

[1]   R. H. Kingston, J. Appl. Phys. **27** (2), 101 (1956).

[2]   P. W. Loscutoff and S. F. Bent, Annu. Rev. Phys. Chem. **57** (1), 467 (2006).

[3]   K. Prabhakaran, F. Maeda, Y. Watanabe et al., Appl. Phys. Lett. **76** (16), 2244 (2000).

[4]   V. Craciun, I. W. Boyd, B. Hutton et al., Appl. Phys. Lett. **75** (9), 1261 (1999).

[5]   O. J. Gregory, E. E. Crisman, L. Pruitt et al., Mater. Res. Soc. Symp. Proc. **76**, 307 (1987).

[6]   Y. Wang, Y. Z. Hu, and E. A. Irene, J. Vac. Sci. Technol., A **12** (4), 1309 (1994).

[7]   D. B. Alford and L. G. Meiners, J. Electrochem. Soc. **134** (4), 979 (1987).

[8]   S. Huiling, H. Okorn-Schmidt, K. K. Chan et al., IEEE IEDM, 441 (2002).

[9]   C. M. Ransom, T. N. Jackson, and J. F. DeGelormo, IEEE Trans. Electron Devices **38** (12), 2695 (1991).

[10]   R. S. Johnson, H. Niimi, and G. Lucovsky, J. Vac. Sci. Technol., A **18** (4), 1230 (2000).

[11]   M. L. Lee, C. W. Leitz, Z. Cheng et al., Appl. Phys. Lett. **79** (20), 3344 (2001).

[12]   R. A. McKee, F. J. Walker, and M. F. Chisholm, Science **293** (5529), 468 (2001).

[13]   M. Meuris, A. Delabie, S. Van Elshocht et al., Mat. Sci. Semicond. Proc. **8** (1-3), 203 (2005).

[14]   K. C. Saraswat, C. O. Chui, T. Krishnamohan et al., Microelectron. Eng. **80**, 15 (2005).

[15]   T. J. Grassman, S. R. Bishop, and A. C. Kummel, *in preparation* (2007).

[16]   K. T. Queeney, M. K. Weldon, J. P. Chang et al., J. Appl. Phys. **87** (3), 1322 (2000).

[17]   D. A. Muller, T. Sorsch, S. Moccio et al., Nature **399** (6738), 758 (1999).

[18]   M. C. Cheynet and T. Epicier, Philos. Mag. **84** (17), 1753 (2004).

[19]   W. P. Bai, N. Lu, and D.-L. Kwong, IEEE Electron Device Lett. **26** (6), 378 (2005).

[20]   R. M. Feenstra, J. A. Stroscio, and A. P. Fein, Surf. Sci. **181** (1-2), 295 (1987).

[21]   N. D. Lang, Phys. Rev. B **34** (8), 5947 (1986).

[22]   N. Li, M. Zinke-Allmang, and H. Iwasaki, Surf. Sci. **554** (2-3), 253 (2004).

[23]   A. Selloni, P. Carnevali, E. Tosatti et al., Phys. Rev. B **31** (4), 2602 (1985).

[24]   J. Tersoff and D. R. Hamann, Phys. Rev. Lett. **50** (25), 1998 (1983).

[25]   J. Tersoff and D. R. Hamann, Phys. Rev. B **31** (2), 805 (1985).

[26]   J. A. Strosico and R. M. Feenstra, in *Scanning Tunneling Microscopy*, edited by J. A. Strosico and W. J. Kaiser (Academic Press, San Diego, 1993).

[27]   G. Kresse, Thesis, Technische Universität Wien, 1993.

[28]   G. Kresse and J. Furthmüller, Phys. Rev. B **54** (16), 11169 (1996).

[29]   G. Kresse and J. Furthmüller, Comp. Mat. Sci. **6** (1), 15 (1996).

[30]   G. Kresse and J. Hafner, Phys. Rev. B **47** (1), 558 (1993).

[31]   P. E. Blöchl, Phys. Rev. B **50** (24), 17953 (1994).

[32]   G. Kresse and D. Joubert, Phys. Rev. B **59** (3), 1758 (1999).

[33]   J. Paier, R. Hirschl, M. Marsman et al., J. Chem. Phys. **122** (23), 234102 (2005).

[34]   D. L. Winn, M. J. Hale, T. J. Grassman et al., J. Chem. Phys. **126** (8), 084703 (2007).

[35]   T. Fukuda, Surf. Sci. **417** (2-3), L1149 (1998).

[36]   T. Fukuda and T. Ogino, Phys. Rev. B **56** (20), 13190 (1997).

[37]   T. Fukuda and T. Ogino, Appl. Surf. Sci. **130-132**, 165 (1998).

[38]   T. Fukuda and T. Ogino, Appl. Phys. A **66** (0), S969 (1998).

[39]   W. E. Spicer, P. W. Chye, P. R. Skeath et al., J. Vac. Sci. Technol. **16** (5), 1422 (1979).

[40]   W. E. Spicer, Z. Liliental-Weber, E. Weber et al., J. Vac. Sci. Technol., B **6** (4), 1245 (1988).

[41]   O. Gurlu, H. J. W. Zandvliet, and B. Poelsema, Phys. Rev. Lett. **93** (6), 066101 (2004).

[42]   J. P. Perdew and M. Levy, Phys. Rev. Lett. **51** (20), 1884 (1983).

[43]   L. J. Sham and M. Schlüter, Phys. Rev. Lett. **51** (20), 1888 (1983).

CHAPTER FIVE

Density Functional Theory Study of First-Layer Adsorption of

ZrO$_2$ and HfO$_2$ on Ge(100)

5.1 ABSTRACT

Density functional theory was used to performed a survey of transition metal oxide (MO$_2$ = ZrO$_2$, HfO$_2$) ordered molecular adsorbate bonding configurations on the Ge(100)-4×2 surface. Surface binding geometries of metal-down (O-M-Ge) and oxygen-down (M-O-Ge) were considered, including both adsorbate and displacement geometries of M-O-Ge. Calculated enthalpies of adsorption show that bonding geometries with metal-Ge bonds (O-M-Ge) are essentially degenerate with oxygen-Ge bonding (M-O-Ge). Calculated electronic structures indicate that adsorbate surface bonding geometries of the form O-M-Ge tend to create a metallic interfaces, while M-O-Ge geometries produce, in general, much more favorable electronic structures. Hydrogen passivation of both oxygen and metal dangling bonds was found to improve the electronic structure of both types of MO$_2$ adsorbate systems, and induced the opening of true semiconducting band gaps for the adsorbate-type M-O-Ge geometries. Shifts observed in the DOS minima for both O-M-Ge and M-O-Ge adsorbate geometries are consistent with surface band bending induced by the adsorbate films, where such band bending extends much further into the Ge substrate than can be modeled by the Ge slabs used in this work.

5.2 INTRODUCTION

Due to the approach of the fundamental limits of classical silicon CMOS scaling, recent years have seen a great deal of work focused on alternative channel materials for high-speed MOS-type field-effect transistors. One such alternative material is germanium, whose greater low-field intrinsic carrier mobilities may provide for a significant increase in saturation current over state-of-the-art silicon MOSFET devices. However, in contrast to Si, Ge does not have a suitably stable electrically-passivating native oxide. The Ge native oxide, GeO_2, is both water-soluble and thermally unstable at elevated temperatures; GeO_2 decomposes and desorbs as GeO above 400ºC.[1-3] Therefore, an alternative dielectric and/or electrical passivation method is needed.

Numerous experiments have attempted the fabrication of Ge-based MOSFET or MOSCAP devices using a great diversity of insulators, including GeO_2,[4-6] Ge_3N_4,[7] GeO_xN_y,[5,8,9] SiO_2 (with and without a Si interlayer/cap),[10,11] and high-k metal-oxides ($BaStTiO_3$, ZrO_2, HfO_2).[12-14] The success of these different dielectric materials has been found to depend greatly on the nature of the semiconductor-oxide interface. The most studied, and probably most successful, gate dielectric materials are the transition metal dioxides ZrO_2 and HfO_2 (denoted as MO_2 in this manuscript), usually grown by atomic layer deposition (ALD). These oxides, under normal Ge processing conditions, are amorphous, and depending on initial native oxide content (as well as composition) on the Ge(100) surface, the oxide/Ge interface may be either abrupt or contain some germanate interlayer (though these interlayers are thinner than those found with Si). High resolution TEM imaging indicates that ZrO_2 tends to form more abrupt interfaces, while HfO_2 has

been shown to be more likely to form interfacial interlayers.[15] The TEM images also seem to indicate that the abrupt oxide/Ge interface may be somewhat ordered, even though the rest of the oxide layer is amorphous.

MOSFET (and MOSCap) device quality is found to vary greatly in these MO_2/Ge(100) gate stacks, with the trend closely related to the oxide-semiconductor interface quality and composition (i.e. clean vs. oxidized surface, native oxide vs. oxynitride, abrupt vs. interlayer interface, etc.).[16] Currently available data, however, is not accurate or precise enough to sufficiently characterize the oxide/Ge interface, so detailed conclusions about the exact causes of problems related to the interface in these devices are unable to be made. It is hoped that carefully performed high resolution scanning transmission electron microscopy (STEM) will enable a close look at the structure at the oxide/semiconductor interface to reveal the extent of order at these interfaces and to elucidate the basic bonding structure as metal-O-Ge, O-metal-Ge, or a combination of the two.

We have performed a survey of potential ordered oxide/semiconductor interface structures between stoichiometric molecular ZrO_2/HfO_2 and Ge(100), considering both surface coverage and surface binding configuration (O-metal-Ge bonding vs. metal-O-Ge bonding) using density functional theory (DFT) modeling. This work is by no means intended to be an exhaustive set of structures, but merely an attempt to provide some insight into the MO_2/Ge interfacial system. Additionally, these structures will serve as precursors to later computational studies of thick amorphous MO_2 layers on Ge(100).

5.3 METHODS

All density functional theory (DFT) calculations presented in this paper were performed using the Vienna Ab-Initio Simulation Package (VASP)[17-20] in the generalized gradient approximation (PBE exchange-correlation functional), with projector augmented wave (PAW) potentials[21,22] (as supplied by the VASP group), a 4×4×1 Monkhorst-Pack k-point mesh generation scheme (for a total of 4 irreducible k-points), and plane-wave basis cut-off of 450 eV. All parameters (i.e. k-points, cut-off energy, vacuum space, slab thickness, etc.) were chosen such that they were each individually converged to within 1 meV/atom for the system of study. The absolute error of this type of calculation is estimated to be up to 0.37 eV,[23] but it is difficult to estimate the exact error with respect to the SiO/Ge(100) system presented in this report. Regardless of absolute numerical accuracy, the qualitative results from these calculations should be quite reasonable because comparisons are being made merely between different bonding geometries that have all been calculated under identical conditions and with similar types of bonds. Therefore, the calculations in this paper should have good relative accuracy, with an estimated relative error of ± 0.1 eV.[24]

The system studied consisted of an Ge(100) slab supercell with a 4×2 surface dimer reconstruction, as this is the lowest energy configuration (compared to the 2×1 flat dimer and 1×1 unreconstructed geometries). The germanium slab was 8 atomic layers thick, with each layer being 2×4 atoms in area, for a total of 64 Ge atoms per unit cell (for the clean, Ge surface/substrate calculations), shown in Figure 5.1a (inlay). The bottom of the slab was unreconstructed and terminated with 16 hydrogen atoms (two H

atoms per Ge). The clean Ge supercell contained 12 atomic layers of vacuum space in the z-direction. The bottom three Ge layers were constrained to the minimum-energy bulk DFT geometry, which was found through a series of bulk Ge calculations to have a lattice parameter of 5.795 Å (2.6% larger than the experimental result of 5.646 Å due to the well-known GGA overestimation of lattice parameters). The terminating H atoms were initially allowed to relax and were kept fixed at these optimized positions for all subsequent calculations. All other atoms (upper substrate, adsorbate, gas-phase) were allowed to structurally relax with respect to interatomic forces to a tolerance of 0.01 eV/Å.

5.4 RESULTS AND DISCUSSION

Metal oxide molecules (MO_2 = ZrO_2, HfO_2) were placed on the Ge(100)-4×2 surface at appropriate (chemically sensible) coverages in two different surface binding configurations: O-M-Ge, where the metal atoms bond directly to the Ge surface, and M-O-Ge, where the oxygen atoms bond directly to the Ge surface. The M-O-Ge configuration also consisted of two distinct sub-configurations: displacement-type, where the O atoms displace surface Ge atoms, and adsorbate-type, where the O atoms bind to the dangling bonds of the Ge atoms. Adsorption enthalpies were extracted from these calculations using the Hess's law method of "products minus reactants." A summary of the geometries modeled and their calculated enthalpies of adsorption can be found in Table 5.1. The systems were also analyzed for electronic structure (density of states) information in order to determine passive or pinning oxide bonding to the surface.

It must be noted, however, that there are well-known problems with standard LDA- and GGA-based DFT with respect to the electronic structures of semiconducting and insulating materials, namely a general underestimation of the band gap by 30 – 100%, due to the approximation of the exchange potential.[25,26] Unfortunately, this problem is at its worst for small band gap semiconductors, such as germanium. In fact, standard DFT predicts a slight overlap of the Ge VB maximum and CB minimum, producing a semi-metallic electronic structure (see Figure 5.1a). Clearly these calculations would benefit from being performed under a higher level of theory, such as the inclusion of exact exchange (i.e. hybrid functionals). We do intend to perform this work, but as these higher-level calculations are about two orders of magnitude more expensive that standard DFT, they are far from being completed.

However, because there is still a significant minimum in the DOS at the Fermi level, it is possible to extract useful information from standard DFT calculations of Ge(100). Specifically, one may compare the calculated DOS of the clean Ge(100)-4×2 slab with the DOS of the various Ge(100) slabs with oxygen adsorbates on them. Because we are particularly interested in the induction of electronic states within the band gap, a potential cause of Fermi level pinning, special attention will be paid to the near-Fermi level region of the calculated densities of states. There are two general possible conditions related to the DOS after the addition of the metal-oxide adsorbates to the Ge(100) surface: (a) the DOS at the near-E_F region decreases (or exhibits no change) after the addition of the MO_2 adsorbates, or (b) the DOS at the near-E_F region increases after the addition of the MO_2 adsorbates. If the DOS decreases or shows no change, it is reasonable to conclude that the adsorbate is not a potential source of Fermi level pinning,

while if the DOS increases it is reasonable to conclude that pinning is possible because of the induction of band gap or band edge states that are consistent with Fermi level pinning.

For the sake of comparison between the clean Ge(100)-4×2 and MO_2 adsorbate-covered Ge(100) surfaces, we align the calculated densities of states using the Ge band edge located at about -12 eV (the deepest Ge-based DOS feature available in these calculations). Because of the lack of band gap in these simulations the calculated Fermi level for the majority of the various systems modeled has little meaning. Therefore, the calculated Fermi level for the MO_2/Ge(100) systems shall be indicated in the DOS figures but shall not be considered in the analysis of most of the computational results. In the case where the calculated Fermi level of a MO_2/Ge(100) system actually is meaningful (e.g. in the case where the MO_2 adsorption yields a system band gap), it shall be pointed out and discussed. The x-axis (energy) on each presented DOS figure in this manuscript is reliable only for the clean Ge(100)-4×2 plot.

With this method of DOS alignment, we can directly visualize any changes in the density of states that may have occurred due to the addition of MO_2 molecules, particularly any changes at or near the clean Ge(100) near-E_F (i.e. the zero volts position). The projected density of states (PDOS), which is essentially the local DOS for each individual atom in the computational system (e.g. see Fig. 5.1b for PDOS of the two different Ge surface dimer atoms), can provide additional insight into any observed changes in the electronic structure.

B. O-M-Ge Surface Binding of MO$_2$ on Ge(100)

1. Half-Coverage O-M-Ge Adsorption

To simulate a metal-Ge interface at the first layer of MO$_2$ on the Ge(100) surface molecular ZrO$_2$ and HfO$_2$ were adsorbed to the surface in a metal-down, or O-M-Ge, bonding configuration (see Figure 5.2a). Such a configuration models atomic layer deposition (ALD) growth in which the metal atoms are deposited first onto the clean surface. In this particular O-M-Ge geometry, the metal atom binds directly to the Ge dangling bonds, with half the oxygen atoms pointing upward (away from the surface) and half sideways, bonding with the next metal atom over. This particular system only utilizes half of the number of available Ge bonding sites (i.e. in this case the Ge-Ge surface dimers are left intact), and is designated half-coverage. This geometry yielded enthalpies of adsorption for the MO$_2$/Ge(100) system of -3.16 eV/ZrO$_2$ and -3.63 eV/HfO$_2$.

The half-coverage O-M-Ge configuration was found to induce a large DOS at the zero-volt position (which is very close to the system's calculated Fermi level), as seen in the system densities of states from both ZrO$_2$ and HfO$_2$ cases, shown in Fig. 5.2b. The PDOS for the ZrO$_2$ case is presented in Fig. 5.2c (the PDOS for HfO$_2$ is nearly identical). The increased DOS appears to be a result of a downward shift of the near-E$_F$ CB states belonging to the sp^2-like (i.e. mostly empty dangling bond) "low" buckled dimer atoms as they are forced flat by the bonding of the MO$_2$ adsorbates. On the clean Ge(100) surface, flat dimers possess exactly half-filled dangling bonds, which produces small metallic states within the band gap.[27] Therefore, it seems that the metal-Ge bonds being

formed in this O-M-Ge adsorbate configuration may be more metallic in nature than covalent, where we would expect to see these states shifted out of the near-E_F region due to the molecular orbital split into sigma bonding and antibonding states.

2. Half-Coverage H-O-M-Ge Adsorption

The upward pointing oxygen atoms in the previous O-M-Ge adsorbate geometry have partially-filled dangling bonds and simple reasoning indicates that they may possess electronic states near or at the Fermi level, possibly playing a role in the large observed induction of near-E_F DOS. It is also possible, given the high electronegativity of oxygen atoms, that they could be withdrawing excessive amounts of charge from the Zr/Hf atoms, thereby inducing the observed DOS shift. Passivation of these dangling bonds with H atoms would eliminate the partially-filled dangling bonds and limit the O atoms' capacity for charge withdrawal from the neighboring metal atoms. Additionally, the termination of the O dangling bonds would act in a similar manner as further oxide growth, comparable to the use of H passivation on the bottom of the Ge slab.

Figure 5.3 presents the results of the H passivation of the half-coverage O-M-Ge adsorption geometry. We find that while the passivation has indeed eliminated much of the near-E_F oxygen DOS, it has not removed the increased DOS at the Fermi level (see Fig. 5.3b). In fact, the PDOS for the surface Ge and Zr atoms has actually increased as a result, seen in Fig. 5.3c. Most likely this is actually a consequence of charge being forced back into the metal atoms (because of the charge withdrawal limitations placed upon the O atoms by the H passivation), and thereby back into the metallic M-Ge bonding states.

For both the passivated and unpassivated O-M-Ge geometries we consider the shift of the near-E_F DOS minima (see Figs. 4.2b and 4.3b), especially the gap-like situation seen for the H-O-M-Ge case. A possible explanation for this behavior is band bending induced by the MO_2 adsorbate films. For a thick doped sample, band bending should induce a decrease or elimination of an observable band gap in the total DOS. However, band bending for an intrinsic semiconductor is expected to extend much further into the semiconductor than can be modeled with the current Ge(100) slab. Therefore, for the eight layer intrinsic slab employed in our calculations, the band bending should appear as just a shift in the band gap (or DOS minimum) with respect to the original clean Ge(100)-4×2 DOS minimum, such as that observed for the O-M-Ge adsorbate geometries.

3. Full-Coverage H-O-M-Ge Adsorption

As a final check into the O-M-Ge type adsorbate bonding configuration, metal oxide molecules were also inserted into the Ge dimers, giving a full coverage MO_2/Ge(100) system (see Figure 5.4a). We present only the H-passivated version of this geometry because the difference between the passivated and the non-passivated geometries is the same as for the half-coverage case (the removal of some of the near-E_F oxygen DOS makes for easier visualization). This full coverage geometry produces a network of -M-Ge-M- bonding, compared to the half-coverage case where the metal atoms were always separated by two Ge atoms (-M-Ge-Ge-M-). If the hypothesis of metallic M-Ge bonding derived from the half-coverage case is valid, we would expect the full-coverage case to display even greater metallic bonding character. The average

adsorption energy per MO_2 molecule calculated for the full-coverage case was -2.78 eV/ZrO_2 and -3.29 eV/HfO_2, noticeably lower than for the half-coverage case but still considerably exothermic.

As shown in Fig. 5.4b, the metallic DOS near and at the Fermi level is indeed greatly increased. The calculated PDOS, given in Fig. 5.4c, indicates the near-E_F DOS is primarily due to the surface Ge and metal atoms, just like in the half-coverage geometries, but in this case there is no minimum above the Fermi level. Since there is no shifted band gap, the issue of band bending is probably not relevant. Therefore, even within the limited accuracy of the DOS calculations, the greatly increased PDOS of the metal-Ge bonding network demonstrates a clear metallic nature, which is likely to cause problems in a MOSFET device.

B. M-O-Ge Surface Binding of MO_2 on Ge(100)

1. Half-Coverage M-O-Ge Displacement

To simulate an oxygen-Ge interface for the first layer of MO_2 on the Ge(100), surface molecular ZrO_2 and HfO_2 were adsorbed to the surface in an oxygen-down, or M-O-Ge, bonding configuration via a Ge displacement reaction. Two M-O-Ge bonding geometries were studied: the first consists of oxygen displacement of surface Ge atoms (see Figure 5.5a), similar to that seen in the case of the oxidation reaction of Ge(100),[28] while the second M-O-Ge binding geometry is a simple adsorption bonding configuration. The displacement geometry replaces all of the surface Ge atoms with O atoms, and includes one metal atom for every two oxygen atoms to maintain the MO_2

stoichiometry. Because this system contains the same number of MO_2 molecules as the half-coverage O-M-Ge, it is also denoted as half-coverage. This geometry yielded enthalpies of adsorption for the MO_2/Ge(100) system of -1.62 eV/ZrO_2 and -2.13 eV/HfO_2 (note: these enthalpies include the formation enthalpy of Ge ad-dimers by the displaced Ge atoms). These enthalpies are considerably lower than for the O-M-Ge cases, as well as the other M-O-Ge that shall be discussed later in this report. With such comparatively low adsorption energies, we would not expect this site to form, and one might actually expect molecules of this sort of desorb from the surface at standard processing temperatures (500 – 600ºC).

Regardless of the low adsorption energy, it is insightful to examine the calculated electronic structures for the displacement-type M-O-Ge geometry. As seen in Figure 5.5b, there is an increase in the near-E_F DOS for the MO_2/Ge(100) systems, but the minima are still located at basically the same spot as the clean Ge(100)-4×2 minimum. There is a noticeable decrease in filled-state density (VB) and an increase in empty-state density (CB); the calculated Fermi level is found to reside 0.3 eV above the clean Ge(100) position due to the different filling of electronic states resulting from the change in DOS. The PDOS for this system (see Fig. 5.5c) shows that increase in CB density is due entirely to the metal atoms, while the reduction in VB density appears to have occurred at the second layer Ge atoms to which the O atoms are bonded. These results are entirely consistent with large charge withdrawal from both the metal and Ge atoms by the electronegative O atoms. However, the induced near-E_F DOS changes are nowhere near as extreme as those for high-coverage O_2 displacement configurations reported elsewhere.[28] This is most likely due to the fact that the metal atoms act as good electron

donors to the O atoms reducing the charge withdrawal from the Ge atoms (and thus reducing the ionic character of the O-Ge bonds), thereby decreasing the perturbation of the Ge electronic structure.

2. Half-Coverage M-O-Ge Adsorption

To simulate a simple non-displacement M-O-Ge interface, ZrO_2 and HfO_2 molecules were adsorbed to the Ge(100)-4×2 surface oxygen-down (see Figure 5.6a). In this geometry, the O atoms bind directly to the Ge dangling bonds, the MO_2 molecules bridge the trough between dimer rows, and the M atoms point upward away from the surface. This adsorbate system only utilizes half of the number of available Ge bonding sites (i.e. the Ge-Ge surface dimers are left intact), and is therefore also denoted as half-coverage. This geometry yielded enthalpies of adsorption for the MO_2/Ge(100) system of -2.97 eV/ZrO_2 and -3.67 eV/HfO_2, within only 0.2 eV of the half-coverage O-M-Ge geometries.

The half-coverage M-O-Ge geometry is found to display distinct densities of states for the ZrO_2 and HfO_2 systems. Seen in Figure 5.6b, the ZrO_2/Ge(100) system possesses a slightly shifted near-E_F DOS minimum compared to the clean Ge(100) surface. The HfO_2/Ge(100) system also possesses a near-E_F DOS minimum, shifted 0.3 eV up from the clean Ge(100) DOS minimum, but there exists a new peak centered at the clean Ge(100) Fermi level position. The rest of the two densities of states are nearly identical.

Examination of the ZrO_2/Ge(100) system PDOS, presented in Figure 5.7a, clearly shows that the vast majority of the surface electronic state density belongs to the metal

(Zr) atoms. The same holds true for the HfO$_2$/Ge(100) case (see Fig. 5.7b). The Ge and O band edge states for the two systems are nearly identical and comparatively small. The 0 eV position in the Zr PDOS shows a state density minimum, but the same location for the Hf case displays a distinct, unexpected peak. This peak may correspond to the small shoulder in the CB PDOS for the Zr system, denoted in Fig. 5.7a by the arrow. HfO$_2$(g) has a smaller HOMO-LUMO splitting (about half) than ZrO$_2$(g), consistent with these adsorbates have distinct electronic structures. However, it is also possible that the small 0 eV state for HfO$_2$/Ge in seen Fig. 5.6b is due to the previously-discussed errors in the density functional theory.

3. Half-Coverage H-M-O-Ge Adsorption

Similar to the upward-pointing oxygen atoms in the O-M-Ge configuration, the metal atoms in the M-O-Ge configuration are expected to possess partially-filled dangling bonds. In bulk MO$_2$, each metal atom makes four bonds to neighboring oxygen atoms. Therefore, in order to explore the effect of the dangling bonds on the electronic structure of the interface, the metal atoms were passivated with two H atoms each (see Figure 5.8a). We note this bond termination should act as a simulation of further oxide growth, but with the caveat that H atoms are not as good of electron acceptors as O atoms.

Figure 5.8b presents the calculated total densities of states for the two H-passivated M-O-Ge MO$_2$/Ge(100) adsorbate geometries. We see that the H passivation has reduced some of the empty-state (CB) state density, as well as opened true band gaps for both systems, though these gaps do not align with the clean Ge(100)-4×2 Fermi level.

We know that these are true band gaps because the DOS goes to zero at the minimum, the calculated Fermi level lies in the middle of the minimum, and the Kohn-Sham orbitals in that energy range are empty. It is interesting that a band gap should form for these systems given the lack of true gap for the clean Ge case, but we note that the formation of this gap is consistent with the strong covalent binding of the metal oxide, removing the metallic character of the flat Ge dimers. However, even with the opening of the band gaps, we see that the ZrO_2 and HfO_2 systems are still not equal; the HfO_2 still retains a distinct state at the 0 eV position, as it did in the non-H-passivated case, while the ZrO_2 system does not.

Analysis of the Zr and Hf PDOS plots for the H-M-O-Ge systems, shown in Figure 5.9, reveals that the H passivation greatly reduced the CB density for the metal atoms, which resulted in the opening of the semiconducting band gaps. The VB doublet peaks seen in the non-passivated PDOS (Fig. 5.7) were also coalesced into single peaks due to the H passivation. However, the anomalous Hf peak at the 0 eV position remains (see Fig. 5.9b), though it has somewhat merged with the new VB peak, causing the narrowing of the HfO_2/Ge(100) system band gap and the VB edge shoulder seen in the total DOS.

We also note that, especially for the H-passivated case, we see a similar shift in DOS minima for the M-O-Ge adsorbate systems as was observed for the O-M-Ge case. These shifts, too, may be consistent with surface band bending.

5.5 CONCLUSIONS

We have performed a survey of various transition metal dioxide (ZrO_2 and HfO_2) ordered molecular adsorbate bonding configurations on the Ge(100) surface in order to both provide some potential insight into the high-κ/Ge interface, as well as computational precursors to further calculations using thick amorphous oxide layers. The calculated enthalpies of adsorption show that bonding geometries with metal-Ge bonds (O-M-Ge) are just as thermodynamically favorable as ones with oxygen-Ge bonds (M-O-Ge), therefore a method of chemical processing may be needed to control the bonding at the interface. The calculated electronic structure results indicate that adsorbate surface bonding geometries of the form O-M-Ge tend to create a metallic (large near-E_F DOS) interface due to the metallic nature of the metal-Ge bonds, which worsens with increasing MO_2 coverage. Adsorbate surface bonding geometries of the M-O-Ge sort appear to produce much more favorable electronic structures (at least for the case of ZrO_2), including the opening of semiconducting band gaps for the H-passivated systems. Shifts in the DOS minima for both O-M-Ge and M-O-Ge adsorbate geometries are consistent with surface band bending induced by the adsorbate films, where such band bending extends much further into the Ge substrate than can be modeled by the eight layer intrinsic Ge slabs used for this computational work.
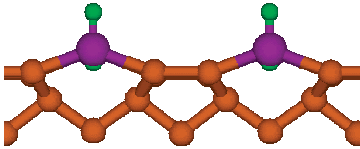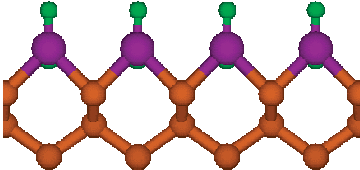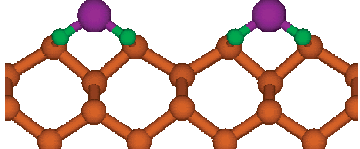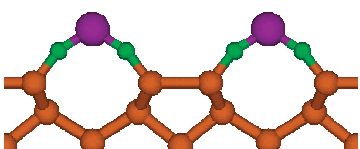
5.6 ACKNOWLEDGEMENTS

TABLE 5.1. Summary of computational results for ordered molecular adsorption of MO_2 on the Ge(100) surface, including ball-and-stick diagram and calculated enthalpies of adsorption

Identification	Geometry	$\Delta H_{ads}(ZrO_2)^a$	$\Delta H_{ads}(HfO_2)^a$
Half-Coverage O-M-Ge Adsorption		-3.16 eV	-3.63 eV
Full-Coverage O-M-Ge Adsorption		-2.78 eV	-3.29 eV
Half-Coverage M-O-Ge Displacement		-1.62 eV	-2.13 eV
Half-Coverage M-O-Ge Adsorption		-2.97 eV	-3.67 eV

a: Calculated adsorption energies, ΔHads, are given with respect to the clean Ge(100)-4×2 surface and single SiO molecules. Displacement sites are calculated with respect to the creation of Ge ad-dimers.
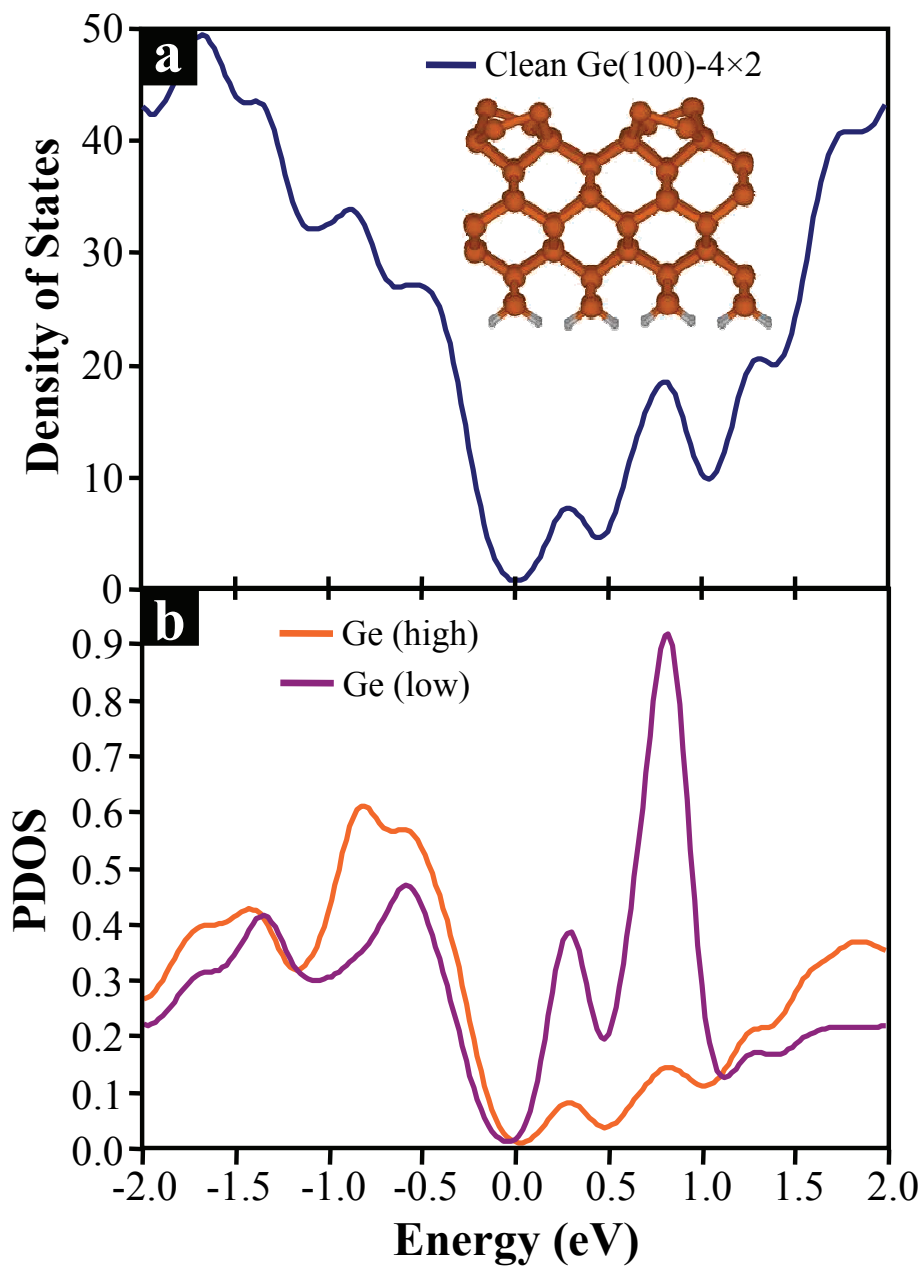
FIGURE 5.1. DFT calculated (a) density of states, DOS, and (b) projected densities of states, PDOS, for clean Ge(100)-4×2. Note the different electronic structures for the high vs. low Ge surface dimer atoms, where the sp^2-like low atom has a large empty-state (CB) density, while the sp^3-like high atom has a greater filled-state (VB) density.
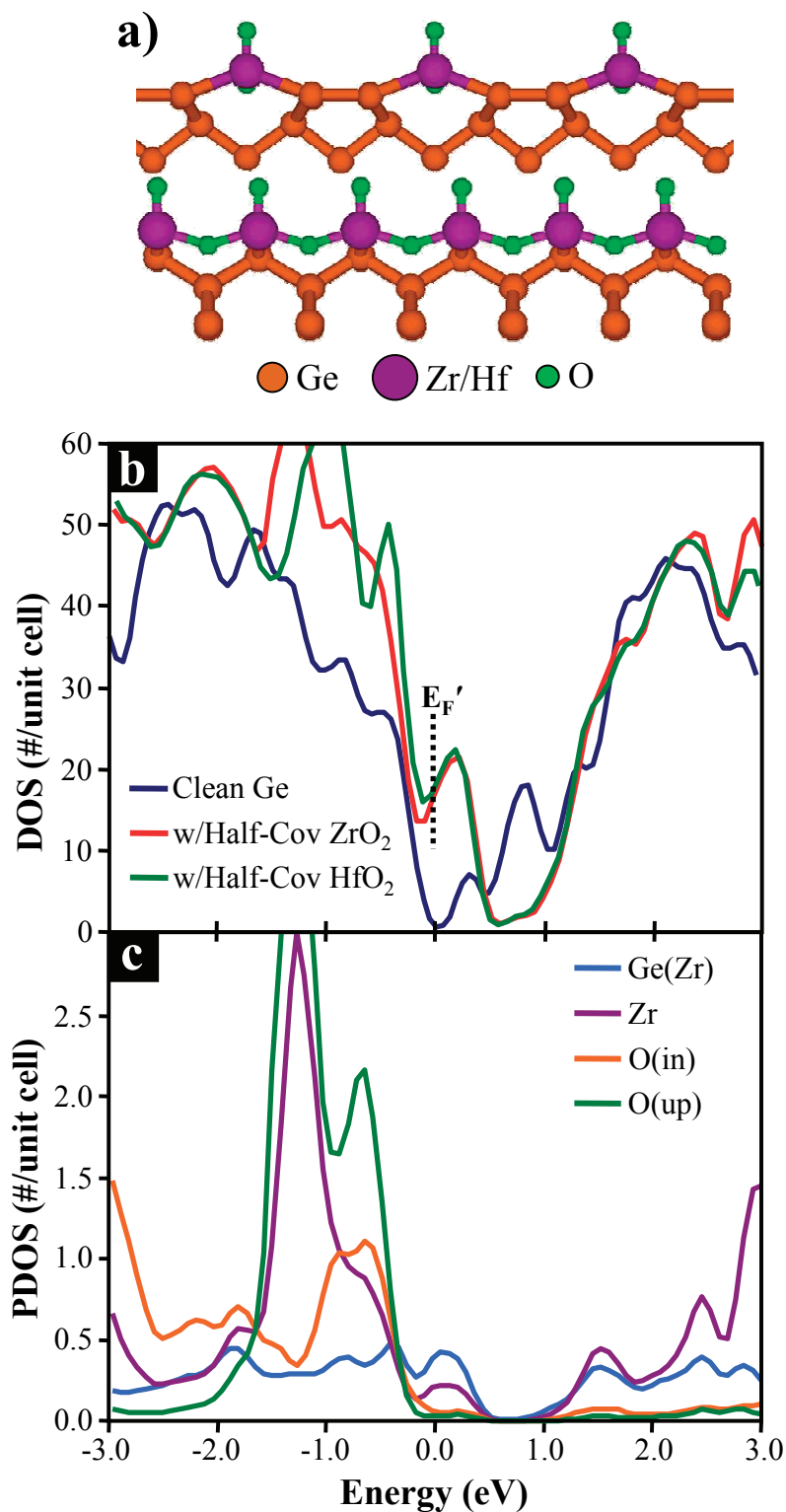
FIGURE 5.2. (a) Ball-and-stick diagrams of the half-coverage O-M-Ge geometry. (b) DFT calculated densities of states for half-coverage O-M-Ge ZrO_2 and HfO_2. (c) Projected density of states for ZrO_2 case (note: HfO_2 results nearly identical).
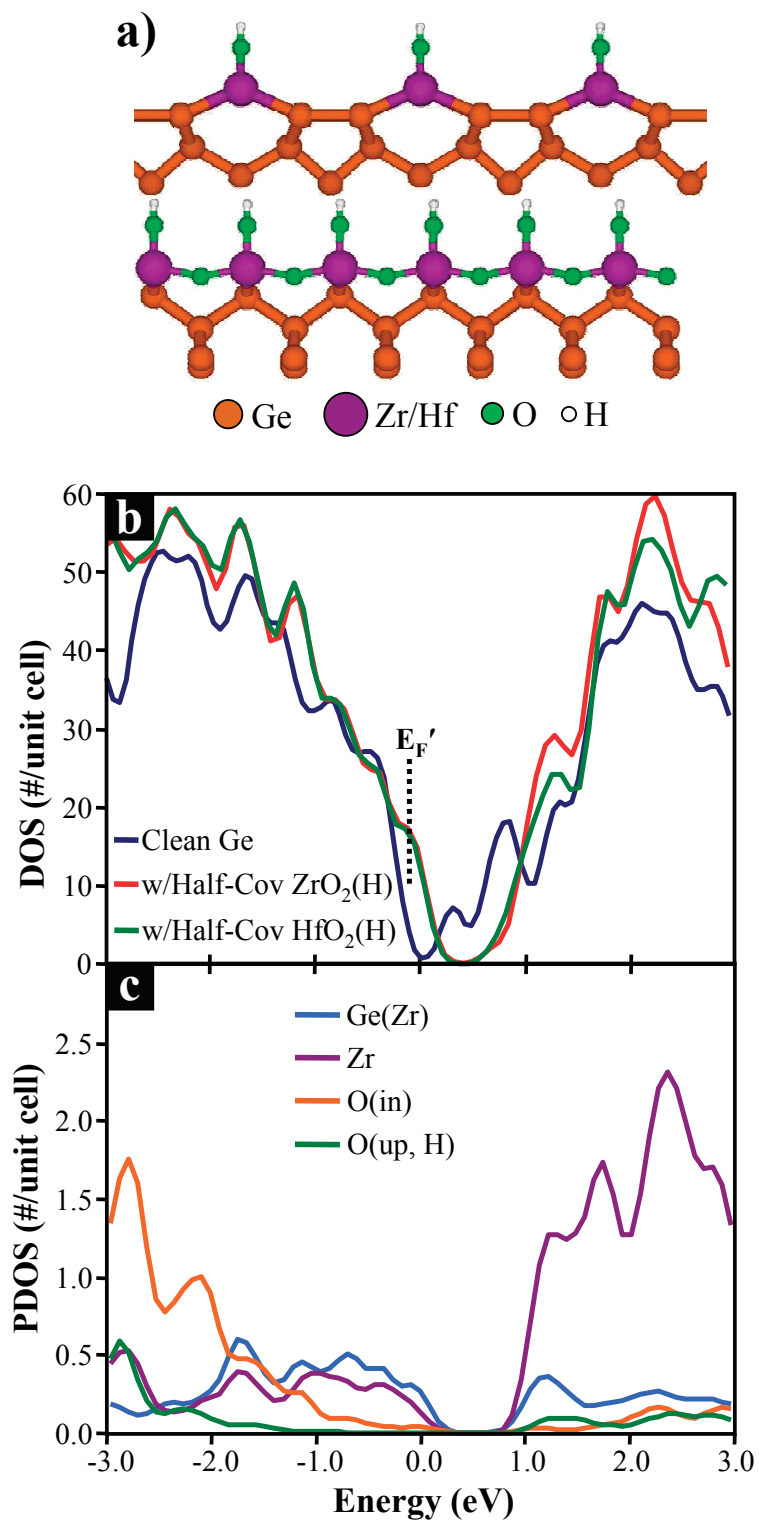
FIGURE 5.3. (a) Ball-and-stick diagrams of the half-coverage H-O-M-Ge geometry. (b) DFT calculated densities of states for half-coverage H-O-M-Ge ZrO_2 and HfO_2. (c) Projected density of states for ZrO_2 case (note: HfO_2 results nearly identical). Note the shift in DOS minima for both species.
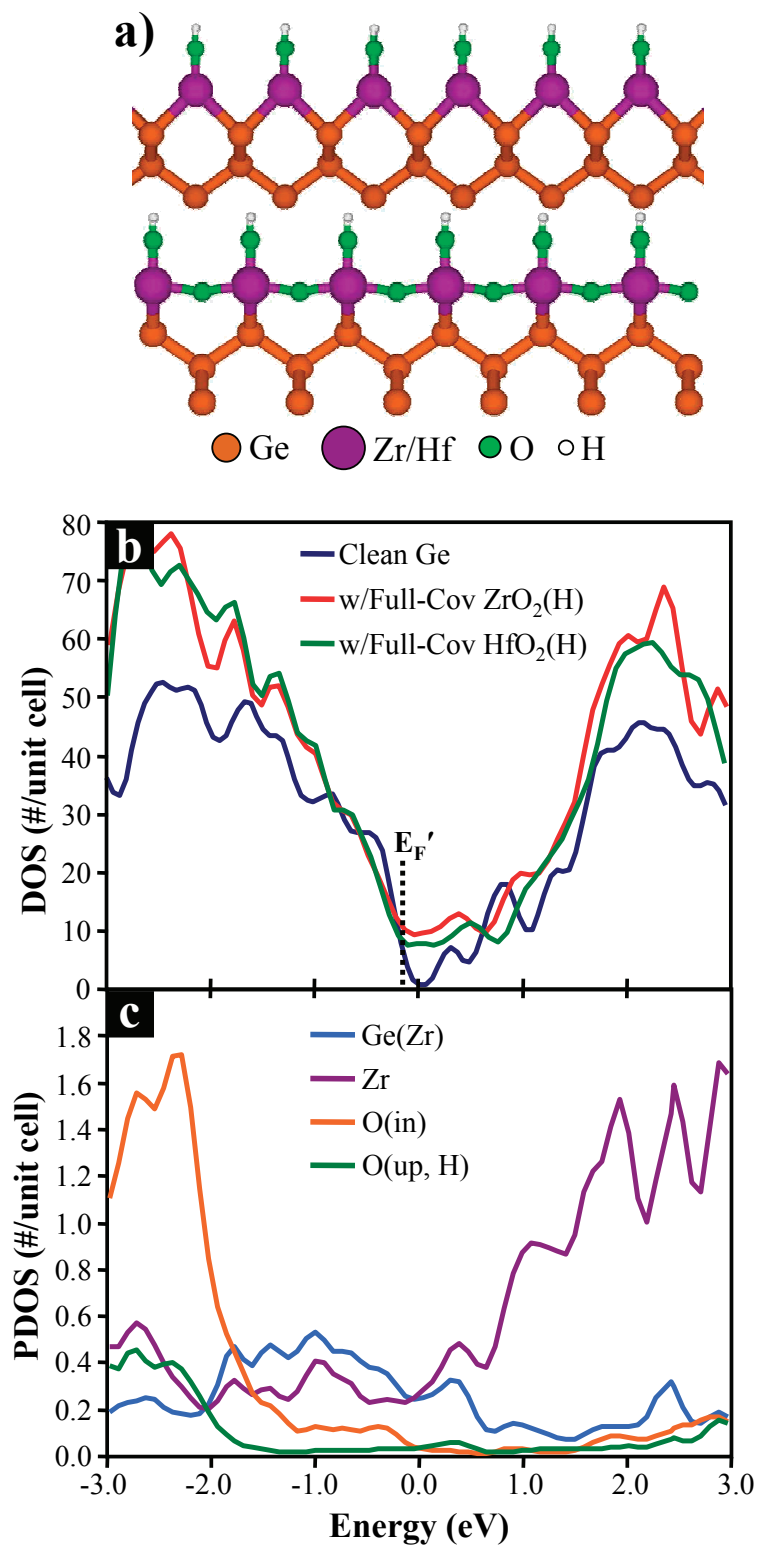
FIGURE 5.4. (a) Ball-and-stick diagrams of the full-coverage H-O-M-Ge geometry. (b) DFT calculated densities of states for full-coverage H-O-M-Ge ZrO_2 and HfO_2. (c) Projected density of states for ZrO_2 case (note: HfO_2 results nearly identical).
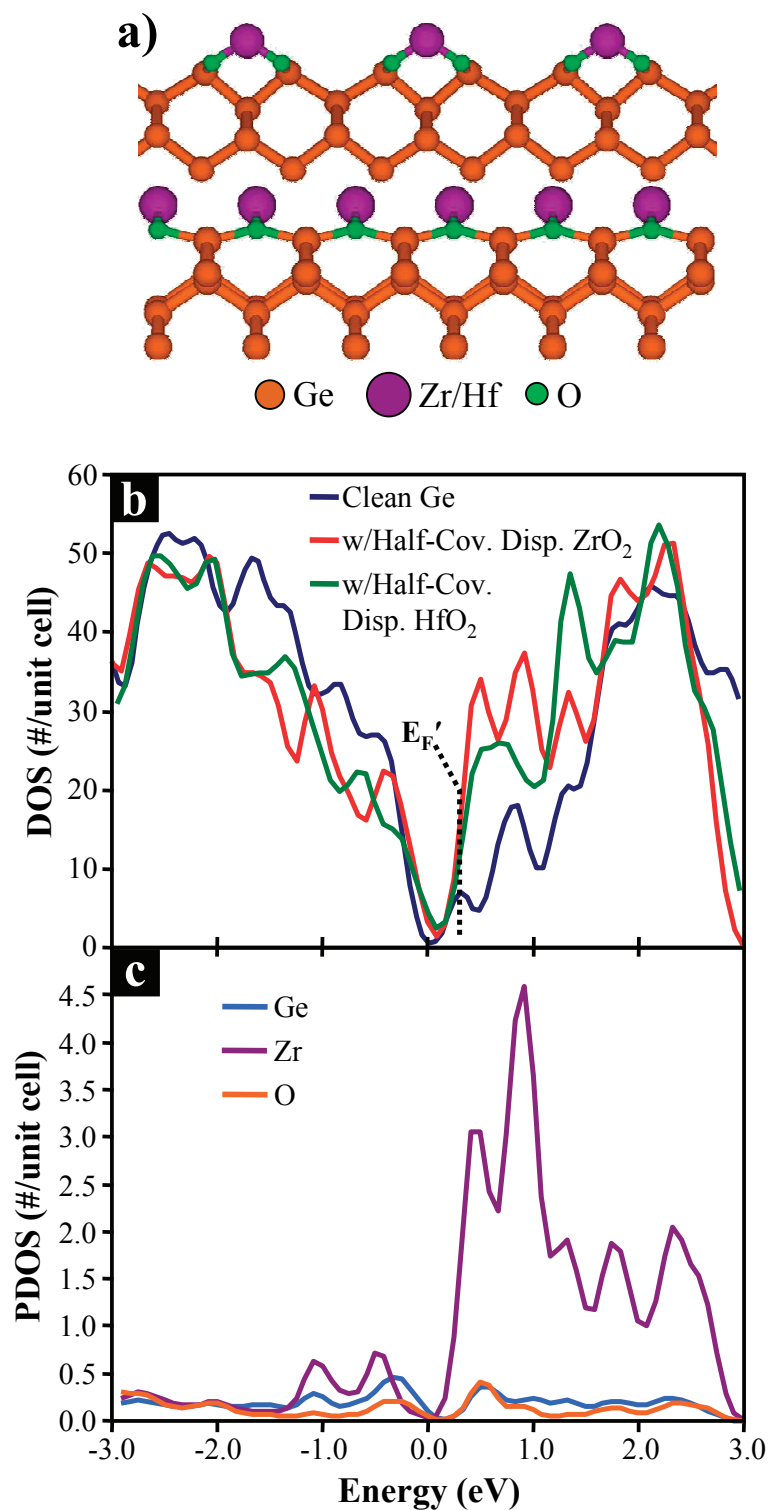
FIGURE 5.5. (a) Ball-and-stick diagrams of the half-coverage displacement-type M-O-Ge geometry. (b) DFT calculated densities of states for half-coverage displacement-type M-O-Ge ZrO_2 and HfO_2. (c) Projected density of states for ZrO_2 case (note: HfO_2 results nearly identical).
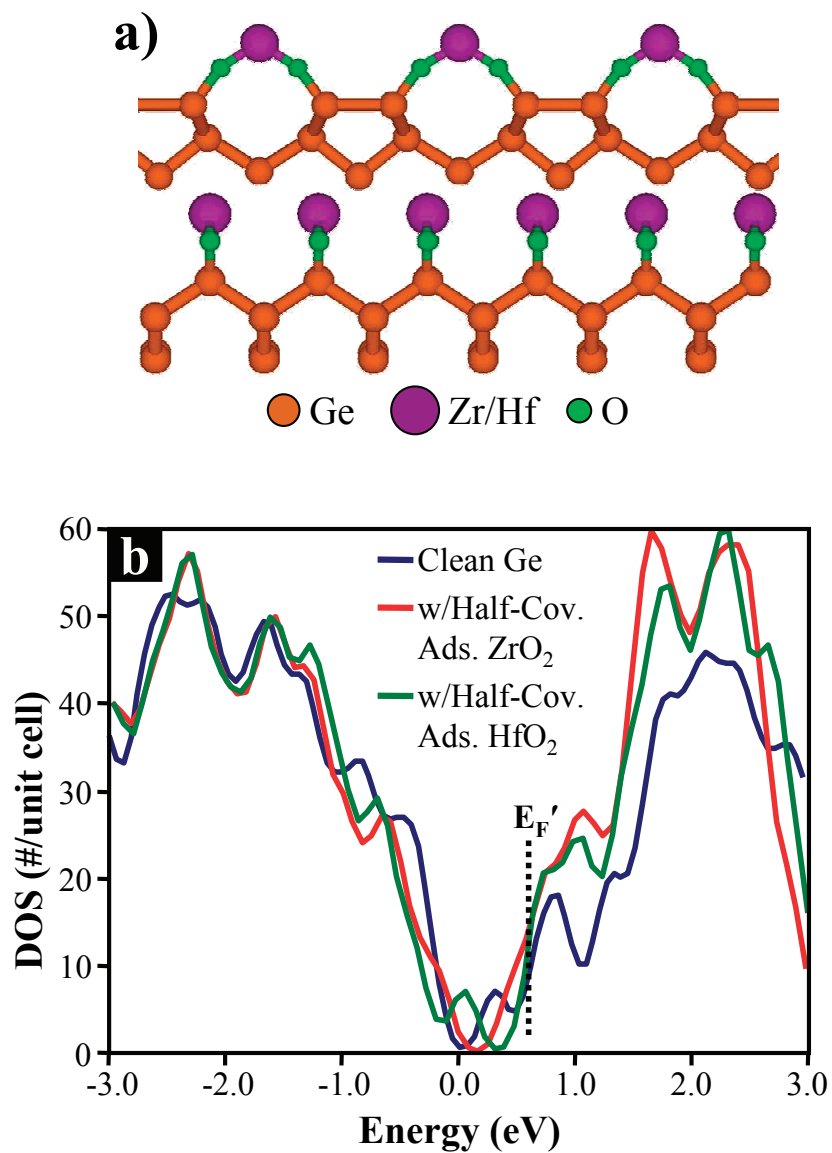
FIGURE 5.6. (a) Ball-and-stick diagrams of the half-coverage adsorbate-type M-O-Ge geometry. (b) DFT calculated densities of states for half-coverage adsorbate-type M-O-Ge ZrO_2 and HfO_2.
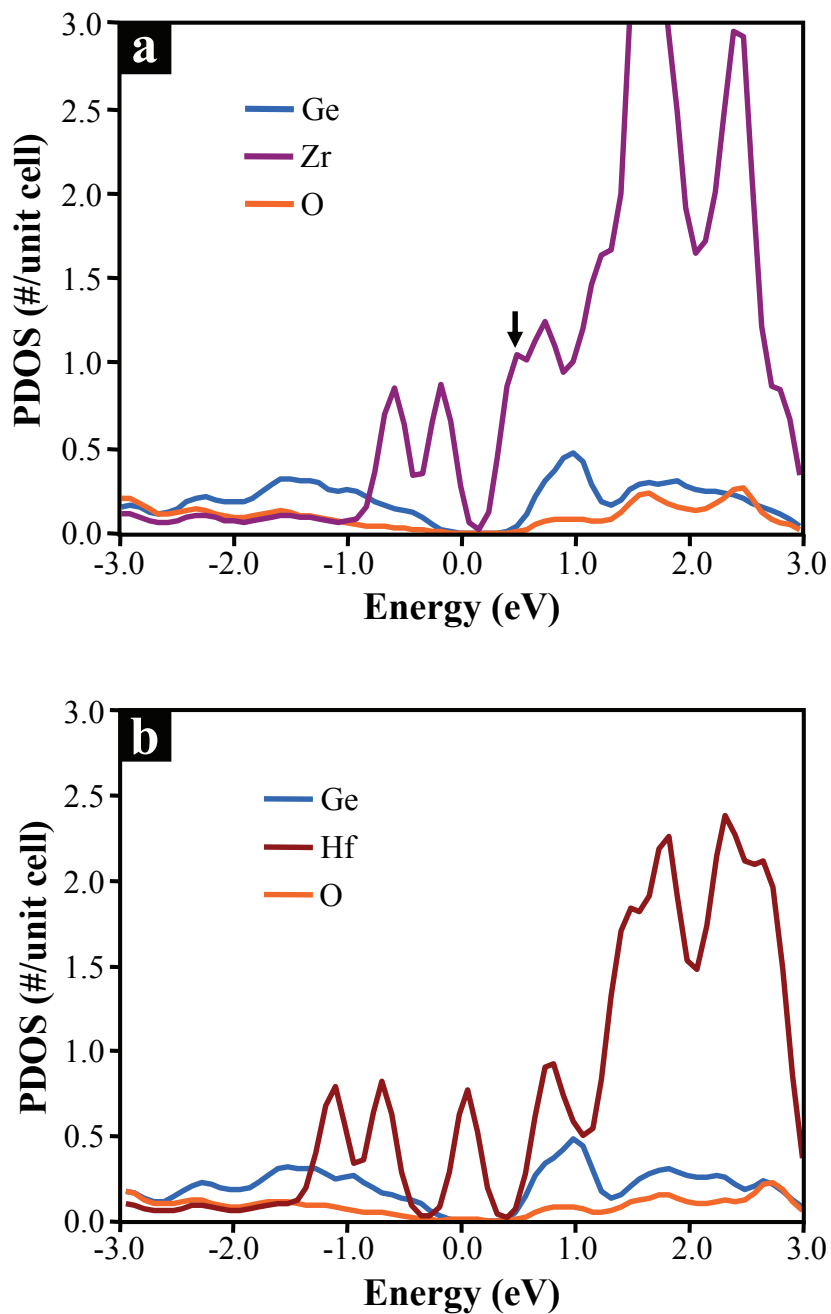
FIGURE 5.7. DFT calculated projected densities of states of the half-coverage adsorbate-type M-O-Ge geometry for (a) ZrO_2 and (b) HfO_2. The arrow in (a) points to the shoulder potentially belong to an electronic state equivalent to that found for HfO_2 at 0.0 eV.
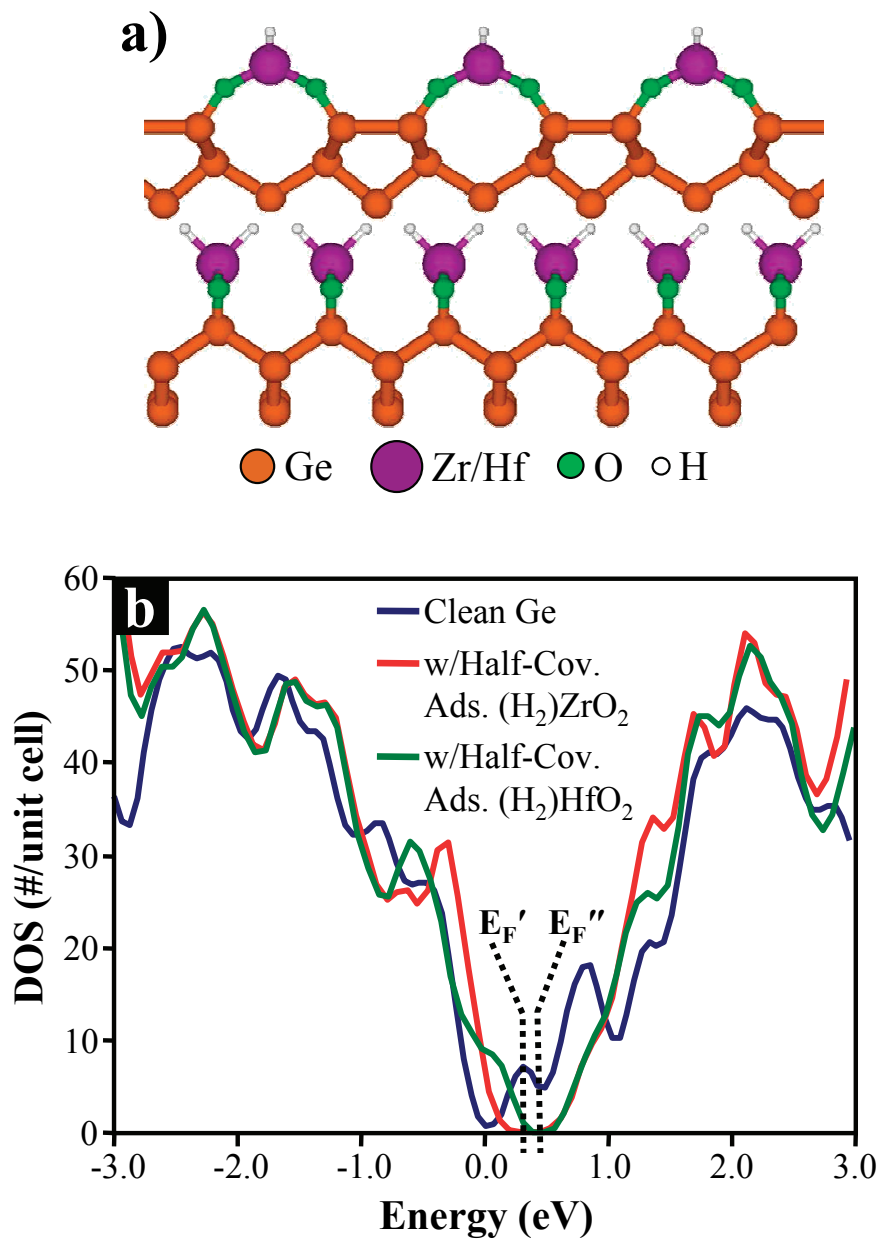
FIGURE 5.8. (a) Ball-and-stick diagrams of the half-coverage adsorbate-type H-M-O-Ge geometry. (b) DFT calculated densities of states for half-coverage adsorbate-type H-M-O-Ge ZrO_2 and HfO_2. Note the opening of the semiconducting band gap and minima shifts for both species.
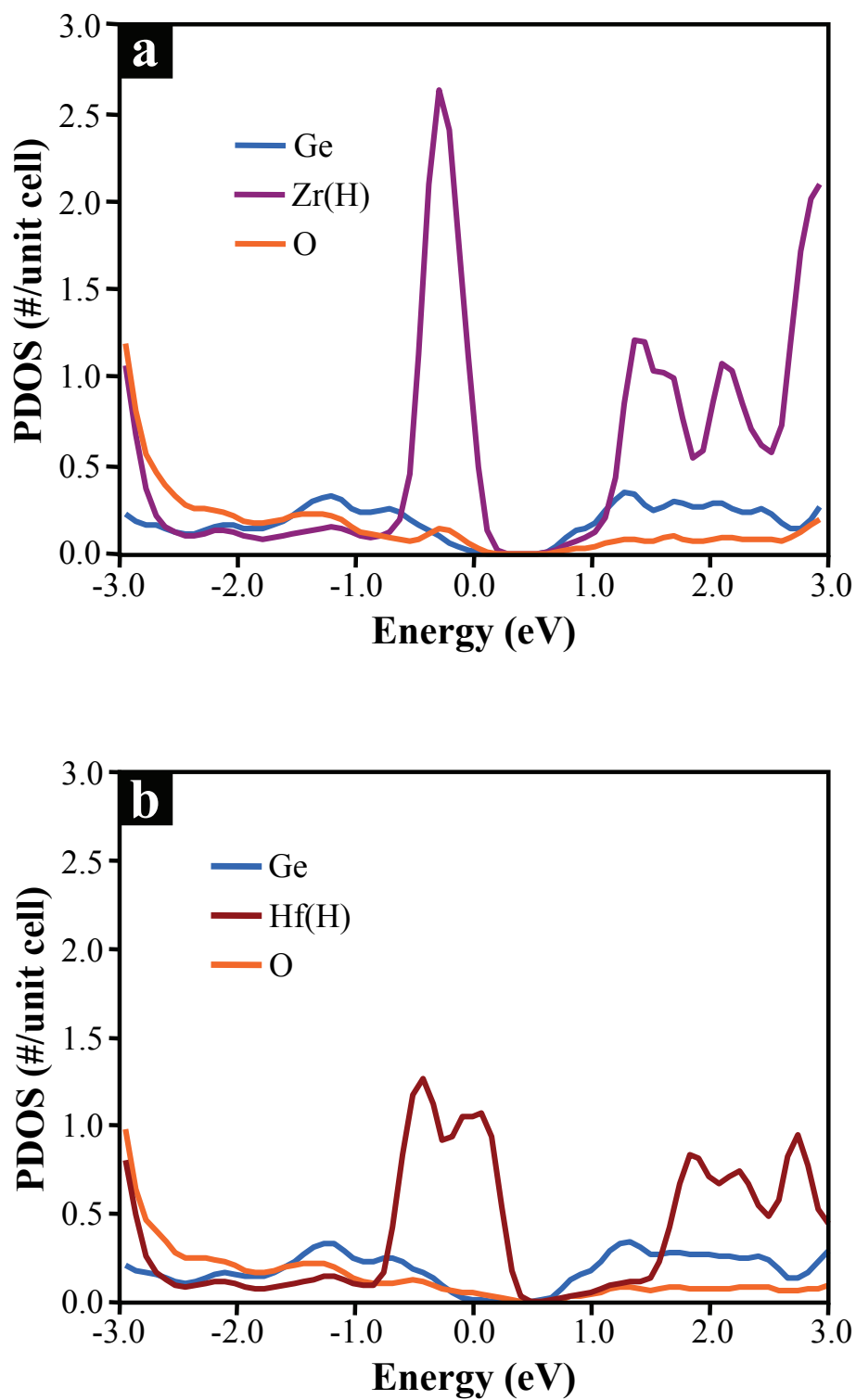
FIGURE 5.9. DFT calculated projected densities of states of the half-coverage adsorbate-type H-M-O-Ge geometry for (a) ZrO_2 and (b) HfO_2.

5.8 REFERENCES

[1] R. H. Kingston, J. Appl. Phys. **27** (2), 101 (1956).

[2] P. W. Loscutoff and S. F. Bent, Annu. Rev. Phys. Chem. **57** (1), 467 (2006).

[3] K. Prabhakaran, F. Maeda, Y. Watanabe et al., Appl. Phys. Lett. **76** (16), 2244 (2000).

[4] V. Craciun, I. W. Boyd, B. Hutton et al., Appl. Phys. Lett. **75** (9), 1261 (1999).

[5] O. J. Gregory, E. E. Crisman, L. Pruitt et al., Mater. Res. Soc. Symp. Proc. **76**, 307 (1987).

[6] Y. Wang, Y. Z. Hu, and E. A. Irene, J. Vac. Sci. Technol., A **12** (4), 1309 (1994).

[7] D. B. Alford and L. G. Meiners, J. Electrochem. Soc. **134** (4), 979 (1987).

[8] S. Huiling, H. Okorn-Schmidt, K. K. Chan et al., IEEE IEDM, 441 (2002).

[9] C. M. Ransom, T. N. Jackson, and J. F. DeGelormo, IEEE Trans. Electron Devices **38** (12), 2695 (1991).

[10] R. S. Johnson, H. Niimi, and G. Lucovsky, J. Vac. Sci. Technol., A **18** (4), 1230 (2000).

[11] M. L. Lee, C. W. Leitz, Z. Cheng et al., Appl. Phys. Lett. **79** (20), 3344 (2001).

[12] R. A. McKee, F. J. Walker, and M. F. Chisholm, Science **293** (5529), 468 (2001).

[13] M. Meuris, A. Delabie, S. Van Elshocht et al., Mat. Sci. Semicond. Proc. **8** (1-3), 203 (2005).

[14] K. C. Saraswat, C. O. Chui, T. Krishnamohan et al., Microelectron. Eng. **80**, 15 (2005).

[15] Y. Kamata, Y. Kamimuta, T. Ino et al., Jpn. J. Appl. Phys. **44** (4B), 2323 (2005).

[16] C. Chi On, H. Kim, D. Chi et al., IEEE Trans. Electr. Dev. **53** (7), 1509 (2006).

[17] G. Kresse, Thesis, Technische Universität Wien, 1993.

[18] G. Kresse and J. Furthmüller, Phys. Rev. B **54** (16), 11169 (1996).

[19] G. Kresse and J. Furthmüller, Comp. Mat. Sci. **6** (1), 15 (1996).

[20] G. Kresse and J. Hafner, Phys. Rev. B **47** (1), 558 (1993).

[21] P. E. Blöchl, Phys. Rev. B **50** (24), 17953 (1994).

[22] G. Kresse and D. Joubert, Phys. Rev. B **59** (3), 1758 (1999).

[23] J. Paier, R. Hirschl, M. Marsman et al., J. Chem. Phys. **122** (23), 234102 (2005).

[24] D. L. Winn, M. J. Hale, T. J. Grassman et al., J. Chem. Phys. **126** (8), 084703 (2007).

[25] J. P. Perdew and M. Levy, Phys. Rev. Lett. **51** (20), 1884 (1983).

[26] L. J. Sham and M. Schlüter, Phys. Rev. Lett. **51** (20), 1888 (1983).

[27] O. Gurlu, H. J. W. Zandvliet, and B. Poelsema, Phys. Rev. Lett. **93** (6), 066101 (2004).

[28] T. J. Grassman, S. R. Bishop, and A. C. Kummel, *in preparation* (2007).

CHAPTER SIX

Low Coverage Spontaneous Etching and Hyperthermal

Desorption of Aluminum Chlorides from Cl$_2$/Al(111)

6.1 ABSTRACT

Non-resonant multiphoton ionization with time-of-flight mass spectrometry has been used to monitor the desorption of aluminum chloride (Al$_x$Cl$_y$) etch products from the Al(111) surface at 100 K and 500 K during low-coverage (< 5% monolayer) monoenergetic Cl$_2$ (0.11 eV to 0.65 eV) dosing. The desorption products in this low-coverage range show predominantly hyperthermal exit velocities under all dosing conditions. For example, with 0.27 eV incident Cl$_2$, the etch product was found to have a most-probable velocity of 517 ± 22 m/s at an Al(111) surface temperature of 100 K. This corresponds to 22 times the expected thermal desorption translational energy for AlCl$_3$. Cl$_2$ sticking probability measurements and Al$_x$Cl$_y$ etch rate measurements show etching even at Cl$_2$ coverages of less than 5% monolayer at surface temperatures between 100 K and 500 K. These experimental results are consistent with a combination of fast-time-scale surface diffusion and agglomeration of the adsorbed chlorine to form aluminum chlorides and the presence of activated AlCl$_3$ chemisorption states having potential energies above the vacuum level. Density functional theory calculations yield results that are consistent with both our experimental findings and mechanistic descriptions.

6.2 INTRODUCTION

The mechanism of Cl_2 adsorption onto aluminum, and subsequent etching by thermal aluminum chloride desorption, has been studied many times in the last quarter century.[1-13] Most of the work has focused on Cl_2 plasma etching for integrated circuit processing of aluminum films. Because plasma etching environments are typically very complex, the problem is usually broken down into much simpler components, including the dry etching of Al by Cl_2. Etch rate and etch product studies utilizing a variety of techniques, including (but not limited to) quadrupole[1-3] and time-of-flight mass spectrometry,[5] gas-phase titration of chlorine atoms,[6] quartz-crystal microbalance,[2,4] *in situ* Fourier transform infrared spectroscopy,[7] Auger electron spectroscopy,[4,10-12] and x-ray photoelectron spectroscopy[1,4] have been performed at pressures ranging from UHV to near-atmospheric. Kinetic modeling has also been employed to characterize the processes involved in both the thermal and ion-assisted etching of Al(111) by Cl_2.[9]

Spontaneous high-rate thermal etching of Al by Cl_2 has been reported by several investigators at high surface coverages (monolayer or greater).[1-10] These reports state that at least monolayer coverages of chlorine are necessary for the initiation of thermal desorption of aluminum chloride etch products. Presumably this high chlorine coverage allows for subsurface absorption of Cl adsorbates to occur such that the surface Al atoms are more stoichiometrically surrounded by Cl atoms.[11] These stoichiometric aluminum chlorides are then said to thermally desorb into the gas phase, with a barrier to desorption equal to about room temperature. This thermal etching is reported to be quenched below room temperature;[6] while ion-assisted etching has been observed at -50ºC in electron

cyclotron resonance (ECR) plasmas.[9] These proposed high-coverage adsorption and etching mechanisms reproduce the experimental high-coverage data reasonably well.

Conversely, we observe not only that etching of Al(111) by Cl_2 can occur at very low surface coverages (< 5% monolayer), but that these etch products actually exit the surface at hyperthermal velocities which correspond to $2 - 30$ times thermal energy. Remarkably, these effects are independent of both surface temperature (experiments were performed at both 100 K and 500 K) and Cl_2 translational energy (0.11 eV, 0.27 eV, and 0.65 eV Cl_2 incident energies were studied). Time-of-flight mass spectrometry of aluminum chloride desorption products, Cl_2 sticking probability measurements, and etch rate profiling experiments (etch rate vs. Cl_2 exposure time) all clearly indicate a low-coverage hyperthermal etching behavior that has not yet been reported. Computational DFT modeling of the Cl_2/Al(111) gas-surface reaction sequence has also been performed to further characterize the mechanism behind this etching phenomenon. We have thus developed a mechanistic model to account for both the occurrence of the low-coverage etching and the hyperthermicity of the desorbed etch products. We hypothesize that the ultra low-coverage etch results from reactions of Cl adsorbates with exposed, and therefore more reactive, Al surface defect-type sites such as adatoms, regrowth islands, and step edges. It is at these special sites, then, that the subsequently formed aluminum chloride reaction product is able to exist in a slightly energized or excited state, specifically an activated chemisorption state, with a potential energy above that of the vacuum level. Thereafter, desorption produces etch products that exit the surface with translational energies greater than that of thermal energy.

6.3 METHODS

A. Experimental Setup

All experiments were performed under ultra-high vacuum (UHV) conditions, with a base chamber pressure of 2×10^{-10} Torr. The UHV chamber used for these studies has been previously described in detail elsewhere.[14-17, 20] Experiments were performed on an aluminum single crystal (Monocrystals Company, 99.999+% purity, 10 mm diameter $\times$ 2 mm thickness) with a (111) surface orientation. The aluminum surface was cleaned by sputtering with normal incidence 2 kV Ar^+ ions; this was followed by a two minute high temperature anneal (500 ºC) to reduce sputter damage. Surface purity and order were then checked by Auger electron spectroscopy (AES) and low-energy electron diffraction (LEED).

Aluminum chloride desorption experiments were performed in conjunction with Cl_2/Al(111) abstractive chemisorption measurements.[18] A mechanically chopped (7 µs chopper open time), 10 Hz pulsed molecular beam (General Valve, model #9-400-900, 2 mm orifice) of Cl_2 seeded in different noble gases was used to dose the aluminum surface at three different Cl_2 incident energies: pure Cl_2 at 0.11 ± 0.01 eV, 5% Cl_2/Ne at 0.27 ± 0.01 eV, and 5.32% Cl_2/He at 0.65 ± 0.02 eV. (Note that all values reported in this paper, where applicable, are given with standard errors, rather than standard deviations, because the reported numbers are mean values of numerous experiments.) All related etching experiments were performed with the molecular beam at normal incidence to the surface, and products were detected just off-normal (~ 9º off of the surface perpendicular) in an effort to avoid interference from the incident beam.

All gases were purchased premixed from Matheson Tri-Gas, and no other halogen contaminants were detected by QMS. The average beam fluxes – as calculated via half surface coverage times from sticking data, and using a simple $1-\theta$ sticking coefficient dependence – were found to be as follows: 3.0×10^{13} molecules cm^{-2} sec^{-1} for pure Cl_2, 2.6×10^{13} molecules cm^{-2} sec^{-1} for Cl_2/Ne, and 1.0×10^{13} molecules cm^{-2} sec^{-1} for Cl_2/He. All three molecular beam varieties gave an increase in background pressure of no more than 2×10^{-11} Torr when introduced into the main UHV chamber.

The aluminum chloride desorption products were detected via nonresonant multiphoton ionization (MPI) and subsequent time-of-flight mass spectrometry (TOF-MS). A pulsed UV laser was optimized for resonant multiphoton ionization (REMPI) of neutral chlorine atoms, but also provided sufficient fluence for both the dissociation of the aluminum chloride desorption products and a strong nonresonant aluminum MPI signal, as described by Equations 6.1 and 6.2.
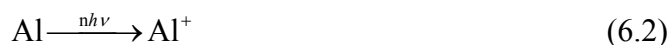
$$Al_xCl_y \xrightarrow{\ nh\nu\ } xAl + yCl \qquad\qquad (6.1)$$

$$Al \xrightarrow{\ nh\nu\ } Al^+ \qquad\qquad (6.2)$$

The laser light was prepared by using the frequency-doubled fundamental from a Q-switched Nd:YAG laser (Continuum, 581C-SF; 532 nm, 10 Hz, 7 ns pulse width) to pump a tunable dye laser (Lambda-Physik, FL 3002) running DCM/methanol, tuned to 630.6 nm. The dye laser output was frequency-doubled with a KDP-C crystal housed in a wavelength-tracking package (Inrad, UV Autotracker III). This doubled light was then

added to the remaining dye laser fundamental (via a BBO crystal in an identical Autotracker box) to produce a final output of 210.2 nm, with average pulse energy of 1.5 mJ, pulse widths of 7 ns, and a rate of 10 Hz.

Experiments were performed at aluminum surface temperatures of both 100 K and 500 K. The TOF detection method was used to probe incident and scattered species (Cl_2), as well as abstraction (Cl) and desorption (Al_xCl_y) products. Sticking probability measurements were performed using both the standard King and Wells type reflection technique[18,19] and the previously discussed transient peak-to-peak method.[20] The transient peak-to-peak technique uses a slow-pulsed (2 Hz) beam to accommodate for the fast chamber wall pumping[21] in between each pulse, giving a more reliable baseline, whereas the reflection technique uses a fast-pulsed (60 Hz) beam whose baseline is strongly affected by chamber wall pumping. The individual resultant signal peaks are used as data points, giving a more accurate initial sticking probability measurement for reactive systems that are sometimes difficult to measure using the standard reflection technique.

B. Computational Details

All density functional theory (DFT) calculations presented in this paper were performed using the Vienna Ab-Initio Simulation Package (VASP)[22-25] in the generalized gradient approximation (GGA, PW91), with ultra-soft Vanderbilt pseudopotentials[26,27] (as supplied with the VASP program), a 5×4×1 Monkhorst-Pack k-point mesh generation scheme (for a total of 10 irreducible k-points), and plane-wave basis kinetic energy cut-off of 350 eV. All parameters (i.e. k-points, cut-off energy, vacuum space, etc.) were

chosen such that they were each individually converged to within 1 meV/atom for the $Cl_{2(g)}/Cl_{(ad)}/Al(111)$ system of study. These calculations should provide good relative accuracy, with an estimated relative error 0.1 eV. Regardless of absolute numerical accuracy, the qualitative results from these calculations should be quite reasonable because we are making comparisons both between different bonding geometries and between relative energies which have all been calculated under identical conditions and with similar types of bonds.

The system studied consisted of an Al(111) surface slab supercell which is repeated in all directions. The aluminum slab was 4 atomic layers thick, with each layer being 4×5 atoms in area, for a total of 80 Al atoms per unit cell (81 for the adatom calculations). The supercell also contained 10 atomic layers of vacuum space (18 Å) in the z-direction. The bottom two aluminum layers were constrained to the minimum-energy bulk geometry, which was found through a series of bulk Al calculations that yielded an Al nearest-neighbor distance of 2.86 Å (equal to the experimentally observed value). All other atoms (substrate, adsorbate, gas-phase) were allowed to structurally relax without constraint.

6.4 RESULTS

Experimental identification of the aluminum chloride etch products was not possible with our instrumental setup. The high energy, high fluence photons used during the experiments were too powerful to leave a detectable amount of large-mass fragments behind (but were necessary for a sufficiently measurable Al MPI signal). Therefore, we

are left to rely upon both indirect evidence from our own data and the experimental results of several other groups for aid in the identification of the aluminum chloride etch products. All applicable published results for the etching of aluminum by Cl_2 (References 1-9 in particular) were consulted as to their assignment of the major desorption products for this reaction; their reasons for doing so were also taken under consideration. Unfortunately, unlike the results presented in this paper, none of the published studies were performed under ultra-low Cl_2 coverage conditions, nor were any of the experiments performed at surface temperatures below -50 ºC (~220 K). The most similar experimental conditions found in the literature were those presented by van Veen et al.,[5] who performed molecular beam Cl_2 dosing and TOF-MS detection of thermal etch products from Al(111). The molecular beam flux used for their experiments (7×10^{16} molecules cm^{-2} sec^{-1}), however, was over three orders of magnitude larger than that used in our experiments.

With this in mind, the major etch products for the etching reaction of Cl_2 on Al(111) reported by van Veen et al. are as follows: Al_2Cl_6 at temperatures below 450 K, $AlCl_3$ between 500 K and 650 K (also reported by Winters[3]), and AlCl above 700 K. These assignments are generally agreed upon within the bulk of the literature, but with somewhat varying temperature ranges reported across groups. It must also be noted that at the comparatively large pressures under which some of these studies were performed, gas-phase reactions – most importantly the aluminum chloride dimerization reaction, $2AlCl_3 \leftrightarrow Al_2Cl_6$ – may play a role in the identity of the final detected etch product. Cleland and Hess[7] showed that at a gas temperature of 500 K, pressures below 1×10^{-5} Torr are required to produce a mean free path long enough that the aluminum chloride

desorbates are unlikely to undergo significant intermolecular collisions. Under these conditions, one does not need to account for dimerization because the equilibrium is driven all the way to the left, preventing the formation of Al_2Cl_6. We thus assume that the etch product at 500 K is $AlCl_3$ and at 100 K is either $AlCl_3$ or Al_2Cl_6. This issue will be discussed in more detail later in the paper.

A. Hyperthermal Aluminum Chloride Exit Velocities

Time-of-flight spectra of the neutral desorbing aluminum chloride etch products were recorded to determine their exit velocities. This was accomplished by successively increasing the delay between the molecular beam chopper open time and the laser fire trigger by small, successive increments (typically around 2-5 μs per increment). The velocities of the incident Cl_2 molecular beams were measured with a UTI 100C quadrupole mass spectrometer and were checked daily by laser TOF-MS. These checks were performed both to verify that the incident velocities were consistent with the QMS values and to ensure that the arrival times of the incident Cl_2 at the surface were consistent between experiments. Figure 6.1 presents a typical TOF distribution of each of the incident Cl_2 beams – (a) Cl_2/He, (b) Cl_2/Ne, and (c) pure Cl_2 – with the velocities, translational energies, and widths given in the table in part (d). The incident Cl_2 arrival time upon the Al(111) surface, t_0, was calculated using both the most-probable velocity of the incident molecular beam, $v_{p,inc}$, from the QMS measurements and the measured distance between the laser ionization volume and the aluminum surface, $d_{ls,inc}$, such that

$$t_0 = \frac{d_{ls,inc}}{v_{p,inc}}.$$ (6.3)

This value was then subtracted from the Al$^+$ TOF spectra in order to provide a zero time for the etch product time-of-flights.

Attempts to fit the time-of-flight data to the commonly used modified Maxwell-Boltzmann distribution form[28,29]

$$f(v) \propto v^3 \exp\left[-\left(\frac{v - v_0}{\alpha}\right)^2\right],$$ (6.4)

where v_0 is the so-called stream velocity and $\alpha = \sqrt{2kT_{eff}/m}$ is a term describing the width of the distribution via an effective temperature, T_{eff}, yielded very soft, low-correlation fits with large negative stream velocities and large effective temperatures. Such results are not particularly useful, as they only indicate a Boltzmann-like velocity distribution that is wider than a thermal distribution for that particular mean velocity and do not provide any actual numerical information. Therefore, the method described below was used to extract the needed information from the time-of-flight data. Additionally, because the widths of the etch product distributions were found to be 4 to 10 times wider than the incident Cl_2 molecular beam distributions (see Figure 6.1), deconvolution of the time-of-flight distributions was not deemed necessary, as the difference between the raw and deconvoluted distributions are negligible.

From the aluminum chloride etch TOF spectra, the most-probable exit velocities (v_p, Equation 6.4) were extracted using the following relationship:

$$v_p = \frac{d_{sl}}{t_p}, \tag{6.5}$$

where d_{sl} (= 12.5-16.0 mm) is the distance from the surface to the laser focus and t_p is the most-probable time of flight, or the value at the peak detected ion intensity, taken from the TOF spectra. From this data, and with the known etch product masses (References 1-9), the exit kinetic energies can be calculated. These values are then compared to the expected most-probable thermal desorption translational energies, E_p, for the surface temperatures of interest. E_p is calculated from the expected most-probable time of flights from a general flux-weighted Maxwell-Boltzmann time-of-flight distribution using a density detector (as is the case with this detection method):[29]

$$S(t) \propto \frac{1}{t^4} \exp\left(-\frac{md_{sl}^2}{2kT}\frac{1}{t^2}\right) \quad \Rightarrow \quad \frac{\partial S(t)}{\partial t} = 0 \quad \Rightarrow \quad t_p = \frac{d_{sl}}{2}\sqrt{\frac{m}{kT}}, \tag{6.6}$$

$$v_p = \frac{d_{sl}}{t_p} = 2\sqrt{\frac{kT}{m}}, \tag{6.7}$$

$$E_p = \frac{1}{2}mv_p^2 = 2kT, \tag{6.8}$$

where m is the desorption product mass, k is the Boltzmann constant, T is the surface temperature, and t is time of flight; t_p is the most-probable (or peak) time of flight of the distribution, v_p is the most-probable velocity of the distribution, and E_p is the most-probable translational energy of the distribution. In addition, the widths of the measured

distributions can be analyzed and compared with the values that would be expected for a thermal distribution. A true flux-weighted Maxwell-Boltzmann thermal distribution of the form given in Equation 6.6 exhibits a most-probable velocity to full-width half-max ratio (v_p:w) of about 1, and deviation from this expected ratio is an indication of non-thermal desorption phenomena; a ratio smaller than unity indicates a wider distribution than would be expected for a purely thermal desorption mechanism. All relevant data from the time-of-flight experiments is given in Table 6.1. Two typical raw TOF Al^+ spectra for the 0.27 eV Cl_2 incident beam are shown in Figure 6.2, along with thermal distributions for the probable etch products.

1. Low Surface Temperature Desorption

Due to the high sensitivity of the MPI detection scheme, even at low surface temperatures (100 K), very low Cl_2 flux ($1.4 \times 10^{13} - 4.2 \times 10^{13}$ molecules cm^{-2} sec^{-1}), and very low surface Cl_2 coverage (< 5% monolayer), we are able to observe the small amount of aluminum chloride etch product that results from the gas/surface reaction between Cl_2 and the Al(111) surface. In addition, we find that these etch products desorb from the Al(111) surface with hyperthermal translational exit velocities/energies upon dosing with all incident Cl_2 energies studied. In an effort to consider all reasonable possibilities for etch product identification, as well as to establish both an upper and a lower bound to our measured translational exit energy results at 100 K, we shall compare the kinetic energies of the desorption products assigned as both $AlCl_3$ (lower bound) and Al_2Cl_6 (upper bound).

Figure 6.3 displays the results of the 100 K Al(111) surface temperature etch

product desorption time-of-flight experiments, as both exit velocity vs. incident Cl_2 velocity (Figure 6.3a) and exit translational energy vs. incident Cl_2 translational energy (Figure 6.3b). The velocity-space graph (1.3a) compares the experimentally observed exit velocities with the expected thermal exit velocities for the two possible etch products, $AlCl_3$ and Al_2Cl_6. The energy-space graph (1.3b) compares the exit translational energies of the possible etch products (as calculated from the experimental exit velocities) with the expected exit energies from thermal desorption. Exit velocities are also plotted vs. both 100 K and 500 K Al(111) surface temperatures in Figure 6.4.

The desorption products from the reaction at 100 K with the lowest incident translational energy Cl_2 (pure Cl_2, 535 m/s, 0.11 eV) were found to have the slowest mono-modal exit velocity (465 ± 28 m/s). Assuming that the etch product for this system is $AlCl_3$, the measured kinetic energy is 0.14 ± 0.01 eV, or 8 times that of 100 K thermal energy (0.017 eV). If we assume that the etch product is Al_2Cl_6, the measured kinetic energy is 0.32 ± 0.04 eV, or 19 times that of the expected thermal exit energy. The 100 K surface temperature 0.11 eV Cl_2 data exhibits a most-probable velocity-to-width ratio (v_p:w) of 0.69, consistent with a non-thermal distribution. The etch product mean velocity and the most-probable velocity-to-width ratio (v_p:w) for etching by Ne-seeded incident Cl_2 (850 m/s, 0.27 eV) were similar to those from 0.11 eV pure Cl_2.

The etch products from the reaction with the highest incident translational energy Cl_2 (Cl_2/He, 1327 m/s, 0.65 eV) at 100 K were found to be bimodal, with peak velocities of 255 ± 9 m/s and 612 ± 21 m/s. As shown in Figure 6.5, during the first ~10 seconds of dosing with 0.65 eV Cl_2 on a fresh, clean Al(111) surface, the etch products were found to have the faster exit velocity (solid curve, open circles). After the initial 10 second

clean etch, the peak velocity switches to the lower value (dashed curve, open squares) and remains at this value until surface saturation. Both velocity modes, however, show hyperthermal exit energies. Assuming that the thermal etch product at 100 K is $AlCl_3$, the measured kinetic energy of the slow mode (from the Cl_2 pre-exposed surface) was 0.05 ± 0.01 eV, 3 times that of thermal energy, while the fast mode (from the fresh, clean surface) was 0.22 ± 0.03 eV, 13 times that of thermal. Assuming that the etch product is Al_2Cl_6 results in a measured kinetic energy for the slow mode of 0.09 ± 0.01 eV, 5 times that of thermal, and a fast mode of 0.52 ± 0.04 eV, 31 times greater than thermal energy. The 100 K surface temperature 0.65 eV incident Cl_2 data exhibited a slow-mode v_p:w ratio of 0.65, and a fast-mode ratio of 0.84.

2. High Surface Temperature Desorption

For high surface temperature (500 K), the measured exit velocities/energies of the etch products were not as dramatically larger than thermal as was observed in the cold surface temperature experiments, but were hyperthermal nonetheless (see Figure 6.6 and Table 6.1). In this case, all relevant reported experimental data by other research groups identify $AlCl_3$ as the definite etch product at 500 K.[2,3,5,6] As such, we are confident to designate this species as that which we detected in the 500 K experiments. The calculated exit translational energies are shown in Figure 6.6b and given numerically in Table 6.1.

The most dramatic difference observed at 500 K surface temperature was that the 0.65 eV Cl_2 produced a monomodal etch product velocity distribution instead of the bimodal distribution that was observed at 100 K. At 500 K surface temperature and 0.65

eV incident Cl_2, the measured most-probable velocity was 653 ± 16 m/s. This data exhibits a v_p:w ratio of 0.56, making it the most non-thermal distribution measured. It is possible that the slow etch product observed at 100 K surface temperature and high coverage for 0.65 eV Cl_2 is due to collision induced desorption and is absent at high surface temperature because no adsorbates remain on the surface at 500 K.

Upon comparing the etch product mean velocities at surface temperatures of 100 K and 500 K, two major trends are observed. First, as the incident translational velocity is increased by an overall factor of 2.5, the etch product velocity increases by only 22% to 33%, with the effect being largest at 100 K surface temperature. Second, as the surface temperature is increased by a factor of 5, the etch product exit velocity increases by only 6.7% to 15%, with the effect being largest for the lowest incident energy Cl_2. These trends indicate that there is very little, if any, temperature dependence upon the mechanism of etch product formation and desorption. The weak dependence upon incident Cl_2 velocity/energy is consistent with the existence of two distinct mechanisms for the reaction of Cl_2 with the Al(111) surface – direct activated chemisorption at high incident energy and precursor mediated chemisorption at low incident kinetic energy – as described recently.[20] It is reasonable that the different chemisorption mechanisms would produce etch products with slightly different mean velocities. The small amount of excess energy from the direct chemisorption mechanism (high-energy Cl^- adsorbing onto the surface) may add slightly to the overall reaction energetics, consistent with the weak dependence upon Cl_2 incident energy observed for the aluminum chloride exit energies.

B. Cl$_2$ on Al(111) Sticking Probabilities

Sticking probability measurements were performed via both the standard King and Wells reflection technique[18-19] and by a transient peak-to-peak method recently discussed by our group.[20] Both techniques used a quadrupole mass spectrometer (QMS) set for mass 35 as the scattered chlorine detector. The King and Wells and the transient peak-to-peak methods utilize relatively high (60 Hz pulse rate) and low (2 Hz pulse rate) Cl$_2$ fluxes, respectively, compared to the normal conditions of the time-of-flight experiments. The peak-to-peak method exhibits considerably more sensitivity with respect to initial low-coverage sticking measurements because it can overcome the problems of high flux and chamber wall pumping.[21]

1. Low Surface Temperature Sticking Curves

Figure 6.7a displays a typical 100 K Al(111) surface temperature King and Wells-type sticking curve for dosing with a 0.11 eV Cl$_2$ molecular beam, and Figure 6.7b displays the sticking curve for dosing with a 0.65 eV Cl$_2$ beam. The 100 K surface temperature sticking curves from both types of sticking experiments demonstrate the basic expected behavior for a reactive system with reasonably high initial sticking probability for all three Cl$_2$ incident energies (0.11 eV, 0.27 eV, and 0.65 eV). However, the King and Wells technique was found to give artificially low initial sticking probabilities because of the high Cl$_2$ fluxes and fast pumping by the chamber walls.[21] Upon exposure to the Cl$_2$ dose beam, a large (> 65%) initial sticking probability is observed, followed by eventual saturation coverage. The 0.11 eV Cl$_2$ beam gives the highest initial sticking probability (90%), while the higher-energy 0.27 eV and 0.65 eV

Cl_2 beams show slightly lower (80% and 65%, respectively) initial sticking probabilities. The 0.65 eV Cl_2 sticking curve was found to not reach complete saturation, while the 0.11 eV and 0.27 eV Cl_2 did reach complete saturation. Furthermore, the 0.65 eV Cl_2 had a much slower rate of decay toward zero sticking than the 0.11 eV and 0.27 eV Cl_2.

2. High Surface Temperature Sticking Curves

Figure 6.7c displays a typical 500 K Al(111) surface temperature King and Wells-type sticking curve for dosing with a 0.65 eV Cl_2 molecular beam. The high surface temperature (500 K) sticking curves from both experiments demonstrate nearly identical behavior for all three Cl_2 incident translational energies. The actual sticking probability values measured are not important, but rather the profile of the curve is critical. At 500 K surface temperature, upon exposure to the Cl_2 molecular beam, steady-state sticking conditions are instantaneously achieved and saturation coverage is never reached. This indicates that an equilibrium is quickly reached between the Cl_2 flux reaching the surface and the etch product desorption.

C. Aluminum Chloride Etch Rate Profiles

Fixing the delay between the chopper trigger and the laser fire time (i.e. focusing on one particular exit velocity channel, v_r) allows for the detected ion intensity to be monitored versus elapsed time (see Figures 1.8 and 1.9). In this experiment, the intensity of the detected Al^+ ions is proportional to the rate of desorption of aluminum chloride molecules which exit the surface at a velocity v_r. For these experiments, the most-probable velocity found for each particular system (as presented earlier) was used to

select the fixed time-of-flight value, t_r, such that $v_r = d_{ls}/t_r$. As a check to ensure that the peak positions of the TOF spectra were not actually moving, a number of spectra were taken for the various Cl_2 incident energies and surface temperatures, showing that (aside from the case of 0.65 eV incident Cl_2 at 100 K surface temperature) the observed peak velocity was constant for at least 15 minutes of dosing. Therefore, we are confident that any changes in the detection intensities found by this experiment are indeed changes in the etch rates, rather than changes in peak exit velocities. The actual etch rates were not calculated in this experiment: the focus of this paper did not warrant such a quantitative study, but rather just a qualitative understanding of the process.

1. Low Surface Temperature Etch Rate Profiles

The 100 K surface temperature etch rate profiles for the 0.11 eV and 0.27 eV Cl_2 molecular beam-dosing showed the expected behavior (see Figure 6.8a) that one would predict from the sticking curves and time-of-flight data. Both incident molecular beam energies yielded detectable etch signal within at most two or three molecular beam pulses. This corresponds to an approximate surface coverage of only about 2-3% of a monolayer, at which we observe spontaneous etching of the surface. The Al^+ etch curves typically showed a short pseudo-steady-state etching region (i.e. a relatively flat etch signal) for the first 20 seconds of dosing, followed by an exponential decay to an etch signal of zero. The 0.11 eV incident Cl_2 etch signal decayed to zero with a $1/e$ lifetime of 10 seconds, and the 0.27 eV incident Cl_2 system showed a $1/e$ lifetime of about 8 seconds. The variation in lifetimes most likely stems from a combination of slightly differing Cl_2 fluxes at the surface, small differences in sticking probabilities, and slight

dissimilarities in the actual etch rates for the two different energy incident beams. These times are also longer than those in the sticking experiments due to the difference in Cl_2 molecular beam flux (60 Hz unchopped beam for the King and Wells sticking experiments vs. 10 Hz chopped beam for the etch rate profiles and time-of-flight experiments).

Two different modes of etch behavior are observed for 100 K surface with the 0.65 eV incident Cl_2 beam, as shown in Figure 6.9. Figure 6.9a displays an etch rate profile curve for 100 K surface temperature Al(111) exposed to a 0.65 eV Cl_2 beam while monitoring the fast velocity mode (600 m/s), and Figure 6.9b displays the profile curve for the same system while monitoring the slow velocity mode (250 m/s). The first, and fastest, etch mode is found for very low surface coverages (total dosing time of ≤ 10 seconds), exhibiting a pseudo-steady-state region lasting for the first 5-6 seconds of dosing and a subsequent decay lifetime of about 4 seconds. This behavior corresponds to the fast mode seen in the TOF experiments. The second, slower mode is found at slightly higher surface coverages (total dosing time of > 10 seconds) or from Cl_2 pre-exposed surfaces. In this mode, the pseudo-steady-state region lasts longer (~15 sec) and has a longer decay lifetime (~60 sec). Both velocity modes exhibit the same instantaneous etch product signal within ~1% ML surface coverage as was seen with the 0.11 eV and 0.27 eV incident Cl_2 energy beams.
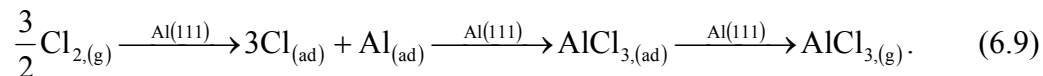
2. High Surface Temperature Etch Rate Profiles

Figure 6.8b shows an etch rate profile for 500 K surface temperature Al(111) exposed to a 0.27 eV incident translational energy Cl_2 beam. The high surface

temperature etch rate profiles recorded in this experiment all exhibit the same basic behavior, independent of incident Cl_2 kinetic energy. As with the 100 K surface temperature studies, all three incident molecular beam energies yielded a detectable steady-state etch signal within, at most, two or three molecular beam pulses. This corresponds to an approximate surface coverage of only about 2-3% ML, which is the minimum coverage at which we observe spontaneous etching of the surface. The etch-rate profiles for the elevated surface temperatures also displayed instantaneous steady-state conditions that lasted for the entire span of the experimental run-time (at least 15 minutes of continual dosing). Therefore, not only does the surface immediately begin to etch upon exposure to small amounts of Cl_2 (< 5% monolayer), but it continues to etch indefinitely at exactly the same rate.

D. Computational Data

Density functional theory (DFT) calculations under periodic boundary conditions, with Vanderbilt-type ultrasoft pseudopotentials (US-PP) and plane-wave basis were performed on the $Cl_{2(g)}/Cl_{(ad)}/Al(111)$ system in an effort to provide information concerning both the possible surface reactions and the energetics of those reactions. The goal was to study the nature of the adsorption of Cl on the Al(111) surface, including adsorption site preference and possible Cl adsorbate clustering effects on flat terraces. Calculations were also performed to help characterize the model reaction sequence occurring in the present study,

$$\frac{3}{2}Cl_{2,(g)} \xrightarrow{\text{Al(111)}} 3Cl_{(ad)} + Al_{(ad)} \xrightarrow{\text{Al(111)}} AlCl_{3,(ad)} \xrightarrow{\text{Al(111)}} AlCl_{3,(g)}. \qquad (6.9)$$

Namely, this total reaction includes the dissociation of incident Cl_2 and adsorption of Cl fragments products onto the Al(111) surface, the reaction of Cl adsorbates with an Al adatom to form ground state $AlCl_3$ (as standard DFT only allows for the calculation of ground state energies and properties), and the desorption of ground state $AlCl_3$ from the Al(111) surface. Note that the above reaction equation does not explicitly state by which chemisorption mechanism the Cl adsorbates are produced; it states only that a total of three Cl atoms are required and the overall products can result from any combination of Cl_2 molecules (two or three) and chemisorption mechanisms (direct abstractive or precursor-mediated). The computational results concerning relative total energies for these calculations can be found in Table 6.2, and those directly associated with the above reaction sequence are presented diagrammatically in Figure 6.10a.

1. Cl Adsorption on Al(111)

The first reaction of interest in this sequence is the dissociation of gas-phase Cl_2 and the subsequent adsorption of the resultant Cl atoms onto the Al(111) surface:
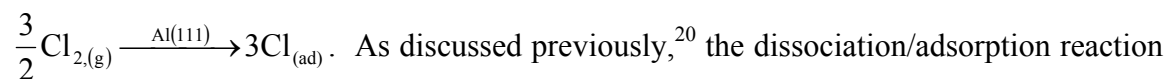
$\frac{3}{2}Cl_{2,(g)} \xrightarrow{\text{Al(111)}} 3Cl_{(ad)}$. As discussed previously,[20] the dissociation/adsorption reaction of Cl_2 on Al(111) proceeds via two different pathways: direct abstractive chemisorption (remote dissociation) and indirect precursor-mediated chemisorption (surface dissociation). In the direct mechanism, as a Cl_2 molecule approaches the Al(111) surface an electron can be transferred from the Fermi sea of the metal to the Cl_2, instantly

creating a Cl_2^- molecular ion. This ion resides high on the repulsive part of the intermolecular potential, resulting in dissociation into a Cl^- ion and a neutral Cl fragment. Note that the closer the Cl_2 is to the surface at the moment of the electron transfer, the higher on the repulsive part of potential the ion will reside. The final result is that the Cl^- ion is drawn to the surface and eventually chemisorbs while the neutral Cl is ejected back into the gas phase. In contrast, for the indirect mechanism, dissociation occurs after the neutral molecule has reached the surface (without being ionized) and has been subsequently trapped in a shallow physisorption state. Dissociation in this manner, while dependent upon the Cl_2 incident molecular orientation with respect to the surface, can either result in the ejection of a Cl neutral into the gas phase and a single Cl adsorbate, or it can result in the adsorption of both Cl atomic fragments. However, regardless of the mechanism, the final chemisorption energies (bond strengths) for Cl onto Al(111) will be the same.

The energetics for the Cl_2 dissociation/adsorption reaction on Al(111) were calculated using the total energy difference between a system consisting of two Cl non-interacting adsorbates on the Al(111) surface and a system consisting of a Cl_2 molecule residing in the gas phase above the Al(111) surface. The calculated reaction energy per Cl adsorbate was -2.12 eV with respect to molecular chlorine far from the surface; for the given reaction, $\frac{3}{2}Cl_{2,(g)} \xrightarrow{Al(111)} 3Cl_{(ad)}$, the total reaction energy is -6.36 eV. The various dissociation/adsorption mechanisms were considered, and calculations were performed to check for consistency in the final overall reaction energy with respect to mechanism and method.

In searching for the lowest-energy (i.e. most stable) adsorption sites for the Cl adsorbates, it was found that adsorbates strongly prefer ontop sites over both bridge and three-fold hollow sites. The relaxed geometries of the Cl adsorbate calculations also show that the Cl atoms tend to pull the Al atoms to which they were bonded into positions that are above the average terrace plane. In addition, the Al atoms that occupied the nearest-neighbor positions were found to have physically relaxed into the resulting voids, placing them in positions that are slightly below the average terrace plane. Overall, the largest displacement in the z-direction was observed for the final $Cl_{(ad)}$ ontop site geometry, where the bonded Al atom was pulled to a position of over 0.4 Å above the terrace plane. The displacements seen in the final hollow site and bridge site geometries were similar to those of the ontop site geometry, but smaller in magnitude by at least a factor of 2.

The low-temperature ion-assisted etch model forwarded by Ikawa et al.[9] included the formation of two-dimensional clusters of Cl adsorbates on the Al(111) surface to help explain the enhancement of the low-temperature etch rate in an ECR plasma. To test this hypothesis, adsorbate clusters containing three $Cl_{(ad)}$ atoms residing in nearest-neighbor equivalent sites (i.e. ontop-ontop-ontop, bridge-bridge-bridge, and hollow-hollow-hollow clusters, all in a triangular geometry) were allowed to structurally relax. It was found that each of these clusters was unstable, and that repulsions between the $Cl_{(ad)}$ atoms forced them to physically move away from each other on the surface, giving final interatomic distances of at least 4 Å. Even after the minimization of interatomic forces, the total energy of the initially-ontop-clustered $Cl_{(ad)}$ system (the system with the lowest relative total energy) was found to be higher than that of the dispersed ontop $Cl_{(ad)}$ system by 0.3

eV. As a result, we believe that clustering of Cl adsorbates, even at temperatures as low as 100 K, is unlikely.

2. Formation and Desorption of AlCl₃

The reaction involving the formation of adsorbed $AlCl_3$, $3Cl_{(ad)} + Al_{(ad)} \xrightarrow{\text{Al(111)}} AlCl_{3,(ad)}$, was modeled computationally using an aluminum adatom and three nearby chlorine adsorbates. The Al adatom, rather than a standard surface atom, was chosen for use as the reaction center in an effort to model Al atom defect sites such as step-edges and regrowth islands (as well as actual adatoms). These unique sites are more exposed to surface adsorbates in the low-coverage regime and provide a good model system for this set of conditions. The formation energy was calculated by subtracting the total energy of the non-bonded reactant system from the total energy of the AlCl₃ adsorbate system: $\Delta E_f = E_{tot}(AlCl_3) - E_{tot}(Al+3Cl)$. Note that for the non-bonded reactant system, the Cl adsorbates were positioned outside of the bonding range of the Al adatom, and after structural relaxation yielded no attractive forces toward the Al adatom. To ensure that both the products and the reactants were all in the lowest energy geometric configurations possible, multiple adsorption geometries were considered. The Al adatoms energetically preferred hollow site positions, while the Cl adsorbates remained most stable in their preferred ontop site positions. The AlCl₃ adsorbates showed no adsorption geometry preference within the estimated accuracy of the calculations (i.e. the AlCl₃ surface adsorption potential was essentially non-corrugated). The final value calculated from these simulations showed an $AlCl_{3,(ad)}$

formation energy of -0.70 eV with respect to the separate $Al_{(ad)}$ atom and 3 $Cl_{(ad)}$ atoms on the Al(111) surface.

The final step of this reaction sequence is the desorption of the ground state $AlCl_3$ adsorbate into the gas phase, $AlCl_{3,(ad)} \xrightarrow{\text{Al(111)}} AlCl_{3,(g)}$. We can only consider ground state energies, as standard DFT is unable to predict excited states. The final desorption energy, $\Delta E_f = E_{tot}(AlCl_{3,(g)}) - E_{tot}(AlCl_{3,(ad)})$, was calculated to be +0.67 eV. The positive value indicates that the desorption of the ground state etch product is endothermic in this case. In other words, the bottom of the chemisorption well for ground state $AlCl_3$ on the Al(111) surface is 0.67 eV below the vacuum level. This means that if the ground state $AlCl_3$ is to exit the surface with a translational energy of 0.2 eV, it must overcome first the 0.67 eV deep potential well and then a barrier to desorption of about 0.2 eV, for a total energy requirement of about 0.87 eV. We would like to restate that these calculated energies describe the ground state system only and do not account for any excited state properties or energies. We will show, however, that the existence of such excited states can indeed account for the hyperthermal desorption of $AlCl_3$.

E. Etch Product Identification

We now return to the task of etch product species assignment. Our previous assumptions, based upon reports in the literature by Winters[3] and van Veen et al.,[5] lead to the conclusion that the major etch product detected in the 500 K surface temperature experiments was $AlCl_3$. Recall that $AlCl_3$ was reported by van Veen et al. as the major etch species at pressures around 7.5×10^{-7} Torr (Cl_2 surface flux of 7×10^{16} molecules cm^{-2} sec^{-1}) and temperatures between 450 K and 750 K. Our experiments have made use of a

much lower flux (1.0×10^{13} - 3.0×10^{13} molecules cm^{-2} sec^{-1}), and therefore lower pressure molecular beam (i.e. no post-desorption dimerization), and we have shown that the etch products are hyperthermal regardless of which species of aluminum chloride we utilize for data analysis. We can also eliminate AlCl as a possible etch product at 500 K due to its high binding energy to the substrate.[5] After these considerations are taken into account, we state with confidence that AlCl$_3$ is the etch product at 500 K surface temperature.

The etch product identity at 100 K surface temperature is, however, a matter of some question. All previous experiments performed near room temperature report an Al$_2$Cl$_6$ etch product, but these were carried out under considerably higher Cl$_2$ fluxes (> 7×10^{16} molecules cm^{-2} sec^{-1}), surface coverages (> 1 ML), and pressures (> 7.5×10^{-7} Torr) than were our experiments. One must note that it is under these conditions that post-desorption chemistry may occur. Consideration of the very low Cl$_2$ incident fluxes (1.0×10^{13} – 3.0×10^{13} molecules cm^{-2} sec^{-1}) and surface coverages (1-3% ML) at which spontaneous etching was observed in our experiments leads us to believe that post-desorption gas-phase dimerization reactions were nonexistent and that any aluminum chloride etch products were detected as-desorbed, as either AlCl$_3$ or Al$_2$Cl$_6$. The very low surface coverages also make reasonable the assumption that the concentration of Cl adsorbates on the Al(111) surface at the onset of spontaneous etching was too small to provide for the formation of a large amount of surface Al$_2$Cl$_6$ species, especially since the etching begins with the equivalent of 1% ML Cl$_2$ surface dose, as shown in the etch-rate profiling experiments. Finally, we note that the exit velocities of the etch products at both the 100 K and 500 K surface temperatures were essentially equal (with the exception

of the anomalous slow mode at 100 K surface temperature and 0.65 eV incident Cl_2), strongly indicating that the identity of the etch products at both temperatures are indeed identical. Therefore we assert with confidence that the etch product species at 100 K in our ultra-low coverage experiments is $AlCl_3$. It is possible, however, that the etch product being detected in the anomalous slow, high-coverage mode may very well be Al_2Cl_6.

6.5 DISCUSSION

A. Fast Chlorine Adsorbate Agglomeration

A high rate of reaction of the adsorbed $Cl_{(ad)}$ on the Al(111) surface to form $AlCl_{3(ad)}$ is consistent with the significant etch product desorption observed at the very low coverage (< 5% monolayer) conditions under which the time-of-flight experiments were performed. Indeed, Park et al. forwarded a model consisting of fast surface diffusion and agglomeration of Cl adsorbates, and fast subsequent reaction rates of intermediates on the Al surface, as ion bombardment was found to have no effect on the etch rate.[4] Our experimental sticking probability results are also consistent with a fast diffusion/agglomeration mechanism, and the aluminum chloride etch rate profiles provide directly observable evidence of unusually fast etch product formation in this system.

The etch rate profiles show aluminum chloride desorption products within just two or three molecular beam pulses, which corresponds to a surface coverage of less than 5% of a monolayer. Such a phenomenon is only possible if there exists a mechanism of fast agglomeration of the Cl adsorbates into reactive positions on the aluminum surface

that creates the observable $AlCl_3$ gas-phase etch products. The data is consistent with the fast diffusion of the Cl adsorbates across the Al(111) surface, such that molecules, or even small islands, of aluminum chlorides are produced and then immediately desorb.

DFT-GGA slab calculations performed on a model $Cl_{(ad)}$/Al(111) system indicate that there is a reasonable thermodynamic drive toward adsorbate agglomeration around and reaction with Al adatoms: the formation of the $AlCl_3$ etch products is exothermic by 0.70 eV per molecule. It is likely that this favorable reactivity would also be seen at Al regrowth islands and step edges. Sufficient numbers of such sites should exist on the surface to account for the significant initial etch rates seen in our low-coverage experiments. The 100 K sticking probability and etch rate measurements are also consistent with the hypothesis that etching occurs favorably at adatoms, regrowth islands, and step edges. At low temperatures, etching is quickly quenched and the surface becomes saturated with Cl adsorbates because there is insufficient thermal energy to regenerate the reactive sites. In contrast, we observe in the 500 K sticking probability and etch rate measurements that surface saturation is never reached and that etching is never quenched, indicating that enough thermal energy exists to regenerate the highly reactive etch sites under these conditions. It should be noted that a defect-dependent mechanism such as the one we propose here is likely to exhibit effects related to the surface history. Effects of this nature may be observable in the low temperature sticking or etch rate experiments, where a slight increase in the length of the initial etching rate is expected and yields a longer time to surface saturation. We did not pursue in depth experiments concerning this issue, though, because these effects would best be probed with low-temperature scanning tunneling microscopy (LT-STM), whereby one could

quantitatively account for the number and type of defect sites on the surface; such experiments are beyond the scope of the present study.

Our calculations also indicate that adsorbed Cl atoms tend to pull the adjacent Al surface atoms out of the surface plane by as much as 0.4 Å. The fact that the second-nearest neighbor Al atoms then sink into the partial voids left behind provides for an even larger relative atomic displacement for the affected Al surface atoms. It is possible that displaced surface atoms such as these would be more prone to both attack and removal by nearby Cl adsorbates (similar to the Al adatom case). It is also possible that this displacement could reduce the energy requirements for Al adatom/vacancy creation. However, such an effect was not directly observed in the calculations because only single-point and geometry relaxation DFT calculations, which are carried out at a computational temperature of 0 K, were performed, not actual molecular dynamics simulations.

B. Activated Chemisorption States

Hyperthermal etch product exit velocities, such as those observed in our low-coverage Cl_2/Al(111) system experiments, can be explained with four possible mechanistic models: first, activated desorption, in which the ground state aluminum chloride chemisorption potential well lies below the vacuum level and a barrier to desorption resides above the vacuum level (see Figure 6.10b); second, activated chemisorption states, in which there exists at least one aluminum chloride adsorption state with a potential well at an energy above the vacuum level (see Figure 6.10c); a third

case in which the energy of reaction is channeled into translational energy for the desorbing aluminum chloride; and finally, collision-induced desorption.

The latter two models can be easily eliminated from consideration. It is unlikely that any reasonable amount of excess energy from the formation of aluminum chlorides could be sufficiently channeled into translational energy, as it is well known that localized energy dissipates quickly on metal surfaces. Dynamics simulations concerning the dissociative chemisorption of O_2 on Al(111) have found that the transfer of energy to the substrate lattice is much too effective to allow for a large post-dissociation adsorbate mobility.[31-33] For the O_2/Al(111) system, there is a much higher exothermicity than for the Cl_2/Al(111) reaction (-7.95 eV per site with respect to the free oxygen atom), indicating that this mechanism is unlikely and can be eliminated. It is also unlikely that collision-induced desorption could produce etch products with such high translational energies, especially at low surface coverages (< 5% monolayer). It is possible that at high surface temperatures (500 K) and high incident kinetic energy there may be components of the etch product translational energy that are produced via collision-induced desorption; this would slightly increase the measured most-probable etch product exit velocity for the high-energy (0.65 eV) incident Cl_2 beam. However, this mechanism is not expected to play a role for the lower energy incident Cl_2 beams (0.11 eV and 0.27 eV) or on the low temperature (100 K) surface.

It is necessary at this point to distinguish between the activated desorption and the activated chemisorption state models for our system of study. Our basic calculations cannot be used to directly predict a desorption mechanism in this case because DFT is known to be inaccurate in predicting barrier heights and weak binding potentials. We

can, however, use the calculated desorption energy values to support our mechanistic assertions. Because we observe hyperthermal exit velocities at 100 K, the activated desorption model seems inconsistent with the data, as it is unlikely that the etch products could easily surmount such an activation barrier at this temperature. According to the DFT calculations and the measured exit translational energies, the barrier height for ground state $AlCl_3$ desorption would be a total of about 0.87 eV, which is considerably large at these temperatures (100-500 K). Therefore, we assert that our results are most consistent with the existence of aluminum chloride activated chemisorption states on the Al(111) surface, desorption from which results in hyperthermal etch product velocities.

6.6 CONCLUSIONS

Hyperthermal desorption of aluminum chloride etch products from Cl_2/Al(111) has, for the first time, been observed under low coverage conditions (< 5% monolayer) at both low (100 K) and high (500 K) surface temperatures and at a variety of incident Cl_2 kinetic energies. Etching is found to spontaneously begin immediately upon exposure of the Al(111) surface to pulsed molecular beams of Cl_2. We believe these hyperthermal desorption products are only observable under very low Cl_2 fluxes and/or surface coverages, and have thus not previously been seen in high coverage experiments. The model presented here to explain these phenomena includes a combination of both fast Cl adsorbate diffusion and agglomeration at Al step-edges, regrowth islands, and adatoms, with fast formation of $AlCl_3$, and the existence of activated aluminum chloride chemisorption states with potential energies above the vacuum level.

6.7 ACKNOWLEDGEMENTS

Chapter 6, in full, is a reprint of the material as it appears in the following publication, for which the dissertation author was the primary investigator and author:

T. J. Grassman, G. C. Poon, A. C. Kummel, "Low coverage spontaneous etching and hyperthermal desorption of aluminum chlorides from $Cl_2/Al(111)$," Journal of Chemical Physics **121**, 9018 (2004).

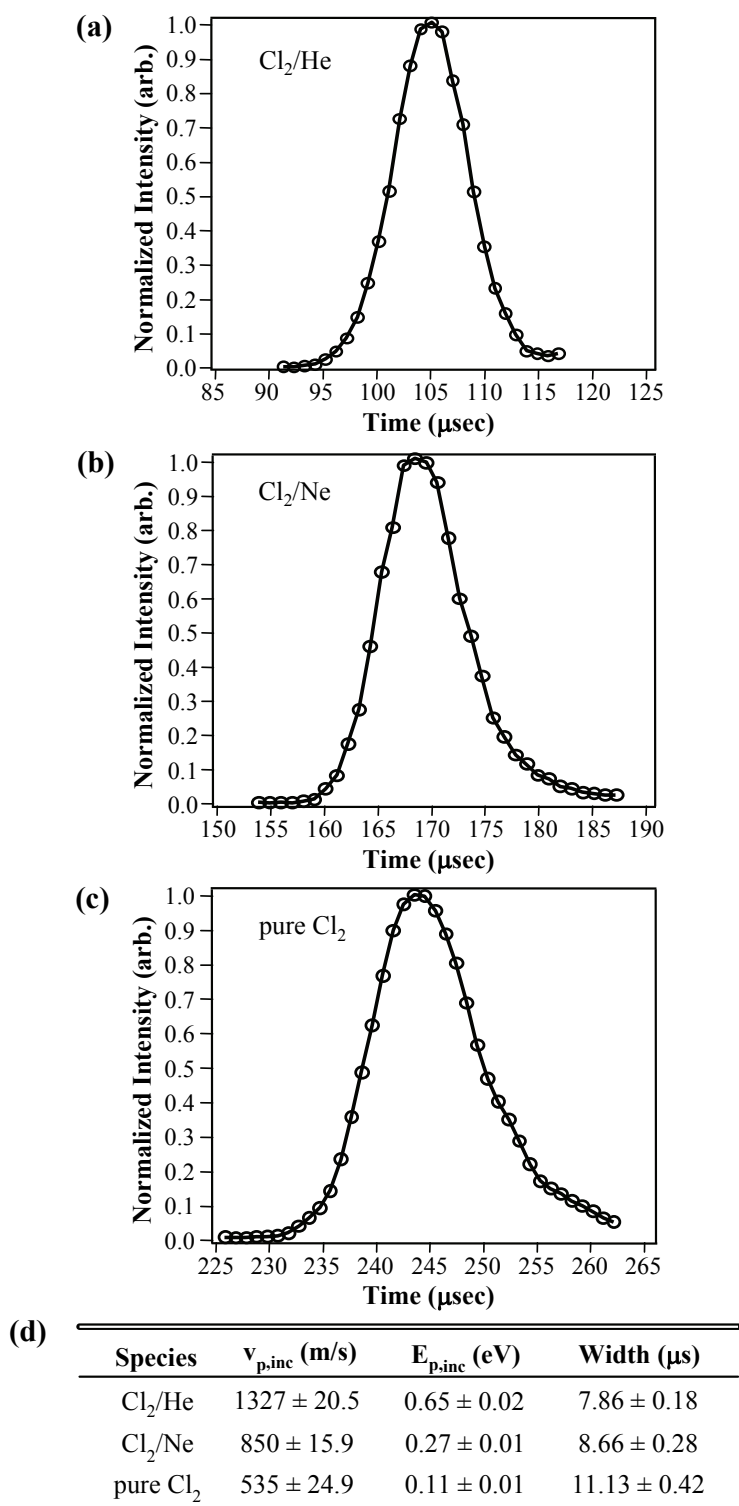| Species	$v_{p,inc}$ (m/s)	$E_{p,inc}$ (eV)	Width (µs)
Cl_2/He	1327 ± 20.5	0.65 ± 0.02	7.86 ± 0.18
Cl_2/Ne	850 ± 15.9	0.27 ± 0.01	8.66 ± 0.28
pure Cl_2	535 ± 24.9	0.11 ± 0.01	11.13 ± 0.42

FIGURE 6.1. Time-of-flight distributions for mechanically chopped (7 µs chopper open time) incident molecular beams of (a) 5% Cl_2 seeded in He, (b) 5% Cl_2 seeded in Ne, and (c) pure Cl_2. The table (d) gives the velocities, energies, and widths of the incident Cl_2 beams used in this experiment.

TABLE 6.1. Measured velocities, translational energies, and peak-to-width ratios for desorbing aluminum chlorides at all incident Cl2 translational energies and Al(111) surface temperatures studied.

Dose Species	E_{inc} (eV)	T_s (K)	v_p (m/s)	E_{AlCl_3} (eV)[a]	$E_{Al_2Cl_6}$ (eV)[b]	v_p/w
Cl$_2$/He: fast[c]	0.65	100	612 ± 21	0.26 ± 0.02	0.52 ± 0.04	0.65 ± 0.06
Cl$_2$/He: slow[d]	0.65	100	256 ± 9	0.05 ± 0.01	0.09 ± 0.01	0.84 ± 0.08
Cl$_2$/He	0.65	500	653 ± 16	0.30 ± 0.01	0.59 ± 0.03	0.56 ± 0.02
Cl$_2$/Ne	0.27	100	518 ± 22	0.19 ± 0.02	0.38 ± 0.03	0.82 ± 0.03
Cl$_2$/Ne	0.27	500	553 ± 14	0.21 ± 0.01	0.43 ± 0.02	0.76 ± 0.03
pure Cl$_2$	0.11	100	460 ± 22	0.14 ± 0.01	0.30 ± 0.03	0.69 ± 0.06
pure Cl$_2$	0.11	500	533 ± 10	0.20 ± 0.01	0.39 ± 0.01	0.71 ± 0.05

a: Translational energy calculated from mass of AlCl3 etch product and measured vp
b: Translational energy calculated from mass of Al2Cl6 etch product and measured vp
c: Fast exit velocity mode; from fresh, clean 100 K surface
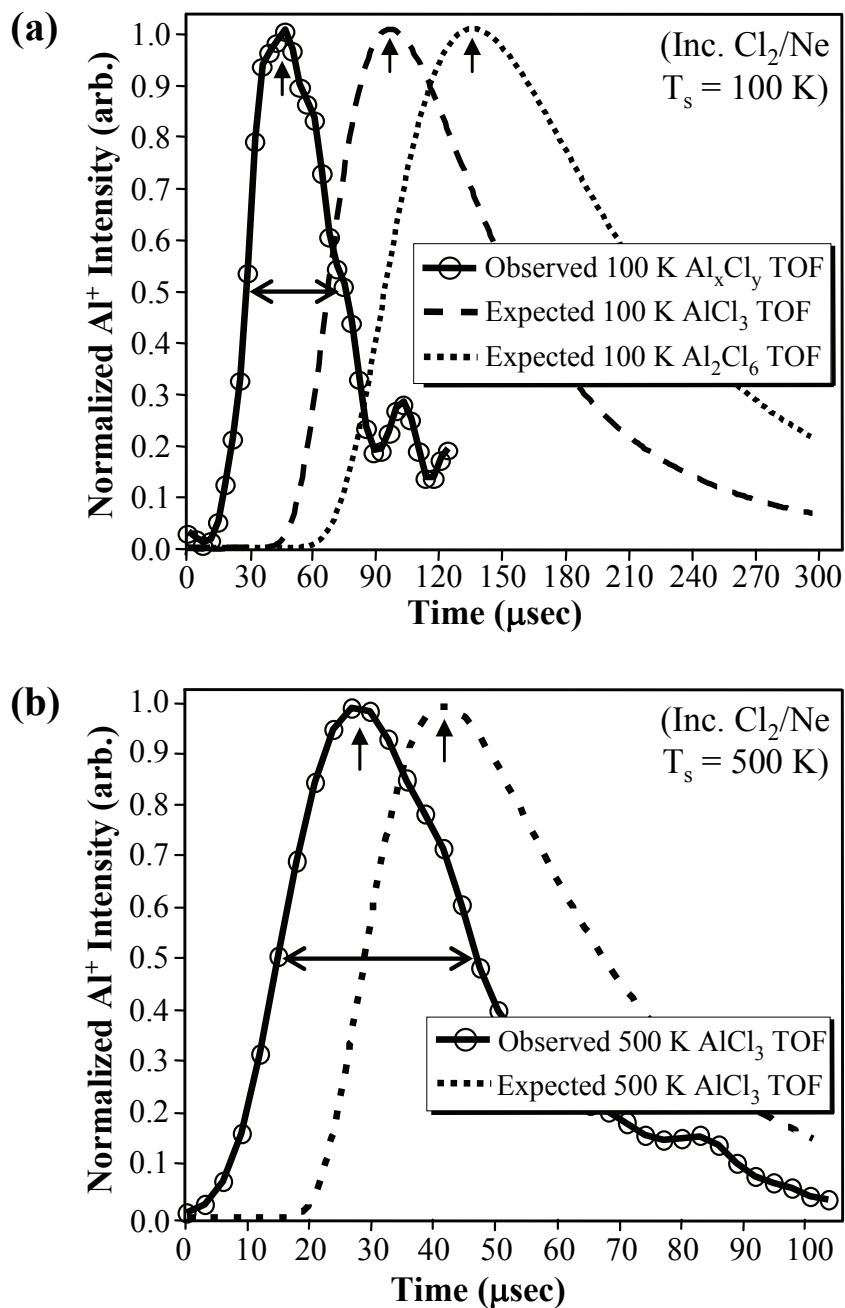d: Slow exit velocity mode; from Cl2 pre-exposed 100 K surface

FIGURE 6.2. Maxwell-Boltzmann-like time-of-flight distribution curves for the etch products from the 0.27 eV incident Cl_2 beam on the (a) 100 K and (b) 500 K Al(111) surface. The solid curves show the experimentally observed desorption distribution, and the dashed curves show the expected thermal desorption time-of-flight distributions for the etch product mass and surface temperature of interest, as indicated in the figures. The most probable time-of-flights are indicated by the vertical, single-headed arrows. The full-width half-max of the experimental distributions are indicated by the horizontal, double-headed arrows.
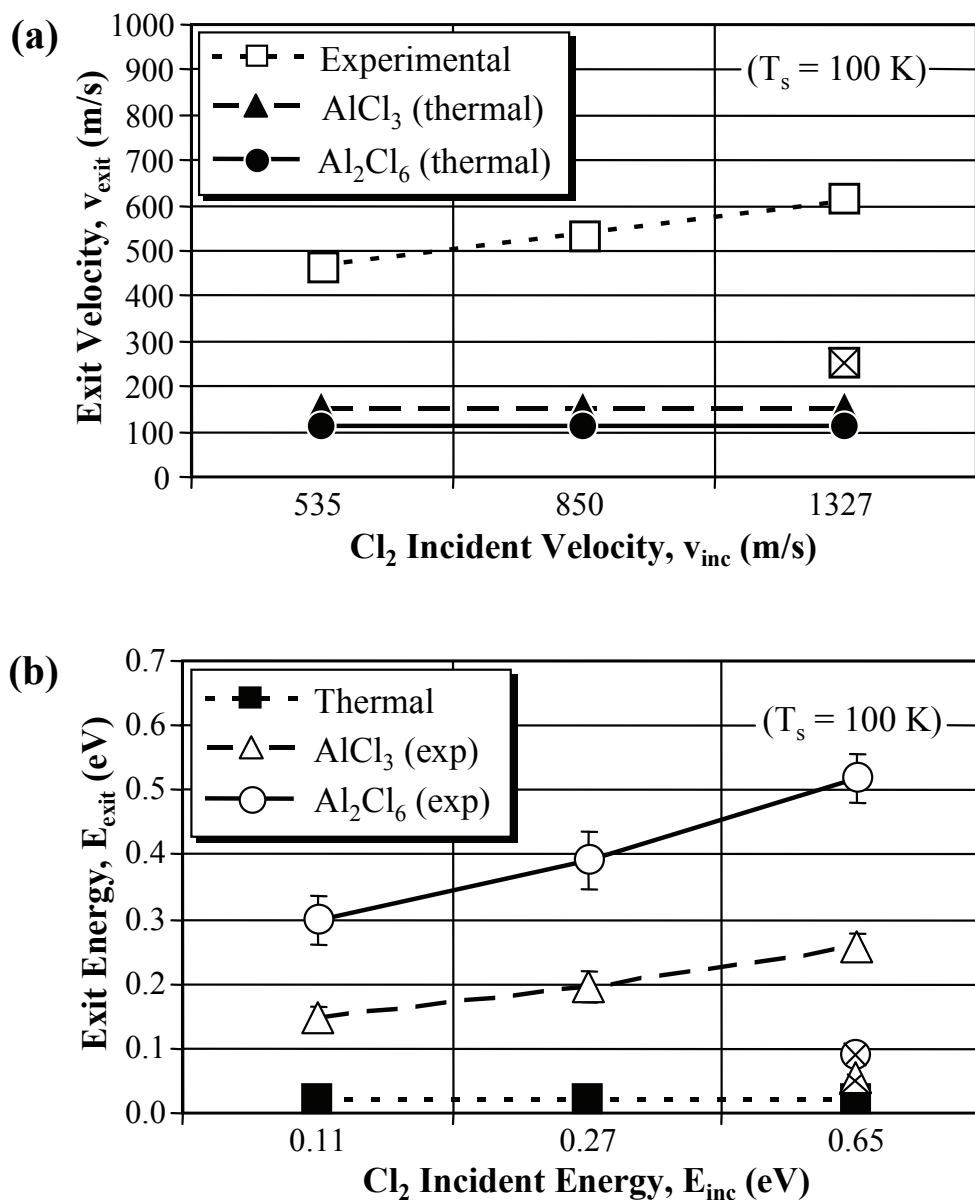
FIGURE 6.3. (a) Etch product exit velocities vs. Cl2 incident velocities for the 100 K Al(111) surface temperature case. The open squares are the experimental velocity data, and the filled circles and triangles represent the expected velocities of the possible etch products from thermal desorption. The anomalous slow component (Cl2 pre-exposed surface) is marked with an "X." (b) Etch product exit energies vs. Cl2 incident energies for the 100 K Al(111) surface temperature case. The open circles and triangles are the translational energies for the possible etch products as calculated from the experimental velocity data. The filled squares represent the expected translational energy from thermal desorption. The anomalous slow component (Cl2 pre-exposed surface) is marked with an "X." NOTE: Where experimental error bars are not seen, they are merely obscured from view by the data points.
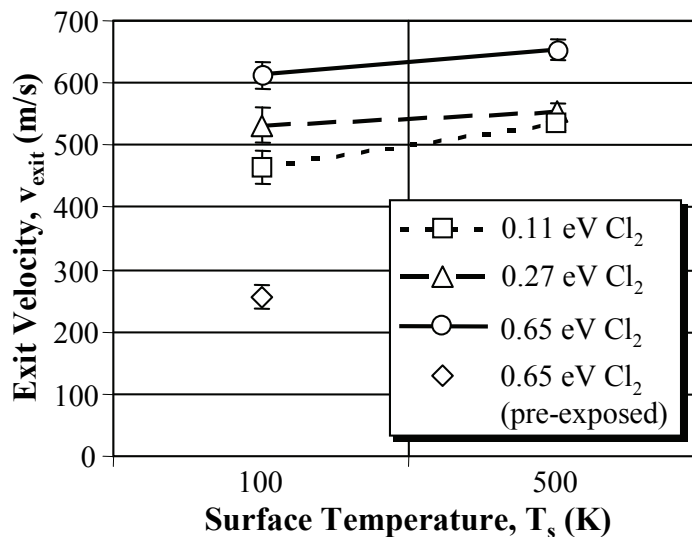
FIGURE 6.4. Experimental aluminum chloride etch product exit velocities vs. Al(111) surface temperature. Two exit velocity modes are observed for the 0.65 eV incident energy Cl_2 dose beam at $T_s = 100$ K, where the fast mode results from Cl_2 dosing upon a fresh, clean Al(111) surface and the slow mode results from the Cl_2 pre-exposed surface. At $T_s = 500$ K with 0.65 eV incident Cl_2 only a monomodal velocity distribution is observed, indicated here with the same shape (open circle, solid line) as the fresh-surface 100 K point.
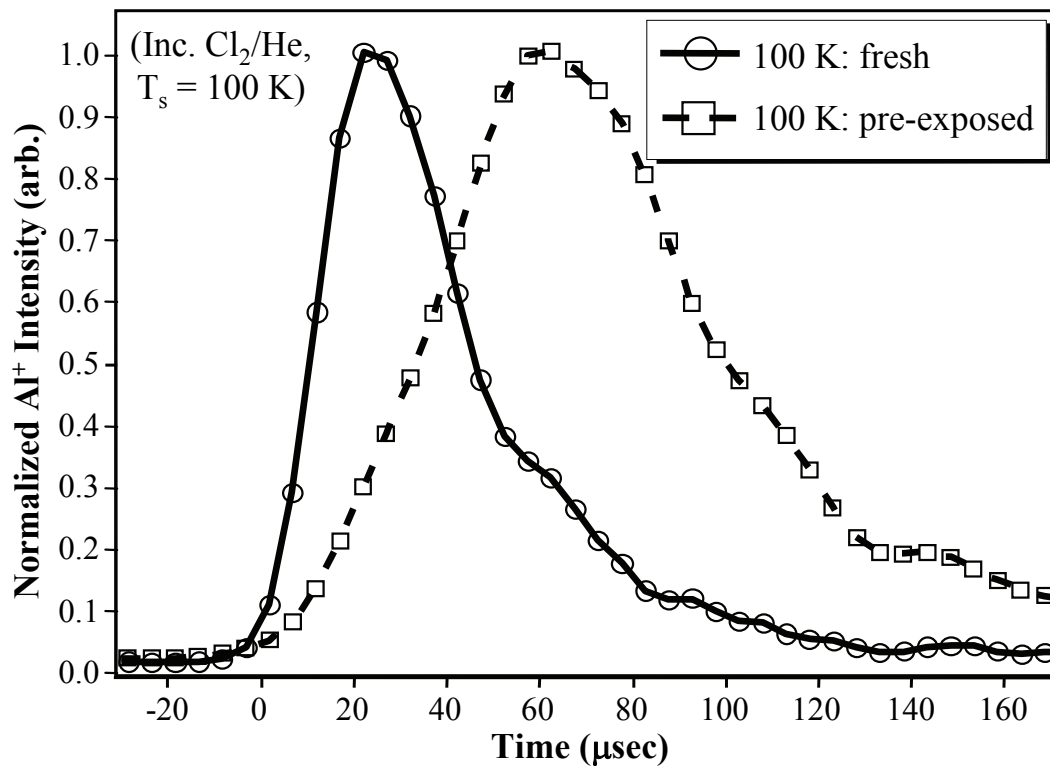
FIGURE 6.5. Two Maxwell-Boltzmann-like time-of-flight distribution curves for the 0.65 eV incident Cl_2 beam and the 100 K Al(111) surface. The solid curve shows the desorption distribution observed upon dosing of a fresh, clean surface, and the dashed curve shows the distribution observed upon dosing of a Cl_2 pre-exposed surface.
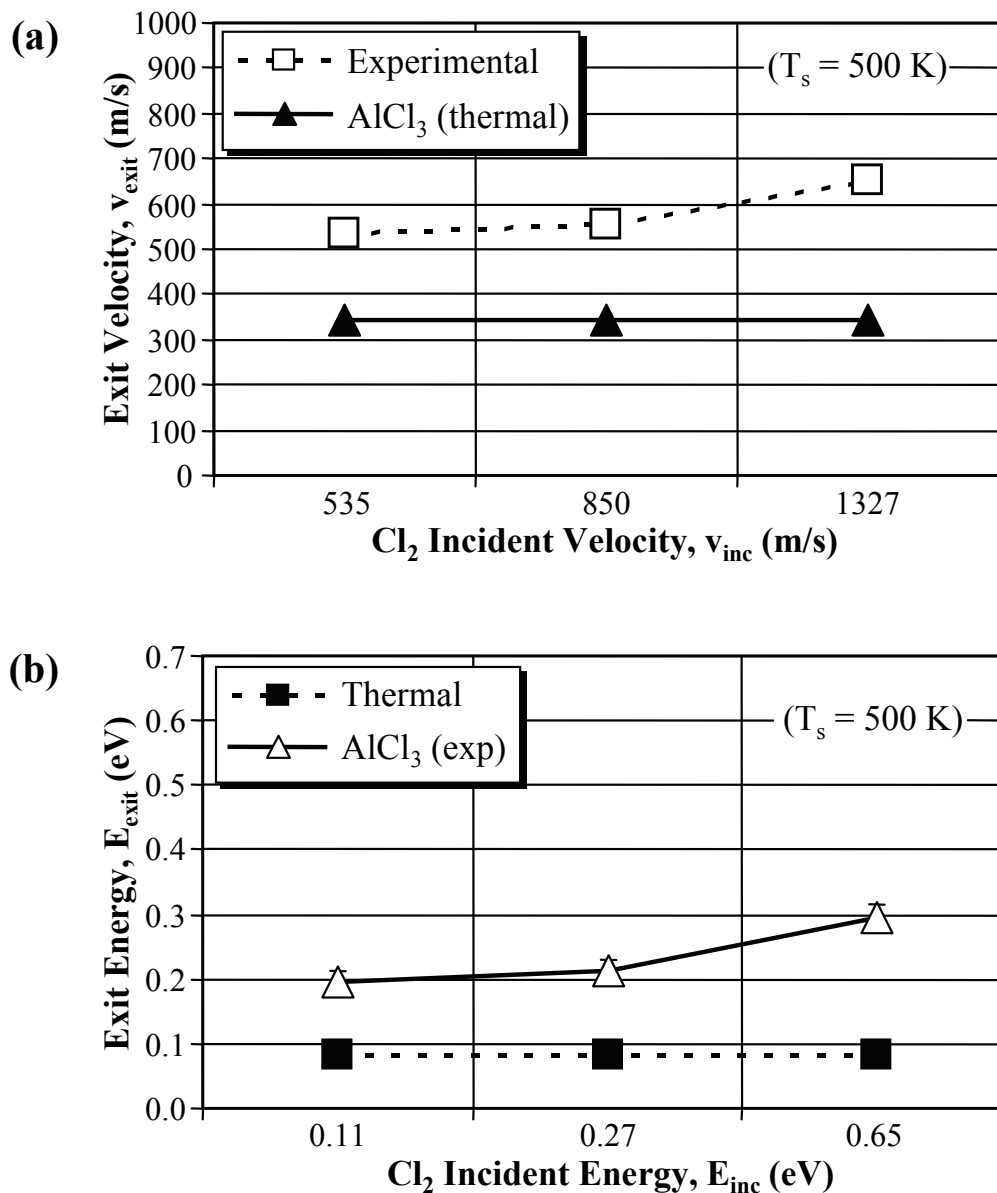
FIGURE 6.6. (a) Etch product exit velocities vs. Cl_2 incident velocities for the 500 K Al(111) surface temperature case. The open squares are the experimental velocity data, and the filled diamonds and triangles represent the expected velocities of the possible etch products from thermal desorption. (b) Etch product exit energies vs. Cl_2 incident energies for the 500 K Al(111) surface temperature case. The open diamonds and triangles are the translational energies for the possible etch products as calculated from the experimental velocity data. The filled squares represent the expected translational energy from thermal desorption. NOTE: Where experimental error bars are not seen, they are merely obscured from view by the data points.
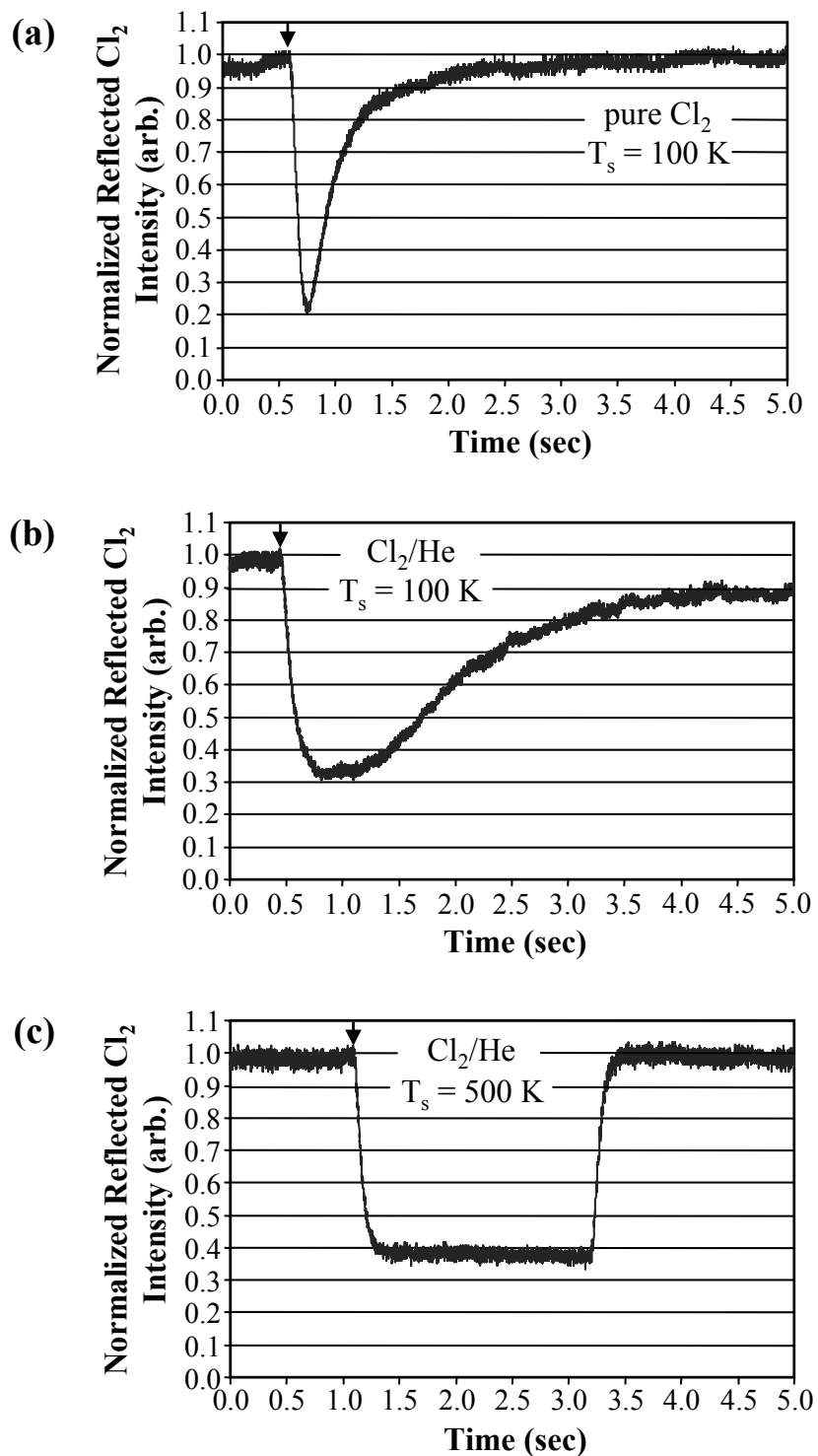
FIGURE 6.7. King and Wells sticking curves for (a) 0.11 eV incident energy Cl_2 on the 100 K surface and 0.65 eV incident energy Cl_2 on both the (b) 100 K surface and the (c) 500 K surface. The beginning of dose beam exposure is indicated on each curve by an arrow.
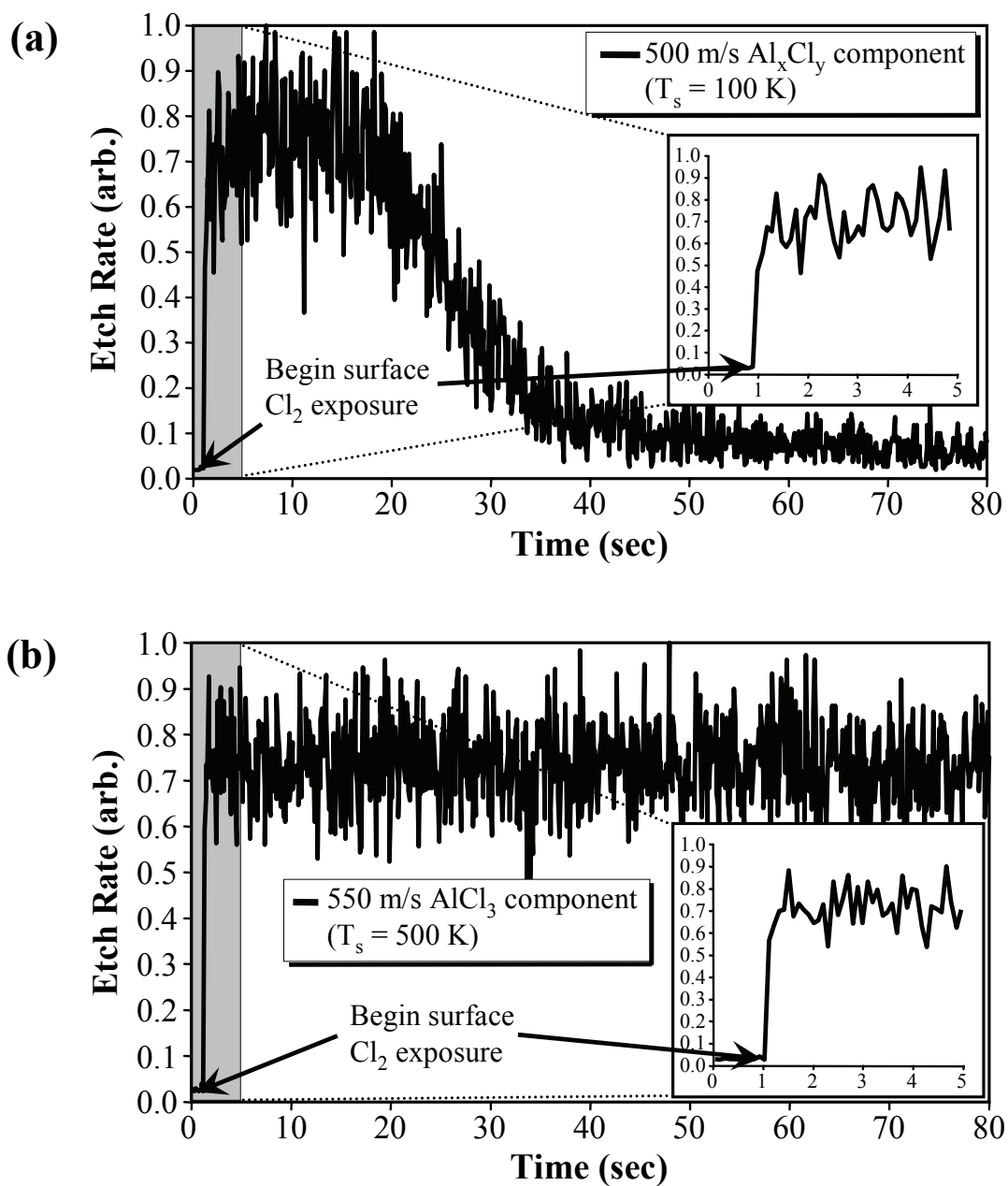
FIGURE 6.8. Etch rate profiles of the 0.27 eV incident energy Cl_2 beam on (a) the 100 K and (b) the 500 K Al(111) surface. The insets are enlargements of the shaded regions and show the first 5 seconds of data. Initial Cl_2 exposure is indicated by arrows.
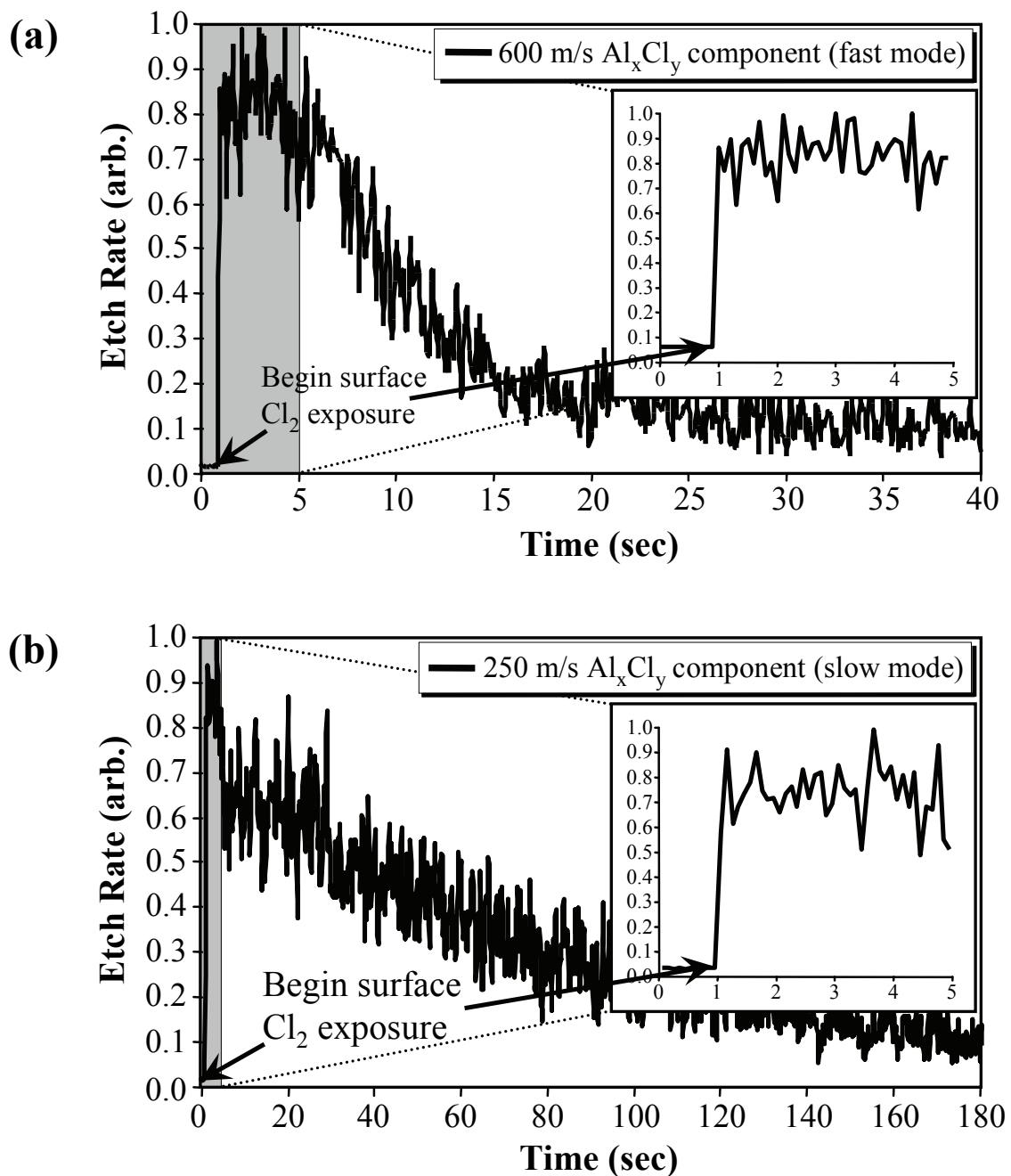
FIGURE 6.9. Etch rate profiles of the 0.65 eV incident energy Cl_2 beam on the 100 K Al(111) surface of (a) the fast mode exit energy Al_xCl_y and (b) the slow mode exit energy Al_xCl_y. The insets are enlargements of the shaded regions and show the first 5 seconds of data. Initial Cl_2 exposure is indicated by arrows. Note the change in length of the time axis in (b).

TABLE 6.2. Final computational relative total energies for DFT-GGA calculations performed on Cl/Al(111) system. The Al(111) slab calculations were performed with the VASP program, using a 5×4×1 Monkhorst-Pack 10 k-point mesh and plane-wave kinetic energy cut-off of 350 eV.

Geometry	ΔE_{tot} (eV)[a]	Geometry	ΔE_{tot} (eV)[b]
$Cl_{(ad)}$ ontop-site	0.00	$3Cl_{(ad)} + Al_{(ad)}$	0.00
$Cl_{(ad)}$ bridge-site	0.16	$AlCl_{3,(ad)}$ (Al hollow, Cl hollow)	-0.67
$Cl_{(ad)}$ hollow-site	0.29	$AlCl_{3,(ad)}$ (Al hollow, Cl ontop)	-0.70
Clustered[i] $Cl_{(ad)}$; bridge-sites[f]	0.11	$AlCl_{3,(ad)}$ (Al ontop, Cl bridge)	-0.70
Clustered $Cl_{(ad)}$; ontop-sites	0.18	$AlCl_{3,(g)}$: desorbed	-0.05

a: Difference in DFT total energies (per Cl adsorbate), with respect to the "Cl(ad) hollow-site" total energy.
b: Difference in DFT total energies, with respect to the non-bonded "3Cl(ad) + Al(ad)" total energy.
i: Initial clustered geometry, with Cl adsorbates in adjacent hollow sites.
f: Final relaxed geometry; Cl adsorbates moved from adjacent hollow-sites to nearby bridge-sites during relaxation.
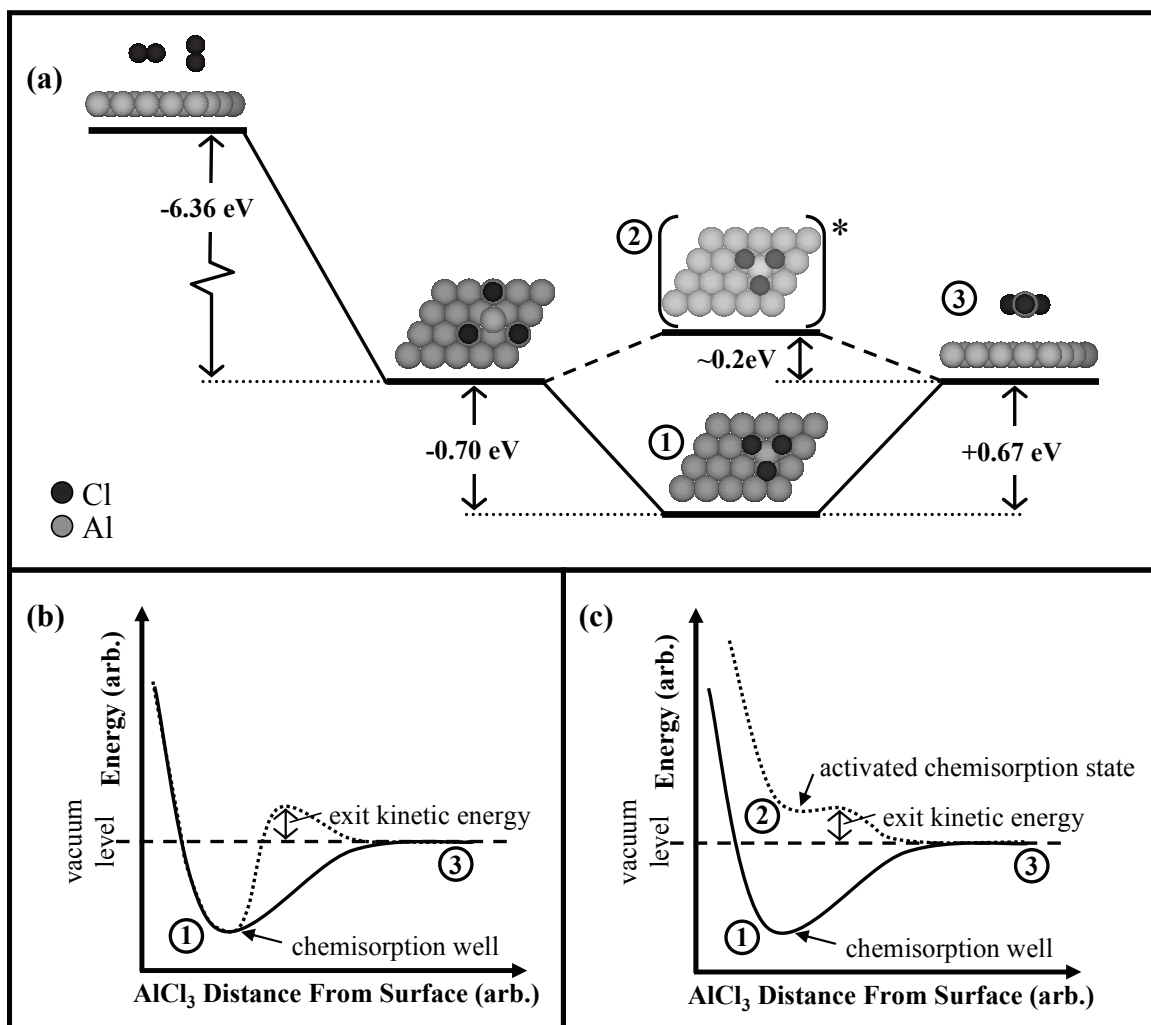
FIGURE 6.10. Computational (DFT) energy diagram (a) of the Cl_2 dissociation/adsorption reaction, followed by subsequent $AlCl_3$ etching from both the ground-state chemisorbed and the activated chemisorbed $AlCl_3$ (labeled **1** and **2**, respectively). Conceptual potential diagrams for $AlCl_3$ chemisorption/desorption are given for the (b) activated desorption and the (c) activated chemisorption state models for hyperthermal exit velocity of aluminum chloride etch products from low-coverage Cl_2 on Al(111). Points of interest between the reaction energy diagram and the corresponding position on the potential diagrams are signified by the circled numbers. The data presented in this paper is consistent with the activated chemisorption state model (c) rather than the activated desorption model (b).

6.9 REFERENCES

[1]   D. L. Smith and P. G. Saviano, J. Vac. Sci. Tech. **21**(3)**,** 768 (1982).

[2]   D. L. Smith and R. H. Bruce, J. Electrochem. Soc. **129**(9), 2045 (1982).

[3]   H. F. Winters, J. Vac. Sci. Tech. B **3**(3), 9 (1985).

[4]   S. Park, L. C. Rathburn, and T. N. Rhodin, J. Vac. Sci. Tech. A **3**, 791 (1985).

[5]   R. J. A. A. Janssen, A. W. Kolfschoten, and G. N. A. van Veen, Appl. Phys. Lett. **52**, 98 (1988).

[6]   D. A. Danner and D. W. Hess, J. Appl. Phys. **59**, 940 (1986).

[7]   T. A. Cleland and D. W. Hess, J. Vac. Sci. Technol. B **7**, 35 (1989).

[8]   N. N. Efremow, M. W. Geis, R. W. Mountain, G. A. Lincoln, J. N. Randall, and N. P. Economou, J. Vac. Sci. Technol. B **4**, 337 (1986).

[9]   T. Uchida, H. Aoki, M. Hane, S. Hasegawa, and E. Ikawa, Jpn. J. Appl. Phys. **32**, 6095 (1993).

[10]   J. W. Lutze, A. H. Perera, and J. P. Krusius, J. Electrochem. Soc. **137**, 249 (1990).

[11]   T. Smith, Surf. Sci. **32**, 527 (1972).

[12]   V. M. Bermudez and A. S. Glass, J. Vac. Sci. Technol. A **7**, 1961 (1989).

[13]   J. Bormet, J. Neugebauer, and M. Scheffler, Phys. Rev. B **49**, 17242 (1994).

[14]   T. F. Hanisco, C. Yan, and A. C. Kummel, J. Chem. Phys. **95**(8), 6178 (1991).

[15]   T. F. Hanisco and A. C. Kummel, J. Phys. Chem. **95**(22), 8565 (1991).

[16]   K. A. Pettus, T. S. Ahmadi, E. J. Lanzendorf, and A. C. Kummel, J. Chem. Phys. **110**(9), 4641 (1999).

[17]   K. A. Pettus, P. R. Taylor, and A. C. Kummel, Faraday Discuss. **117**, 321 (2000).

[18]   D. A. King and M. G. Wells, Surf. Sci. **29**(2), 454 (1972).

[19]   D. A. King and M. G. Wells, Proc. Roy. Soc. London Series A **339**(1617), 245 (1974).

[20]   G. C. Poon, T. J. Grassman, J. C. Gumy, and A. C. Kummel, J. Chem. Phys. **119**(18), 9818 (2003).

21   B. Berenbak, D. A. Butler, B. Riedmuller, D. C. Papageorgopoulos, S. Stolte, and A. W. Kleyn, Surf. Sci. **414**(1-2), 271 (1998).

22   G. Kresse and J. Hafner, Phys. Rev. B **47**, RC558 (1993).

23   G. Kresse, Thesis, Technische Universität Wien (1993).

24   G. Kresse and J. Furthmüller, Comput. Mat. Sci. **6**, 15 (1996).

25   G. Kresse and J. Furthmüller, Phys. Rev. B **54**, 11169 (1996).

26   D. Vanderbilt, Phys. Rev. B **41**, 7892 (1990).

27   G. Kresse and J. Hafner, J. Phys. Condens. Matter **6**, 8245 (1994).

28   D. J. Auerbach, in *Atomic and Molecular Beam Methods*, edited by G. Scoles (Oxford University Press, New York, 1988), Vol. 1, Chap. 14, pp. 362-379.

29   F. M. Zimmermann and W. Ho, Surf. Sci. Rep. **22**, 127 (1995).

30   David R. Lide, ed., *CRC Handbook of Chemistry and Physics*, 83 ed. (CRC Press LLC, Boca Raton, FL, 2003), Chap. 5, p. 5.

31   C. Engdahl and G. Wahnström, *Surf. Sci.* **312**, 429 (1994).

32   J. Jacobsen, B. Hammer, K. W. Jacobsen, and J. K. Nørskov, *Phys. Rev. B* **52**(20)**,** 14954 (1995).

33   G. Wahnström, A. B. Lee, and J. Strömquist, *J. Chem. Phys.* **105**(1), 326 (1996).